TAMPEREEN TEKNILLINEN YLIOPISTO
TAMPERE UNIVERSITY OF TECHNOLOGY

Ali Shahed hagh ghadam

Contributions to Analysis and DSP-based Mitigation of Nonlinear Distortion in Radio Transceivers

Julkaisu 984 • Publication 984

Tampere 2011

Tampereen teknillinen yliopisto. Julkaisu 984
Tampere University of Technology. Publication 984

Ali Shahed hagh ghadam

Contributions to Analysis and DSP-based Mitigation of Nonlinear Distortion in Radio Transceivers

Thesis for the degree of Doctor of Technology to be presented with due permission for public examination and criticism in Tietotalo Building, Auditorium TB109, at Tampere University of Technology, on the 21st of October 2011, at 12 noon.

Tampereen teknillinen yliopisto - Tampere University of Technology
Tampere 2011

Supervisor

Mikko Valkama, Dr. Tech., Professor
Department of Communications Engineering
Tampere University of Technology
Tampere, Finland

Pre-examiners

Fernando H. Gregorio, Dr. Tech., Assistant Professor
Department of Electrical Engineering and Computers
Universidad Nacional del Sur
Bahia Blanca, Argentina

Ali M. Niknejad, Ph. D., Associate Professor
Department of Electrical Engineering and Computer Sciences
University of California-Berkeley
Berkeley, USA

Opponent

Markku Juntti, Dr. Tech., Professor
Department of Electrical and Information Engineering
University of Oulu
Oulu, Finland

ISBN 978-952-15-2650-3 (printed)
ISBN 978-952-15-2794-4 (PDF)
ISSN 1459-2045

ABSTRACT

This thesis focuses on different nonlinear distortion aspects in radio transmitter and receivers. Such nonlinear distortion aspects are generally becoming more and more important as the communication waveforms themselves get more complex and thus more sensitive to any distortion. Also balancing between the implementation costs, size, power consumption and radio performance, especially in multiradio devices, creates tendency towards using lower cost, and thus lower quality, radio electronics. Furthermore, increasing requirements on radio flexibility, especially on receiver side, reduces receiver radio frequency (RF) selectivity and thus increases the dynamic range and linearity requirements. Thus overall, proper understanding of nonlinear distortion in radio devices is essential, and also opens the door for clever use of digital signal processing (DSP) in mitigating and suppressing such distortion effects.

On the receiver side, the emphasis in this thesis is mainly on the analysis and DSP based compensation of dominant intermodulation distortion (IMD) effects in wideband direct-conversion receiver (DCR). The DCR structure is studied in the context of wideband flexible radio type of concepts, such as software-defined radio (SDR) and cognitive radio (CR), where minimal selectivity filtering is performed at RF. A general case of wideband received waveform with strong blocking type signals is assumed, and the exact IMD profile on top of the weak signal bands is first derived, covering the nonlinearities of low-noise amplifier (LNA) as well as the small-signal components, like mixers and amplifiers in the in-phase (I) and quadrature-phase (Q) branches of the receiver. Stemming from the derived interference profiles, a versatile DSP-based adaptive interference cancellation (IC) structure is then proposed to mitigate the dominant IMD components at the weak signal bands. Furthermore, the issue of RF-local oscillator (LO) leakage in mixers is addressed in detail, creating in general both static as well as dynamic direct current (DC) offset type of interference at the desired signal band. Using proper receiver and signal modeling, a blind DSP-based method building on independent component analysis (ICA) is then proposed for suppressing such

interference, especially due to strong blocking signals, in multi-antenna diversity receivers. Altogether, both computer simulations as well as measured real-world radio signals are used to verify and demonstrate the operation of the proposed algorithms.

On the transmitter side, the major source on nonlinearity in radio devices is the RF power amplifier (PA). In general, nonlinear PAs possess superior power efficiency compared to linear PAs, but generate also interfering spurious distortion components at the transmitter output. Methods to mitigate such interference, both in-band and out-of-band, also known as linearizers, are highly active research area, and is also the second main theme of this dissertation manuscript. More specifically, the work in this thesis focuses on the so-called feedforward (FF) PA linearizer, which is building on identifying and subtracting the spurious frequency components at and around the PA output. Such FF linearizer can in principle handle wideband transmit waveforms and PA memory, but is also basically sensitive to certain component mismatches in the linearization loops. In this thesis, a closed-form expression relating such component inaccuracies and the achievable linearization performance is derived, being applicable with both memoryless core PAs and core PAs with memory. Furthermore, as one of the main thesis contributions, a so-called DSP-oriented feedforward linearizer (DSP-FF) is proposed in this thesis, which is a versatile implementation where the core of the linearization signal processing is carried out in digital domain at low frequencies, opposed to more traditional all-RF linearizers. Also efficient parameter estimation algorithms are derived for the proposed DSP-FF structure, building on least-squares (LS) model fitting and widely-linear (WL) filtering. Furthermore, the large sample performance of the proposed parameter estimation methods, and there on of the overall linearizer in terms of the achievable IMD attenuation, are derived covering both memoryless PAs and PAs with memory. Overall, extensive computer simulations as well as proof-of-concept type radio signal measurements are used to demonstrate and verify the analysis results as well as the proper operation of the overall linearizer.

PREFACE

This manuscript is the outcome of the studies and research conducted at the Department of Communications Engineering (DCE) at Tampere University of Technology (TUT), Finland. This work was financially sponsored by Doctoral program in Information Science and Engineering (formerly known as Tampere Graduate School in Information Science and Engineering (TISE)), the Academy of Finland (under the projects "Understanding and Mitigation of Analog RF Impairments in Multi-Antenna Transmission Systems" and "Digitally-Enhanced RF for Cognitive Radio Devices"), the Finnish Funding Agency for Technology and Innovation (Tekes; under the projects "Advanced Techniques for RF Impairment Mitigation in Future Wireless Radio Systems" and "Enabling Methods for Dynamic Spectrum Access and Cognitive Radio"), the Technology Industries of Finland Centennial Foundation, Austrian Center of Competence in Mechatronics (ACCM), Nokia Siemens Networks (formerly Nokia Networks), the Nokia Foundation, Tekniikan edistämissäätiö (TES), and the Tuula and Yrjö Neuvo Foundation .

I have been extremely lucky to enjoy the company of many brilliant people in my life that helped me through the highs and lows of my academic career thus far. Interaction with this amazing bunch shaped not only the direction of my scientific career but the human being I am today. My supervisor, Prof. Mikko Valkama taught me to aim for excellence no matter how impossible and difficult. I express my gratitude for the opportunity he provided me to work under his supervision. I am deeply grateful for his help, guidance, support and patience during my research work. Prof. Markku Renfors, who accepted me into DCE family as a young, inexperienced researcher and supervised me with my M.Sc. research topic, taught me how to trust people and bring the best out of them. I am also grateful of my M.Sc. co-supervisor Prof. Tapio Saramäki who introduced me to the concept of controlled insanity in scientific research.

I would like to thank Prof. Andreas Springer, from Institute for Communications and Information Engineering at Johannes Kepler University of Technology, Linz Austria for his hospitality during my research visit to Jo-

hannes Kepler University during summer of 2009. I am also grateful of Dr. Gernot Hueber, former member of the RF innovation group at Danube Integrated Circuit Engineering GmbH & Co KG (DICE), for providing me with the opportunity to work alongside him during the summer of 2009. My special thanks also goes to M.Sc. Sascha Burghlechner not only for fruitful collaboration on topics included in this manuscript but for being such a amazing company throughout my stay in Linz. Meanwhile, I should thank M.Sc. Marcelo Bruno for fruitful collaborations we had during his exchange visit to DCE.

I would like to express deep gratitude to my thesis pre-examiners Assoc. Prof. Ali M. Niknejad from UC-Berkeley, USA, and Asst. Prof. Fernando H. Gregorio from Universidad Nacional del Sur, Argentina, for their insightful comments which opened fascinating perspectives on different topics of the dissertation for me and greatly improved the final manuscript. I also would like to thank Prof. Markku Juntti from University of Oulu, Finland, for agreeing to act as opponent in my dissertation defense.

I would like to thank all my colleagues for the pleasant and friendly work environment in DCE/DTG. Meanwhile, I extend my special thanks to my colleagues in RF-DSP group Dr. Lauri Anttila, Dr. Yaning Zou, M.Sc. Ahmet Hasim Gökceoglu, M.Sc. Adnan Kiayani, M.Sc. Jaakko Marttila, M.Sc. Ville Syrjälä, M.Sc. Markus Allén and M.Sc. Nikolay N. Tchamov for brilliant discussions on the topic of dirty-RF in various occasions and for direct/indirect contribution to my research work as a whole. I also should thank Ulla Siltaloppi, Coordinator of International Education and Elina Orava, Coordinator of International Education in Computing and Electrical Engineering Faculty (CEE), for their tremendous assistance on everyday matters which make life for foreign researchers, like me, less stressful. Also tremendous gratitude toward past and present DCE administrative staff Tarja Erälaukko, Kirsi Viitanen, Sari Kinnari, Daria Ilina and Marianna Jokila for putting up with my constant need for assistance in bureaucratic matter with unlimited patience.

In a more personal level, I would like to thank my past and present office mates Dr. Tobias "the dude" Hidalgo-Stitz, M.Sc. Ahmet Hasim Gökceoglu, M.Sc. Eero Mäki-Esko and M.Sc. Andreas Hernandez for making TG113 the best office in the entire campus. Also, I would like to extend my appreciation to Iranian community in TUT for creating a slice of heart-warming familiarity faraway from home.

My heart-felt gratitude and love to my parents Asghar and Mehri for they provided me with a nurturing environment at home and allowed me to experiment my way through life. I am grateful to grow up with Leily and Haleh, two of the best and funnest sisters one could wish for. And last, but not least, I would like express my genuine and heart-felt love and appreciation to my lovely wife Baharak "nafas" Soltanian and my sweet son Alan

"jigar" Shahed hagh ghadam for making our house feel like home, for their unconditional love and passion, and for the joy they bring to my life.

Ali Shahed hagh ghadam
Tampere, October 2011.

CONTENTS

Abstract **iii**

Preface **v**

List of Publications **xi**

List of Essential Symbols and Abbreviations **xiii**
Symbols xiii
Abbreviations xviii

1 Introduction **1**
1.1 Motivation and Background 1
1.2 Scope of the Thesis: Nonlinear Distortion in Radios 2
1.3 Outline and Main Contributions of the Thesis 7

2 Nonlinear Distortion Effects in Direct-conversion Receivers **11**
2.1 I/Q Processing Principles 11
2.2 Spurious Frequency Profiles for Even- and Odd-Order Nonlinearities 14
2.3 Inter/Cross-modulation Distortion in Direct-conversion Receivers 19

3 Digital Cancellation of Intermodulation in Direct-conversion Receivers **29**
3.1 Basics of Interference Canceller Operation 29
3.2 Computer Simulation and Laboratory Measurement Examples 38

4 Digital Mitigation of Dynamic Offset in Diversity Receivers 45
4.1 Modeling Dynamic Offset in Diversity Receiver 45
4.2 Spatial Processing Methods 46

5 Nonlinearity Modeling and Linearization Techniques in Radio Transmitters 55
5.1 Characterizing Input/Output Relation in RF PA 56
5.2 Linearization Techniques 62

6 Operation and Sensitivity Analysis of Feedforward PA Linearizer 67
6.1 Feedforward linearizer Operation Principle 67
6.2 Linearizer Performance Under the SC and EC Coefficient Errors 68

7 DSP-oriented Feedforward Amplifier Linearizer 75
7.1 DSP-FF Basic Operation Principle 75
7.2 Least-Squares Methods for SC and EC Coefficient Estimation 80
7.3 DSP-FF Linearization Performance Analysis 83
7.4 Simulation and Numerical Examples 86

8 Conclusions 97

9 Summary of Publications and Author's Contributions 101
9.1 Summary of Publications 101
9.2 Author's Contributions to the Publications 102

Appendix 105
A.1 Real Bandpass Nonlinearity 105
A.2 I/Q Bandpass Nonlinearity 107

Bibliography 113

LIST OF PUBLICATIONS

This Thesis is mainly based on the following publications.

[P1] M. Valkama, A. Shahed hagh ghadam, L. Antilla and M. Renfors, "Advanced digital signal processing techniques for compensation of nonlinear distortion in wideband multicarrier radio receivers," *IEEE Trans. Microw. Theory Tech.*, vol. 54, issue 6, Part 1, June 2006, pp. 2356 - 2366

[P2] A. Shahed hagh ghadam, S. Burglechner, A. H. Gökceoglu, M. Valkama, and A. Springer, "Implementation and performance of DSP-oriented feedforward power amplifier linearizer," To appear in *IEEE Trans. Circuits Syst. I: Regular Papers*, vol.59, issue 2, 2012.

[P3] A. Shahed hagh ghadam, T. Huovinen, M. Valkama, "Dynamic offset mitigation in diversity receivers using ICA," in *proc. IEEE Int. Symp. Personal, Indoor and Mobile Radio Communications (PIMRC)*, Athens, Greece, Sep. 2007, pp. 1 - 5

[P4] A. Shahed hagh ghadam, M. Valkama, M. Renfors, "Adaptive compensation of nonlinear distortion in multicarrier direct-conversion receivers," in *proc. IEEE Radio and Wireless Symp.(RAWCON)*, Atlanta, GA, USA, Sep. 2004, pp. 35-38.

[P5] A. Shahed hagh ghadam, A. H. Gökceoglu, M. Valkama, "Coefficient sensitivity analysis for feedforward amplifier linearizer with memory," in *Proc. Int. Symp. Wireless Personal Multimedia Communications (WPMC)*, Saariselkä, Finland, Sep. 2008, .

[P6] S. Burglechner, A. Shahed hagh ghadam, A. Springer, M. Valkama, G. Hueber, "DSP-oriented implementation of feedforward power amplifier linearizer," in *Proc. IEEE Int. Symp. Circuits and Systems (ISCAS)*, Taipei, May 2009, pp. 1755-1758.

LIST OF ESSENTIAL SYMBOLS AND ABBREVIATIONS

Symbols

$\mathbf{A}$	matrix containing SC circuit coefficients for DSP-FF
$\mathbf{A}_{LS,\gamma}$	matrix containing LS-estimated SC circuit coefficients in presence of measurement noise
$\mathbf{A}_{LS,\gamma}^{\infty}$	matrix containing large sample LS-estimated SC circuit coefficients in presence of measurement noise
$\mathbf{A}_{LS}^{wh,\infty}$	matrix containing large sample LS-estimated SC circuit coefficients (Wiener-Hammerstein core PA)
$\mathbf{A}_{opt}$	matrix containing optimum SC circuit coefficients for DSP-FF
$\mathbf{A}_{opt}^{wh}$	$\mathbf{A}_{opt}$ for Wiener-Hammerstein core PA
$A(t)$,$A_0(t)$,$A_1(t)$,$A_2(t)$	envelope of complex baseband signals
a_1,a_2,a_3	polynomial coefficients for passband nonlinearity
$\mathbf{B}$	matrix containing EC circuit coefficients in DSP-FF
$\mathbf{B}_{opt}$	matrix containing optimum EC circuit coefficients in DSP-FF
b_1,b_2,b_3	polynomial coefficients for in-phase branch nonlinearity model
$d(t)$	intermodulation component in Bussgang theory
f_0,f_1,f_2	center frequencies of RF signals
$\mathfrak{f}[.]$	nonlinear function in EASI
$\hat{f}_0$,$\hat{f}_1$,$\hat{f}_2$	center frequencies of signals after downconversion
G_{LNA}	LNA gain in dB
g_1b_1, g_2b_2, g_3b_3	polynomial coefficients for quadrature branch nonlinearity
$g[.]$	static nonlinearity behavioral model
g_e	power gain of error amplifier G_e
$h_D^I(n)$,$h_R^I(n)$	impulse responses of the main and reference path bandsplit filters (in-phase branch)

$h_D^Q(n)$,$h_R^Q(n)$	impulse responses of the main and reference path bandsplit filters (quadrature branch)
$h_1(t)$,$h_2(t)$	impulse responses of pre- and post-filters in Wiener-Hammerstein model
$\mathbf{H}_u$	mixing matrix for statistically independent signal sources $u_i(t)$
$\mathbf{h}_{u,i}$	mixing coefficient vectors for signal $u_i(t)$
$\mathbf{I}$, $\mathbf{I}_{n\times n}$	identity matrix
$IM_k(\omega_i)$	kth-order intermodulation interference resulted from a signal located at ω_i
IMDA_r	Intermodulation distortion attenuation ratio
IMDA_r^∞	Intermodulation distortion attenuation ratio in case large samples are used to estimate EC coefficients
$\text{IMDA}_r^{wh,\infty}$	IMDA_r^∞ for Wiener-Hammerstein core PA
j	$\sqrt{-1}$
$\mathbf{K}_d$	matrix containing I/Q downconverter imbalance coefficients in DSP-FF
$\mathbf{K}_m$	matrix containing I/Q upconverter imbalance coefficients in DSP-FF
$k_{d,1}$,$k_{d,2}$	I/Q downconverter imbalance coefficients in DSP-FF
$k_{m,1}$,$k_{m,2}$	I/Q upconverter imbalance coefficients in DSP-FF
l_c	power loss of the attenuator L_c
l_I,l_Q	LO-RF cross-leakage coefficients for I and Q mixers
$\mathbf{M}(t)$	EASI update matrix
M_α,M_β	number of samples which are used in the estimation of SC and EC coefficients
$n_D(n)$, $n_R(n)$	complex-valued IMD terms in the main and reference path after bandsplit filters
$n_{D,I}(n)$,$n_{R,I}(n)$	IMD terms in the main and reference path after bandsplit filters (in-phase branch)
$n_{D,Q}(n)$,$n_{R,Q}(n)$	IMD terms in the main and reference path after bandsplit filters (quadrature branch)
$\hat{n}_{D,I}(n)$,$\hat{n}_{D,Q}(n)$	IC adaptive filters reference signals in I and Q branch (general)
$\hat{n}_{D,I}^{(2)}(n)$,$\hat{n}_{D,Q}^{(2)}(n)$	IC adaptive filters reference signals in I and Q branch for second-order nonlinearity
$\hat{n}_{D,I}^{(3)}(n)$,$\hat{n}_{D,Q}^{(3)}(n)$	IC adaptive filters reference signals in I and Q branch for third-order nonlinearity
$\mathbf{O}$	all-zero matrix
p_{in},p_γ	input calibrating signal and measurement noise power
p_m,p_d	input and IMD terms power for core PA in DSP-FF
$p_{d,o}^\infty$	IMD power at the DSP-FF output when large samples are used to estimate EC coefficients

$p_{d,o}^{wh,\infty}$	$p_{d,o}^{\infty}$ for Wiener-Hammerstein core PA
$p_{x_u(t)}$	desired signal power at the mixer input in dynamic DC-offset mitigation case
$p_{x_b(t)}$	blocker signal power at RF LNA input in dynamic DC-offset mitigation case
$p_{x_b(t)(ICA)}$	maximum allowable power of the RF blocker interference in ICA-based compensation case
$p_{x_b(t)(MRC)}$	maximum allowable power of the RF blocker interference in MRC-based compensation case
$p_{\|x_b(t)\|^2(ICA)}$	maximum allowable power of the dynamic offset interference in ICA-based compensation case
$p_{\|x_b(t)\|^2(MRC)}$	maximum allowable power of the dynamic offset interference in MRC-based compensation case
$\mathbf{R}_u$	covariance matrix for desired signal mixing coefficient vector $\mathbf{h}_{u,i}$
$\mathbf{R}'_u$	covariance matrix for interference signals mixing coefficient vectors $\mathbf{h}_{u,j}\|_{j\neq i}$
r-SIR	ratio between the SIR_o and SIR_a
r-SIR_{Wiener}	ratio between the SIR_o and SIR_a (Wiener core PA)
SIR_a	SIR at the core PA output in feedforward linearizer
SIR_o	SIR at feedforward linearizer output
$\text{SIR}_{a-Wiener}$	SIR at the core PA output in feedforward (Wiener core PA)
$\text{SIR}_{o-Wiener}$	SIR at feedforward linearizer output (Wiener core PA)
T_s	sampling period
$u_i(t)$	i^{th} statistically independent signal source
$\mathbf{V}_{a,iq}$,$\mathbf{v}_{a,iq}$	matrix and vector containing samples of $v_{a,iq}(n)$
$\mathbf{V}_d$,$\mathbf{v}_d$	matrix and vector containing samples of $v_d(n)$
$\mathbf{V}_{de}$,$\mathbf{v}_{de}$	matrix and vector containing samples of $v_{de}(n)$
$\mathbf{V}_e$,$\mathbf{v}_e$	matrix and vector containing samples of $v_e(n)$
$\mathbf{V}_{e,opt}$,$\mathbf{v}_{e,opt}$	matrix and vector containing samples of $v_{e,opt}(n)$
$\mathbf{V}_{in}$,$\mathbf{v}_{in}$	matrix and vector containing samples of $v_{in}(n)$
$\mathbf{V}_{out}$,$\mathbf{v}_{out}$	matrix and vector containing samples of $v_{out}(n)$
$\mathbf{V}_m$,$\mathbf{v}_m$	matrix and vector containing samples of $v_m(n)$
$\mathbf{V}_\gamma$,$\mathbf{v}_\gamma$	matrix and vector containing samples of $v_\gamma(n)$
$v_{a,RF}(t)$	the core PA RF output in DSP-FF
$v_a(t)$	baseband equivalent of the core PA output in feedforward linearizer
$v_a(n)$	discrete-time baseband equivalent of the core PA output in feedforward linearizer
$v_{a,iq}(n)$	I/Q downconverted version of the core PA output in DSP-FF
$v_{d,RF}(t)$	IMD term at core PA output in DSP-FF
$v_d(t)$	baseband equivalent of IMD term at the core PA output in feedforward linearizer

$v_d(n)$	discrete-time baseband equivalent of IMD term at core PA output in feedforward linearizer
$v_{de}(n)$	discrete-time baseband equivalent of error amplifier output in DSP-FF
$v_e(n)$	discrete-time baseband error signal in DSP-FF
$v_{e,opt}(n)$	discrete-time baseband error signal in DSP-FF given optimum SC coefficients
$v_{in}(n)$	discrete-time baseband input calibrating signal
$v_{m,RF}(t)$	the core PA RF input in DSP-FF
$v_m(n)$	discrete-time baseband equivalent of core PA input in in feedforward linearizer
$v_m(t)$	baseband equivalent of core PA input in feedforward linearizer
$v_o(t)$	baseband equivalent of feedforward linearizer output
$v_o(n)$	discrete-time baseband equivalent of feedforward linearizer output
$v_{out}(n)$	discrete-time baseband output calibrating signal
$v_\gamma(n)$	discrete-time baseband equivalent of measurement noise
$\mathbf{w}_I$,$\mathbf{w}_Q$	IC adaptive filter coefficients vectors for I and Q branches
$\mathbf{W}_D$	diversity (achieving) matrix
$\mathbf{W}_{EASI}(t)$	diversity (achieving) matrix for EASI algorithm
$\mathbf{w}_{D,i}$	i^{th} column of $\mathbf{W}_D$
$w_{i,I}$,$w_{i,Q}$	IC adaptive filters ith coefficients for I and Q branches
$x_{RF}(t)$	bandpass RF signal
$x_{iq}(t)$	I/Q downconverted version of signal $x_{RF}(t)$
$x(t)$	complex baseband signal
$x_I(t)$	in-phase component of signal $x(t)$
$x_Q(t)$	quadrature component of signal $x(t)$
$x_u(t)$	complex baseband version of the desired signal
$x_b(t)$	complex baseband version of the blocker signal
$x_{D,I}(t)$,$x_{R,I}(t)$	in-phase part of desired and reference signal before nonlinearity
$x_{D,Q}(t)$,$x_{R,Q}(t)$	quadrature part of the desired and reference signals before nonlinearty
$x_D(t)$,$x_R(t)$	complex-valued desired and reference signals before nonlinearity
$\mathbf{x}_\gamma$	vector containing $x_{\gamma,i}$s for all the front-end branches
$x_{\gamma,i}$	zero-mean white Gaussian noise for ith front-end branch
$y_{RF}(t)$	output of the bandpass nonlinearity model
$y_{D,I}(n)$,$y_{R,I}(n)$	signals of the main and reference pathes after bandsplit filters (in-phase branch)
$y_{D,Q}(n)$,$y_{R,Q}(n)$	signals of the main and reference pathes after bandsplit filters (quadrature branch)

$y_D(t)$,$y_R(t)$	complex-valued desired and reference signals after nonlinearity
$\mathbf{Z}$	mixing matrix for dynamic DC-offset case
$\mathbf{z}_u$,$\mathbf{z}_b$	vectors containing channel coefficients for the desired signal and blockers for receiver front-ends
Λ_G	matrix containing desired signal gain of the core PA in DSP-FF
α,α_1,α_2,	SC circuit coefficients
$\alpha_{1,LS}$,$\alpha_{2,LS}$	LS-estimated SC circuit coefficients
$\alpha_{1,LS}^{\infty}$,$\alpha_{2,LS}^{\infty}$	large sample size LS-estimated SC circuit coefficients
α_{opt},$\alpha_{1,opt}$,$\alpha_{2,opt}$	SC circuit optimum coefficients
α_G	amplifier desired signal gain
α_{Lin}	amplifier linear gain
$\alpha_A(.)$	PA AM-AM transfer-function
β,β_1,β_2,	EC circuit coefficients
$\beta_{1,LS}$,$\beta_{2,LS}$	LS-estimated EC circuit coefficients
$\beta_{1,LS}^{\infty}$,$\beta_{2,LS}^{\infty}$	large sample size LS-estimated EC circuit coefficients
β_{opt},$\beta_{1,opt}$,$\beta_{2,opt}$	EC circuit optimum coefficients
$\epsilon_{\beta,1}^{\infty}$,$\epsilon_{\beta,2}^{\infty}$	error in the estimation of EC coefficients in large sample case
$\phi_0(t)$,$\phi_1(t)$,$\phi_2(t)$	phase of complex baseband signals
$\psi_A(.)$	PA AM-PM transfer function
ω_0,ω_1,ω_2	angular center frequencies of RF signals
$\omega_u(t)$	angular center frequency of desired signal at RF
$\omega_b(t)$	angular center frequency of blocker signal at RF
$\hat{\omega}_0$,$\hat{\omega}_1$,$\hat{\omega}_2$	angular center frequencies of signals after downconversion
μ	IC adaptive filter step-size
μ_{EASI}	EASI algorithm step-size
Σ_B^{∞}	matrix containing errors in the estimation of EC coefficients in large sample case
$\Upsilon_{SNR,in}$	matrix containing signal-to-measurement-noise ratio of the input calibrating signal $v_{in}(n)$
$\Xi_k^{IM/CM}$	kth-order non-interfering inter/cross-modulation components
ξ_α,ξ_β	normalized error in the SC and EC circuit coefficients
$\zeta_{u,i}$,$\zeta_{b,i}$	desired signal and blocker channel coefficients for receiver i^{th} front-end
$\approx$	approximation
$\lvert.\rvert$	absolute value
$(.)^*$	complex conjugate
$(.)^T$	transposition

$(.)^H$	conjugate-transpose (Hermitian)
$(.)^\dagger$	matrix pseudoinverse
$\mathbb{E}[.]$	statistical expectation
Re[.]	real part of complex signal
Im[.]	imaginary part of complex signal

Abbreviations

AC	alternating current
ACLR	adjacent channel leakage ratio
ADC	analog-to-digital converter
AM-AM	amplitude-to-amplitude modulation
AM-PM	amplitude-to-phase modulation
AWGN	additive white Gaussian noise
BPF	bandpass filter
CDMA	code division multiple access
C/I	carrier-to-interference ratio
CR	cognitive radio
DAC	digital-to-analog converter
DC	direct current
DCR	direct-conversion receiver
DLS	data least-squares
DPD	digital predistortion
DSP	digital signal processing
DSP-FF	DSP-oriented feedforward (linearizer)
dB	decibel
EASI	equivariant adaptive source identification
EC	error cancellation (circuit)
EVM	error vector magnitude
FFT	fast Fourier transform
FIR	finite impulse response
GHz	gigaherz
HPF	highpass filter
IBO	input back-off
IC	interference cancellation
ICA	independent component analysis
IF	intermediate frequency
IFFT	inverse fast Fourier transform
IMD	intermodulation distortion
I/Q	in-phase and quadrature (parts of signal)
LO	local oscillator
LNA	low-noise Amplifier
LS	least-squares

LTE	long-term evolution
MF	matched filter
M-GEF	(SINR) maximizing generalized Eigen-gilter
MHz	megaherz
MMF	matrix matched filter
MRC	maximum ratio combining
NF	noise figure
OFDM	orthogonal frequency division multiplexing
P1dB	1 dB compression point
P3dB	3 dB compression point
PA	power amplifier
PAPR	peak-to-average power ratio
QAM	quadrature amplitude modulation
QPSK	quadrature phase shift keying
RF	radio frequency
SC	signal cancellation (circuit)
SDR	software-defined radio
SER	symbol error rate
SINR	signal-to-interference-and-Noise Ratio
SIR	signal-to-interference ratio
SNR	signal-to-noise ratio
SSPA	solid-state power amplifier
UMTS	Universal Mobile Telecommunications System
WH	Wiener-Hammerstein
WJ	Watkins Johnson
WL	widely linear
ZF	zero-forcing

CHAPTER 1

INTRODUCTION

1.1 Motivation and Background

Throughout the years many application-specific radio standards have been developed each optimized for a particular radio transmission scenario from stationary close-range communication such as near-field communication (NFC) [1] to high-mobility long-range radio transmissions such as long-term evolution (LTE) [2]. Nowadays, the state-of-the-art radio terminals are expected to integrate many of these standards in one integrated and high performance, yet affordable and power efficient package which, in turn, introduces many challenging constrains particularly in radio front-end design. These constrains are becoming even more challenging with the recent trend toward more flexible exploitation of available spectrum as introduced by paradigm shifting concepts such as cognitive radio (CR) [3, 4]. The receivers based on CR concept, for instance, are required to be wideband with high sensitivity and large dynamic range to be able to receive a weak desired signal in any arbitrary frequency and in the presence of significantly stronger signals [5–7]. As the result, the receiver analog front-end (Fig.1.1) of the CR should be implemented using linear and high quality analog components which results in rather expensive design with poor power efficiency. The CR transmitters, in turn, should be capable of transmitting at any arbitrary band through out the spectrum and without interfering with the regulated radios [5, 7]. Again, this can be obtained by deploying highly linear, yet expensive and power in-efficient, analog components in the transmitter front-end (Fig.1.1). It is in these contexts that employing *dirty-RF* [8] concept is justified. The dirty-RF, in general, refers to a digital/mixed signal processing algorithm targeted at improving/correcting the performance of the analog front-end in the radio transceivers. In particular, implementing dirty-RF-based algorithms for com-

pensating the effects of nonlinearity in radio transceivers ease the linearity constrains on the analog components of the radio transceivers which in turn results in cheap yet high performance transceiver with excellent battery-life.

On the other hand, to design dirty-RF strategies for combating non-idealities in the transceiver front-end, including front-end nonlinearity, the effects of the non-idealities should be fully explored and understood. Therefore, this manuscript aims to shed light on the different nonlinearity mechanisms, as the non-ideality under the focus of this manuscript, and their effects in radio transceivers. Thereafter, based on the acquired knowledge, several dirty-RF-based DSP algorithms are proposed to compensate the effects of nonlinearity in the front-end of radio transceivers.

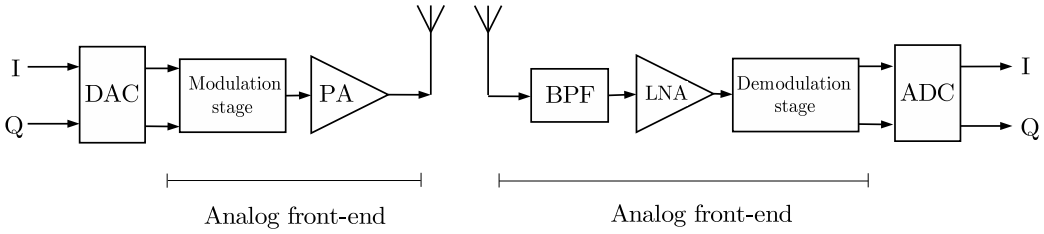

Figure 1.1: Wireless transmitter (left) and receiver (right) at conceptual level.

1.2 Scope of the Thesis: Nonlinear Distortion in Radios

1.2.1 Nonlinear Interference in Direct-Conversion Receivers

Direct-conversion receiver (DCR) (Fig.1.2) is implemented based on the idea of I/Q downconverting the desired radio frequency (RF) band directly to the baseband. This is an alternative to superheterodyne receiver which downconverts the RF band of interest through multiple intermediate frequencies (IF). DCR eliminates the need for a number of off-chip elements, e.g. RF/IF image rejection filters which are typically used in the superheterodyne receivers [9, 10], and therefore suits better for monolithic designs. One closely related structure to DCR is the low-IF [11,12] receiver concept. In this structure the desired signal is I/Q downconverted directly to a low-IF frequency and typically the conversion from low-IF to zero-frequency is performed in the digital segment of the receiver. It is possible to view DCR as a special case of low-IF receiver where the IF frequency is actually zero [13]. The line between the DCR and low-IF concept is particularly unclear in the context of multichannel receivers where multiple signals in different channels are

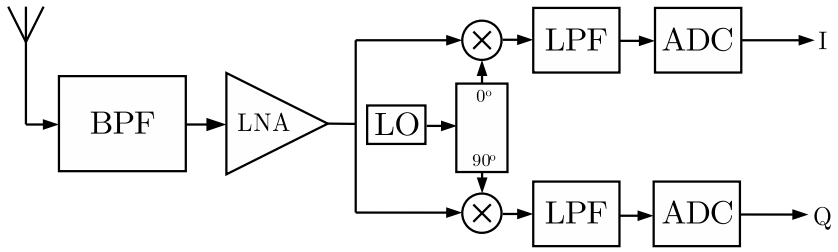

Figure 1.2: Conceptual direct-conversion receiver (DCR).

I/Q downconverted as a whole. In this case implementing DCR structure to downconvert a particular band to the baseband causes most of the signals in the band of interest to be situated at low-IF frequencies around the baseband. Therefore, although the DCR concept is applied for that particular signal which is downconverted to the baseband, the other signals in the band of interest are actually downconverted using low-IF concept. In this manuscript, we denote DCR to the general concept of wideband I/Q downconversion of multichannel/multicarrier signal to lower frequencies such that one of the channels follows plain direct-conversion model while other channels are then following the low-IF model. The desired channel can generally be any of these.

The challenges in implementing DCR structure, i.e., I/Q imbalance [14–17], flicker noise [14, 18, 19], nonlinear signal distortion [13, 14, 18–20] and DC-offset distortion [13, 14, 18–20] are well-known and documented in various publications. In this manuscript we address the two latter issues. More specifically, the issue of inter/cross-modulation interferences which are generated from multiple strong signals in the band of interest is analyzed in this manuscript, considering both odd- and even-order nonlinearity in low-noise amplifier (LNA) and in the I and Q branches of the DCR downconversion path. An adaptive DSP-based interference cancellation method is then proposed to remedy the distortion effects. In this proposal the downconverted signal band, including the desired signal and strong blockers, is split into two branches in the DSP domain. The main branch contains the desired signal plus the interfering components resulting from strong out-of-band signals. The rest of the downconverted band passes through the so-called *reference* branch. The interfering inter/cross-modulation components are regenerated, up to a complex scale factor, from the strong signals in the reference branch using second-order, cubic, fourth-order,... nonlinear models. Finally, the regenerated interfering components are subtracted adaptively from the main branch aiming to cancel out the interfering terms.

In this thesis the DC-offset issue is also studied in the context of multicarrier/multichannel in which the desired signal is directly downconverted to the baseband and single/multiple strong signals are also present in the

downconverted band. The source of the DC-offset components is basically the lack of proper isolation in the mixer ports [13, 14, 18, 20] which, in turn, results in cross-leakage of RF and LO signals. These two phenomena, i.e., leaking RF signal into LO path and vice versa, generate two distinct types of DC-offset, namely dynamic and static. Both dynamic and static DC-offset are analyzed in this manuscript. Particularly, the dynamic DC-offset, as the more challenging issue among the two, is the main focus of this manuscript. The dynamic DC-offset in a diversity receiver is analyzed. Moreover, a compensation scheme deploying higher order statistics based spatial processing is proposed to address this issue in the context of diversity receivers.

1.2.2 Earlier and Related Works

The issue of nonlinear distortion in the DCR has been studied in various works (e.g. [21–24]) prior to the publication of manuscript [P4]. In fact, the work presented in [P1] and [P4] can be viewed as a generalization of the ideas in [21] in which the focus is on cancelling only the second-order interference in DCR structure. In [25] a hybrid analog-digital calibration technique has also been proposed which uses certain feedback from the receiver digital parts back to the analog sections. The feedback signal is used to adjust the I/Q mixer parameters in order to push down the observed nonlinear distortion components. Since the publication of [P4] in 2004 and [P1] in 2006, several extensions/variations of the proposed interference cancellation method has been reported in literature, most notably [26–29]. The work reported in [26] deploys the proposed DSP cancellation method of [P1] and [P4] to mitigate the cross-modulation distortion in the framework of software-defined radio (SDR) concept using a block based algorithm. In [27, 28] the interference cancellation proposed in [P1] and [P4] is deployed to mitigate third-order interference terms stemming from strong signals in the band of interest for a universal mobile telecommunications system (UMTS) receiver. In this approach the strong interference-generating signals are captured already after the LNA and the whole process of regenerating the third-order interfering terms are implemented in the analog domain rather than the DSP domain as is proposed in [P1] and [P4]. The extension of the work in [27, 28] for mitigating higher order interference terms are reported in [29]. The same interference cancellation method is also proposed to compensate for nonlinear behavior in ADC [30].

The problem of dynamic DC offset in direct conversion receivers and various solutions for this issue in single front-end context are reported in various publications, e.g., [6, 13, 14, 21, 31, 32]. Naturally, these solutions can be applied for individual front-end branches in the case of multi-front-end (multi-antenna) receivers. However, as the number of front-end branches increases the cost of compensating for dynamic DC-offset accumulates pro-

portionally. Therefore, devising a flexible and scalable DSP-based algorithm, such as the one proposed in [P3], to mitigate dynamic DC-offset in all the branches of the multi-front-end (multi-antenna) receiver, is an attractive solution. One more important note on this topic is that the initial idea which is implemented in [P3] lead to investigation on the performance of independent component analysis (ICA) algorithm in noisy environments. The outcomes of this branch of study are reported in [33, 34].

1.2.3 Transmitter Nonlinearity and Feedforward Linearization Technique

The main purpose of radio communication transmitter is to transmit the information bearing signal to radio receiver while maximizing the data transfer considering the degrading effects in wireless medium e.g. channel noise and fading. This should be achieved through parsimonious deployment of resources such as spectrum and power with minimum interference to other radio devices that are sharing the same medium. Current solutions to achieve desirable spectral efficiency partially involves exploiting high order symbol alphabet and wideband multicarrier communications wave forms [35,36]. These waveforms due to their high peak-to-average power ratio (PAPR) require highly linear power amplifier (PA) in the transmitter front-end [37, 38]. On the other hand, linear PAs by design have low power efficiency which in turn results in poor overall power efficiency and excessive heat dissipation in radio transmitters [39, 40].

A prominent solution to enhance the power efficiency of a radio transmitter is to combine the use of nonlinear, and power efficient, PA and a *linearizer*. Linearization in general is a process in which the interferences which are resulting from the nonlinear PA, i.e., intermodulation distortion (IMD) products, are mitigated through combination of additional circuitry and advanced (digital) signal processing algorithms. Feedforward linearizer in Fig. 1.3, as the focus of this manuscript, is one of the most established methods of linearization. In short, the idea in feedforward linearization is to re-generate the interfering IMD products in signal cancellation (SC) circuit and subtract them from the final RF waveform in error cancellation (EC) circuit. In general, feedforward linearizer PA is unconditionally stable, PA model independent and particularly effective in wideband signal transmission schemes with stringent linearity constrains [39, 41–45]. However, one of the main issues in feedforward structure is the vulnerability to any delay and/or gain mismatches between the upper and lower branches. Also any deviations in the linearizer coefficients α and β from their nominal values result in linearizer performance degradation in general. The latter issue in feedforward linearizer is analyzed [P5]. Particularly, as one of the contributions of this thesis, the coefficients sensitivity analyses are extended to the case

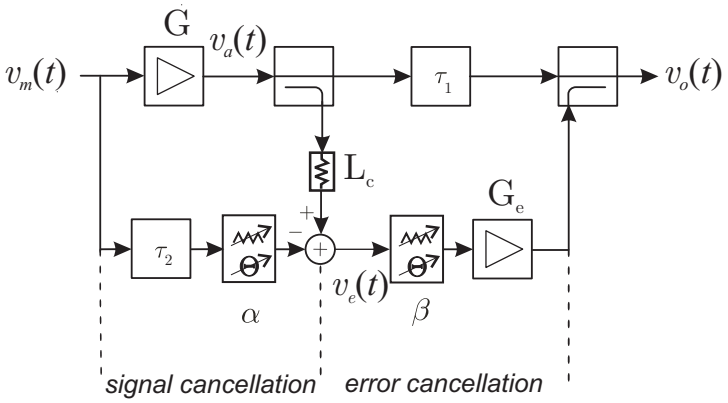

Figure 1.3: Baseband equivalent of feedforward power amplifier linearizer structure.

where core PA exhibits memory effects [P5]. Another issue in implementing feedforward linearizer is that it is commonly implemented entirely in the RF segment of the transmitter. This results in a bulky and rigid design not so attractive for modern radio device concepts such as SDR and CR. In this manuscript, we address this issue by proposing a DSP-oriented approach in implementing the feedforward linearizer ([P2] and [P6]). In DSP-oriented feedforward structure parts of the the EC and SC circuits are transferred to the DSP regime. Moreover, the calibration of EC and SC circuits are performed independently and therefore the errors in the estimation of one circuit do not affect the estimation of the other. This is certainly an advantage over sequential gradient based algorithms which are typically used for the adaptation/calibration of *all-RF* feedforward linearizers [41,46,47]. Also closed-form linearization performance analysis under large-sample conditions is carried out for the overall linearizer concept.

1.2.4 Earlier and Related Works

Effects of misadjusting the feedforward linearizer coefficients in the overall performance of this linearizer and for the case of the PA with instantaneous nonlinearity has been treated extensively in the literature [39, 41, 43]. Nevertheless, including the memory in the performance analysis, as one of the contributions of this manuscript, enhances our understanding on the influence of these coefficients in more generalized and practical settings. On the topic of DSP-oriented feedforward linearizer (DSP-FF), few *partially* DSP based implementations of feedforward linearizer have been reported to address the size and flexibility issues [48–53]. The proposals in [48, 50, 51, 53] generate the IMD components in DSP regime assuming certain behavioral model for the core PA. This approach delegates substantial part of the feed-

forward linearizer functionality from RF to DSP and eliminates most of the RF components. However, the accuracy and the validity of the assumed behavioral model for the core PA affects such linearizer performance. The proposal in [49], in turn, attempts to compensate for the linear distortions stemming from the RF components of feedforward linearizer already in the digital baseband. This structure enhances the feedforward linearizer performance in wideband applications, but, the bulk of the feedforward linearizer in such structure is still implemented in the RF regime. In the structure of [52], the lower branch of the SC circuit is already implemented in the digital domain. However, the EC circuit is still implemented in the RF domain. The adaptation/calibration algorithm in this approach is based on successive adaptation of the SC and EC circuits which is initially proposed in [41]. This calibration/adaptation method has the advantage of tracking the possible circuit parameter changes without interrupting the transmission, while the transmitted signal is still degraded during the initial convergence time. On the downside, this calibration/adaptation suffers from the estimation error propagation from SC to EC circuit. In other words, any estimation error in the SC circuit, significantly deteriorate the estimation error in the EC circuit [41]. The estimation error propagation from SC to EC problem is averted in the proposed structure in [P2] and [P6] by devising two independent least-squares-based estimation algorithm for SC and EC circuit.

1.3 Outline and Main Contributions of the Thesis

In general this manuscript studies the effects of nonlinearity in radio transmitters and receivers front-ends. In Chapter 2 first the basics of I/Q signal processing is reviewed. This principle is the fundamental concept behind the operation of DCR which is the focus of this manuscript. Thereafter, the spurious frequency profile of nonlinearities categorized in odd- and even-order cases are presented. This analysis is performed using multi-tone input as well as multiple modulated signals. The multi-tone characterization of a nonlinear element provides a clear picture on the frequencies of these components in comparison to the original input tone frequencies. On the other hand, the characterization of a nonlinear element using multiple modulated signals provides a broader view not only on the spectrum profile of the spurious frequency components but on their envelopes and phases which are particularly important in understanding the true nature of the nonlinearity-born spurious components. It also creates a solid foundation for understanding and analysis of the interference cancellation-based compensation method which is proposed in [P1] and [P4]. The spurious frequency profiles are also delineated for two distinct scenarios. One, multiple real-valued bandpass signals pass

through odd- and even-order nonlinearities. The results of this study shed light on the nonlinear behavior of such components as LNA. Two, multiple complex-valued bandpass signals pass through I and Q nonlinear components. Viewing the output spurious component profiles in this case from complex-signal point of view reveals interesting differences comparing to the first case study which enhances our understanding of the nonlinear behavior of I/Q downconverters with nonlinear elements in their path. Example spurious frequency components of such scenarios for three-signal scenario are derived in detail in the Appendix. The results of these derivations are used throughout the discussions in Chapters 2 and 3.

The final section of Chapter 2, describes the interference profile on top of the desired signal band stemming from nonlinearities in LNA, mixers and subsequent stages of DCR. More precisely, a scenario in which the antenna picks up multiple strong signals, or *blockers*, within the same spectrum as the weak desired signal is studied. The contributions of odd-order nonlinearity in LNA to the interference in desired signal band as the result of these blockers are delineated. Special scenarios in which even-order nonlinearity in LNA contributes to the desired signal band interference are emphasized, most notably the role of even-order LNA nonlinearity for future wideband receivers which are based on SDR and CR concepts. The contributions of nonlinearity in the mixer and amplification stages of the I and Q branches in DCR to the desired signal band interference profile are also studied in this section. The final part of this section is dedicated to describing the DC-offset phenomenon in DCR as the result of finite isolations between mixing core ports. Particularly, the difference between dynamic and static DC-offset and the mechanisms which yield these offsets are explained and the signal level expressions for both dynamic and static DC-offset are provided in this section.

The basics and operation principle of the DSP-based adaptive interference cancellation method which is originally proposed in [P1] and [P4], are presented in Chapter 3. This method is designed to mitigate the effects of the nonlinear inter/cross-modulation interfering products resulting from nonlinear LNA and nonlinear elements in I and Q branches of DCR downconversion path through regenerating the interfering terms and adaptively subtracting them from the nonlinear device output in a feedforward structure. The signal level analysis of the proposed algorithm reveals the essential conditions under which this algorithm performs optimally. These conditions are examined and justified using the three-signal example derivation provided in the Appendix.

Chapter 4 is dedicated to the issue of dynamic DC-offset in diversity receivers. First, a signal model is developed for an example two-front-end DCR suffering from dynamic DC-offset. It is shown that the optimal solution to mitigate the dynamic DC-offset is the spatial signal processing method that achieves the maximum signal-to-interference-plus-noise ratio (SINR) such as

SINR maximizing generalized Eigen-filter (M-GEF) [33,54,55]. However, the essential assumption in these algorithms is that the noise power and the channel coefficients are known to the receiver. In the continuation of this chapter the independent component analysis (ICA) based algorithm, which is initially proposed in [P3], is described. This algorithm is capable of separating the desired signal from the dynamic DC-offset, up to scale and permutation, blindly. Thus no knowledge of the noise level and channel coefficients are required in this method. The SINR which is achieved by ICA-based method is shown through computer simulation examples to be close to M-GEF-based receiver.

The basics and background of the nonlinearity characterization for RF PA are described in Chapter 5. The concept of behavioral modeling as a system-level description of RF PA input-output relation is briefly discussed. Various widely used behavioral models for RF PA including Wiener, Hammerstein and Wiener-Hammerstein models are introduced in this chapter. The linearization concept as a viable solution to the power efficiency and linearity dilemma in RF PA is discussed. The digital predistortion (DPD) as a promising, yet developing, linearization method and feedforward linearizer as the most developed linearization technique are briefly described in this chapter.

The operation principle and signal models for feedforward linearizer are described in detail in Chapter 6. Thereafter, the effects of misadjusting the feedforward linearizer coefficients on linearization performance of this linearizer are studied. A measure called relative signal-to-interference ratio (r-SIR) [P5] is introduced as the ratio between signal-to-interference ratio (SIR) at the input of the PA and at the feedforward linearizer output. This measure is then used to quantify the linearization performance of the feedforward linearizer. A unified expression for r-SIR in terms of errors in feedforward linearizer coefficients in the case of the memoryless core PA and in the case where the core PA exhibits memory is derived in this chapter.

A variation of feedforward structure, i.e., DSP-FF is introduced in Chapter 7. The basic operation and signal level models for this structure are presented in this chapter. Thereafter, two independent block-based algorithms are proposed for calibration of the SC and EC circuits. A closed-form expression for the EC circuit coefficients estimation error is presented. In addition, a new measure for the performance analysis of DSP-FF is proposed. This figure of merit, i.e., intermodulation distortion attenuation ratio (IMDA_r), is defined as the power ratio between the IMD at the PA and DSP-FF outputs. A closed form expression for IMDA_r in terms of circuit parameters is derived. The analysis results are also extended for the case that the core PA exhibits memory effects. The closed form expressions for EC circuit coefficients estimation and IMDA_r as well as the DSP-FF gain analysis in this chapter fully describe the relation between the estimation errors in EC and SC and

the linearization performance of DSP-FF. This, in fact, enables designers to predict the performance of DSP-FF analytically without the need for lengthy simulations.

A general conclusion on the topics discussed in this manuscript are drawn in Chapter 8. The summary of publications and author's contributions to the publications are included in Chapter 9.

All in all, the main purpose of this manuscript is to provide a platform to present the author's contributions in [P1]-[P6] in a unified manner. From the receiver perspective, the contributions of the author are the overall nonlinearity-born interference analysis of the DCR downconversion chain in Chapter 2, the adaptive IC method in Chapter 3 and the ICA-based DC-offset mitigation method in Chapter 4. The contributions of the author in analyzing the effects of the errors in the SC and EC coefficients for all-RF feedforward in the case of core PA with memory are included in Chapter 6. The entire Chapter 7 includes all the contributions of the author in proposing, signal-level analysis as well as performance analysis of DSP-FF. Naturally, more detailed information and analysis on the above mentioned topics are available in [P1]-[P6].

CHAPTER 2

NONLINEAR DISTORTION EFFECTS IN DIRECT-CONVERSION RECEIVERS

2.1 I/Q Processing Principles

Understanding the true nature of bandpass signals and systems is the key in building efficient radio transmitters and receivers. In addition to the basic envelope and phase representation, the so called I/Q (in-phase/quadrature) interpretation forms the basis for various spectrally efficient modulation and demodulation techniques [36]. And more generally, I/Q processing can be used in the receiver and transmitter front-ends for efficient down/upconversion processing, independently of the applied modulation technique. Given a general bandpass signal

$$\begin{aligned} x_{RF}(t) = 2\mathrm{Re}[x(t)e^{j\omega_0 t}] &= x(t)e^{j\omega_0 t} + x^*(t)e^{-j\omega_0 t} \\ &= 2x_I(t)\cos(\omega_0 t) - 2x_Q(t)\sin(\omega_0 t) \\ &= 2A(t)\cos(\omega_0 t + \phi(t)) \end{aligned} \tag{2.1}$$

the (formal) baseband equivalent signal $x(t)$ is defined as

$$x(t) = A(t)e^{j\phi(t)} = A(t)\cos(\phi(t)) + jA(t)\sin(\phi(t)) = x_I(t) + jx_Q(t) \tag{2.2}$$

where $A(t)$ and $\phi(t)$ denote the actual envelope and phase function, and the corresponding I and Q signals appear as $x_I(t) = A(t)\cos(\phi(t))$ and $x_Q(t) = A(t)\sin(\phi(t))$, respectively. The baseband equivalent signal $x(t)$

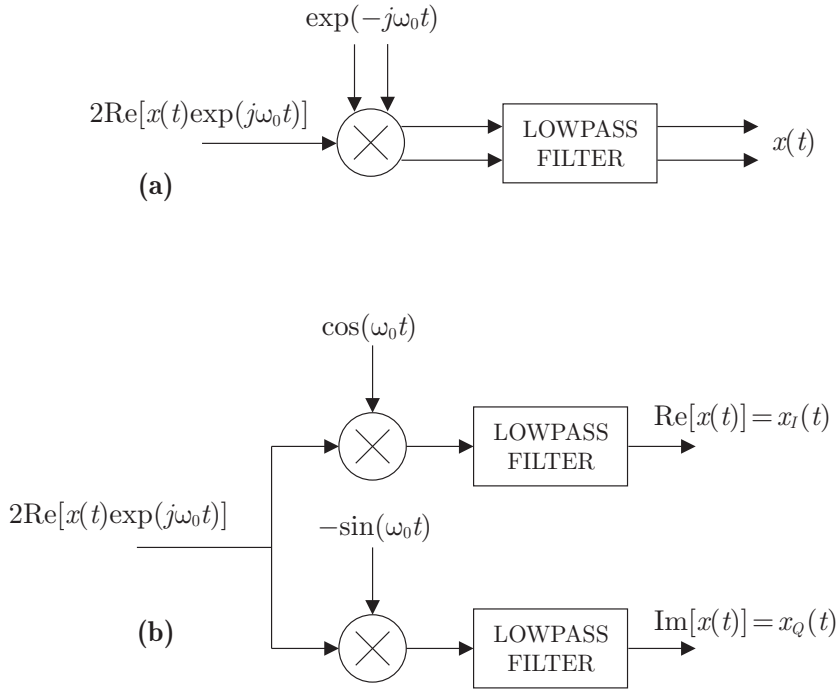

Figure 2.1: Basic I/Q downconversion principle in terms of (a) complex signals and (b) parallel real signals.

can be recovered by multiplying the modulated signal with a complex exponential $e^{-j\omega_0 t}$ and lowpass filtering. This is illustrated in Fig. 2.1 which also depicts the practical implementation structure based on two parallel real signals. In the receiver architecture context, the differences come basically from the interpretation of the downconverted signal structure. In general, both the direct-conversion [9, 13, 14, 18] and low-IF [9, 12] receivers utilize the I/Q downconversion principle and are discussed in more detail in the following. The so called DCR, also known as homodyne receiver, is based on the idea of I/Q downconverting the channel of interest from RF directly to baseband [9,13,14,18]. Thus in a basic single-channel context, the downconverted signal after lowpass filtering is basically ready for modulation-specific processing such as equalization and detection. On the other hand, low-IF receiver [9,12], uses I/Q downconversion to a low but nonzero IF. Thus here a further downconversion from IF to baseband is basically needed before detection, depending somewhat on the actual data modulation. In the basic scenarios, this can be done digitally after sampling the signal at low intermediate frequency. In a wider context, with multiple frequency channels to be detected, a generalization of the previous principles leads to a structure where the whole band of interest is I/Q downconverted as a whole. In this case, either the direct-conversion or low-IF model applies to individual chan-

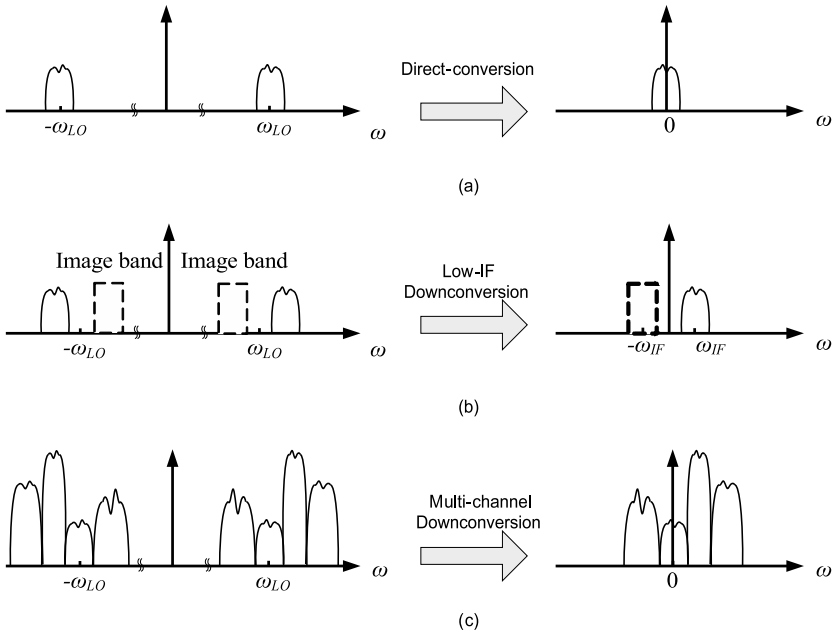

Figure 2.2: (a) Spectra of RF signal (left) and the ideally downconverted signal (right) using direct-conversion principle. (b) Spectra of RF signal (left) and the ideally downconverted signal (right) using low-IF downconversion principle. (c) Spectra of four-channel RF signal (left) and the ideally downconverted signal (right) using direct-conversion/low-IF downconversion principle.

nels but the concept itself is simply referred to as wideband or multicarrier I/Q downconversion. In this manuscript the term DCR is generally used in its wideband I/Q downconversion sense, unless otherwise mentioned.

In general DCR structure is an attractive choice when it comes to monolithic receiver design by eliminating the use of any intermediate frequencies (IF) which results in rather simple front-end processing, especially in terms of the needed RF/IF filtering. Of course, DCR structure in practice suffers from number of nonidealities namely gain and phase imbalance in I and Q branches [14,15], flicker noise [13,14,18], local oscillator (LO)/ RF signal leakage [13, 14, 18] and even/odd-order nonlinearity distortions [13, 14, 18, 32, 56]. One main theme of this manuscript is to treat the two latter topics and to propose methods to remedy their effects on the performance of DCR structure.

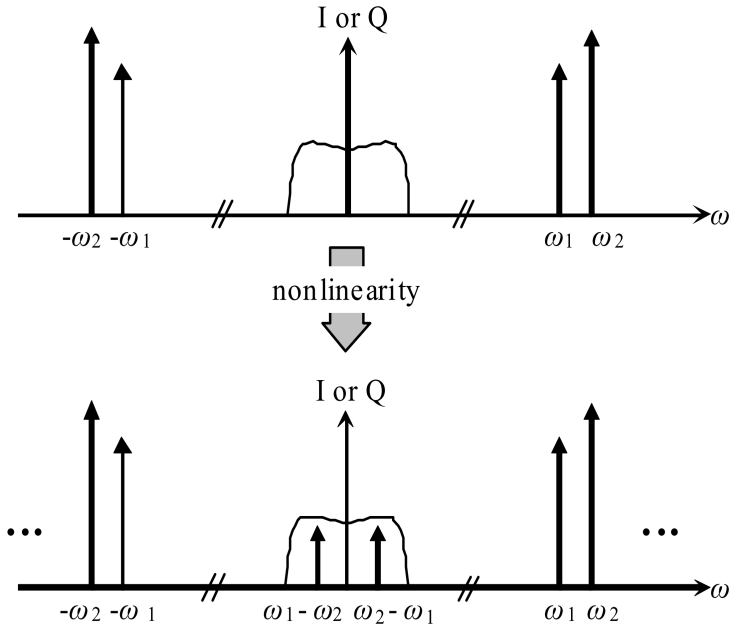

Figure 2.3: Second-order Cross-modulation interference on top of desired signal in a DCR.

2.2 Spurious Frequency Profiles for Even- and Odd-Order Nonlinearities

Studying the effects of nonlinearity, there are two main aspects in general - (*i*) the self-distortion of any individual modulated signal and (*ii*) the spurious interference components stemming from other signals, such as harmonic and intermodulation distortion, falling on top of the desired signal band. The focus in this discussion is on the latter aspects in the wideband I/Q downconversion based receiver context where the RF front-end provides only preliminary band limitation. Thus, the spurious distortion components of strong blockers can easily hit the desired signal band. A basic scenario in which the intermodulation terms from two strong signal tones hit the desired signal band is depicted in Fig.2.3. To gain an insight to the spurious frequency profile of a nonlinear element and for analysis purpose, the model for the nonlinear component or components under study is assumed to be a memoryless polynomial of the form

$$y_{RF}(t) = a_1 x_{RF}(t) + a_2 x_{RF}^2(t) + a_3 x_{RF}^3(t) + ... \tag{2.3}$$

where $x_{RF}(t)$ and $y_{RF}(t)$ denote the input and output signals, respectively. Traditionally, the intermodulation/harmonics distortion profile in such a nonlinearity is defined based on the single-tone or the two-tone response of the

nonlinearity in which the input of the nonlinearity are tone sinusoidal signals. Excitement of such an element modeled by (2.3) with a blocker signal with two frequency components, say ω_1 and ω_2, results in two groups of frequencies at the output - the *harmonics* of the form $n \times \omega_1$ and $m \times \omega_2$, and the intermodulation (or cross-modulation) frequencies $\pm n \times \omega_1 \pm m \times \omega_2$, $n, m = 1, 2, 3, ...$ as is well-known in the literature [10, 19, 57–61].

A more realistic spurious frequency profile of odd-/even-order nonlinearity from radio receivers perspective can be obtained using bandpass modulated signals as the input of the nonlinear component. In contrast to the pure-tone characterization method, these types of analysis provide information on the spurious components center frequencies as well as their envelopes and phases which is essential in understanding the nature of these terms as interference. One example of such analysis is presented in detail in the Appendix A.1. The provided analysis aim to motivate for understanding of the inter/cross-modulation profiles of devices such as LNA with mild nonlinearity. Therefore, the nonlinear elements up to third-order are considered in the analysis. Moreover, the nonlinear component input $x_{RF}(t)$ consists of three bandpass signals at ω_0, ω_1 and ω_2 which is defined as follows

$$\begin{aligned} x_{RF}(t) = {} & A_0(t)\cos(\omega_0 t + \phi_0(t)) + A_1(t)\cos(\omega_1 t + \phi_1(t)) \\ & + A_2(t)\cos(\omega_2 t + \phi_2(t)) \end{aligned} \tag{2.4}$$

It is well-known in the literature, and it is also demonstrated in the Appendix A.1, that the *second-order* nonlinearity, i.e. $x_{RF}^2(t)$, generates following types of spurious components

- **Around DC**
  For example $a_2\frac{A_0^2(t)}{2}$,$a_2\frac{A_1^2(t)}{2}$ and $a_2\frac{A_2^2(t)}{2}$
- **At twice original signals frequencies**
  For example $a_2\frac{A_0^2(t)}{2}\cos(2\omega_0 t + 2\phi_0(t))$
- **Cross-modulations between signal pairs**
  For example $a_2 A_1(t)A_2(t)\cos\big((\omega_1+\omega_2)t + \phi_1(t) + \phi_2(t)\big)$

The *third-order* nonlinearity, i.e. $x_{RF}^3(t)$, in turn, generates following inter/cross-modulation components

- **Self-distortions**
  These components hit the original signals center frequencies e.g.
  $a_3\big(\frac{3A_0^3(t)}{4} + \frac{3A_1^2(t)A_0(t)}{2} + \frac{3A_2^2(t)A_0(t)}{2}\big)\cos(\omega_0 t + \phi_0(t))$
- **At three-times original signals frequencies**
  For example $a_3\frac{A_0^3(t)}{4}\cos(3\omega_0 t + 3\phi_0(t))$

- **Cross-modulations between original signal pairs**
  For instance $a_3\frac{3A_1^2(t)A_2(t)}{4}\cos((2\omega_1+\omega_2)t+2\phi_1(t)+\phi_2(t))$

- **Cross-modulations between all three of the original signals**
  For example $a_3\frac{6A_0(t)A_1(t)A_2(t)}{4}\cos((\omega_1-\omega_2-\omega_0)t+\phi_1(t)-\phi_2(t)-\phi_0(t))$

The above analysis can be extended, from *complex I/Q signal* perspective, when the nonlinearities take place in I/Q processing, like I/Q mixer. An example of such a scenario is provided in the Appendix A.2. Particularly, one should note that the referred derivations are designed to motivate the analysis of the nonlinearity profile in scenarios in which I and Q branches of a DCR exhibit different, yet mild, nonlinearity. As the result, the nonlinearity in the I and Q branches are considered up to third-order elements only. Three complex signals at frequencies of $\hat{\omega}_0$, $\hat{\omega}_1$ and $\hat{\omega}_2$ are assumed at the output of the I/Q downconverter. Note here that $\hat{\omega}_0$, $\hat{\omega}_1$ and $\hat{\omega}_2$ can be considered as the downconverted versions of ω_0, ω_1 and ω_2, respectively. The input of the nonlinear element in this case can be written as follow

$$\begin{aligned} x(t) &= x_I(t) + jx_Q(t) \\ &= A_0(t)e^{j(\hat{\omega}_0 t+\phi_0(t))} + A_1(t)e^{j(\hat{\omega}_1 t+\phi_1(t))} + A_2(t)e^{j(\hat{\omega}_2 t+\phi_2(t))} \end{aligned} \tag{2.5}$$

The overall complex spurious frequency profile stemming form I and Q components of the above signal passing through second-order nonlinearities in the I and Q branches with distinct characteristics, i.e. $b_2x_I^2(t)+jg_2b_2x_Q^2(t)$, can be categorized in following groups (refer to Table A.3 in Appendix).

- **Components around DC**
  For example $b_2(1+jg_2)\frac{A_0^2(t)}{2}$, $b_2(1+jg_2)\frac{A_1^2(t)}{2}$ and $b_2(1+jg_2)\frac{A_2^2(t)}{2}$

- **At ±2-times original frequencies**
  For example
  $b_2\frac{1-jg_2}{4}\frac{A_0^2(t)}{2}e^{j(2\hat{\omega}_0 t+2\phi_0(t))}$ and $b_2\frac{1-jg_2}{4}\frac{A_0^2(t)}{2}e^{-j(2\hat{\omega}_0 t+2\phi_0(t))}$

- **Cross-modulations of signal pairs**
  For example
  $b_2\frac{1-jg_2}{2}A_1(t)A_2(t)e^{j((\hat{\omega}_1+\hat{\omega}_2)t+\phi_1(t)+\phi_2(t))}$ and
  $b_2\frac{1-jg_2}{2}A_1(t)A_2(t)e^{-j((\hat{\omega}_1+\hat{\omega}_2)t+\phi_1(t)+\phi_2(t))}$

One interesting observation here is that the second-order nonlinearity in the form of $b_2x_I^2+jg_2b_2x_Q^2$ generates symmetric intermodulation and cross-modulation components around zero frequency. This is true even in case of different characteristics in I and Q branch ($g_2\neq 1$) which results in the presence of mirror frequencies components [15] on either side of the frequency axis.

The overall complex spurious frequency profile stemming form I and Q components of the signal in (2.5) passing through third-order nonlinearities with distinct characteristics, i.e. $b_3x_I^3 + jg_3b_3x_Q^3$, can, in turn, be categorized in following groups (refer to Table A.4 in the Appendix).

- **Self-distortions**
  One example of such components is
  $\frac{b_3(1+g_3)}{2}\left(\frac{3A_0^3(t)}{4} + \frac{3A_1^2(t)A_0(t)}{2} + \frac{3A_2^2(t)A_0(t)}{2}\right)e^{j(\hat{\omega}_0 t+\phi_0(t))}$

- **At ±3-times original frequencies**
  For example
  $\frac{b_3(1+g_3)}{2}\frac{A_0^3(t)}{4}e^{-j(3\hat{\omega}_0 t+3\phi_0(t))}$ and $\frac{b_3(1-g_3)}{2}\frac{A_0^3(t)}{4}e^{j(3\hat{\omega}_0 t+3\phi_0(t))}$

- **Cross-modulations of signal pairs**
  For example
  $\frac{b_3(1+g_3)}{2}\frac{3A_1^2(t)A_2(t)}{4}e^{-j((2\hat{\omega}_1+\hat{\omega}_2)t+2\phi_1(t)+\phi_2(t))}$ and
  $\frac{b_3(1-g_3)}{2}\frac{3A_1^2(t)A_2(t)}{4}e^{j((2\hat{\omega}_1+\hat{\omega}_2)t+2\phi_1(t)+\phi_2(t))}$

- **Cross-modulations of all three signals**
  For example
  $\frac{b_3(1+jg_3)}{2}\frac{6A_0(t)A_1(t)A_2(t)}{4}e^{-j((\hat{\omega}_1-\hat{\omega}_2-\hat{\omega}_0)t+\phi_1(t)-\phi_2(t)-\phi_0(t))}$ and
  $\frac{b_3(1-jg_3)}{2}\frac{6A_0(t)A_1(t)A_2(t)}{4}e^{j((\hat{\omega}_1-\hat{\omega}_2-\hat{\omega}_0)t+\phi_1(t)-\phi_2(t)-\phi_0(t))}$

Interestingly, the spurious frequency profile of the nonlinearity in the form of $b_3x_I^3 + jg_3b_3x_Q^3$ is not symmetric around the zero frequency. More precisely, when the I and Q branches of the downconverter exhibit identical third-order nonlinearities, the third-order inter/cross-modulation terms appear only at the opposite side of the zero frequency comparing to the original signals. For instance, in the above example, given $g_3 = 1$, the desired signal at $\hat{\omega}_0$ generates the intermodulation term $\frac{b_3A_0^3(t)}{4}e^{-j(3\hat{\omega}_0 t+3\phi_0(t))}$ but the intermodulation term at the original signal side of the spectrum $\frac{b_3(1-g_3)}{2}\frac{A_0^3(t)}{4}e^{j(3\hat{\omega}_0 t+3\phi_0(t))} = 0$. Nevertheless, mismatch between the third-order characteristics of I and Q branches creates extra inter/cross-modulation components at the same side of the spectrum where the original signals are located. This is apparent in the above example where, for instance, the third-order nonlinearities in I and Q branches of the downconverter result in $\frac{b_3(1+g_3)}{2}\frac{A_0^3(t)}{4}e^{-j(3\hat{\omega}_0 t+3\phi_0(t))}$ as well as $\frac{b_3(1-g_3)}{2}\frac{A_0^3(t)}{4}e^{j(3\hat{\omega}_0 t+3\phi_0(t))}$ when $g_3 \neq 1$. There is also another crucial difference compared to the earlier second-order nonlinearity, related to the spurious signal component(s) at the original center-frequency $\hat{\omega}_0$. While the second-order case is free from this "self-distortion" such a spurious component is indeed there in the third-order case.

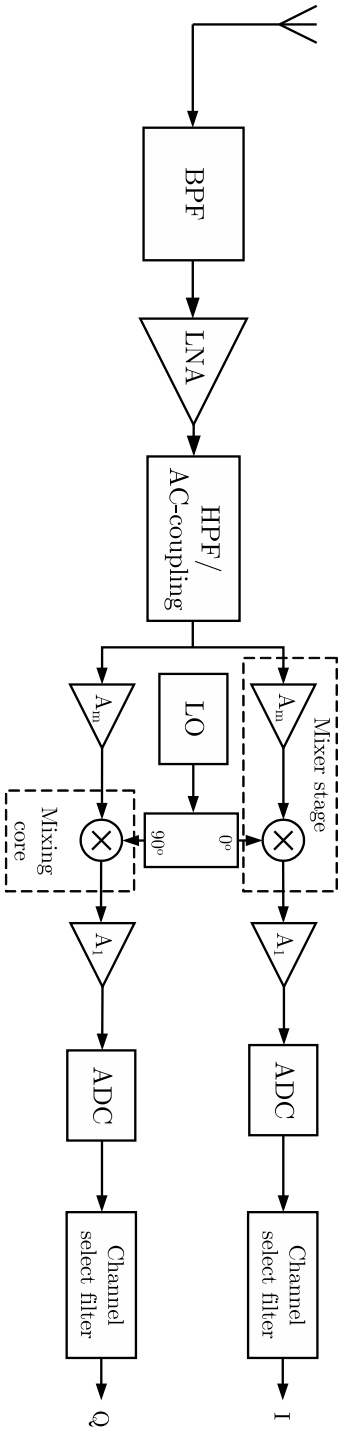

Figure 2.4: Generic schematic for DCR. This figure is detailed to depict the components contributing to odd-/even-order nonlinearity interference profile.

2.3 Inter/Cross-modulation Distortion in Direct-conversion Receivers

To study the intermodulation distortion profile in wideband DCR, it is necessary first to recognize the nonlinearity sources in this type of receiver. For this purpose a generic schematic of a wideband DCR is presented in Fig. 2.4. It should be noted that, the depicted structure by no means represents the complete front-end chain of a wideband DCR as it is only detailed to represent major sources of spurious frequency components. In this structure, the weak RF signal which is picked up by the antenna is amplified heavily before reaching the analogue-to-digital converter (ADC). The overall required gain for the signal to be conditioned for sampling and digitization can mount to tens of dBs. This gain is provided by amplifiers in different stages in the front-end chain, namely after antenna by low-noise amplifier (LNA), before mixing core and finally before ADC [6, 14]. The following subsections are dedicated to the discussions on the interference profile stemming from nonlinearity in these amplification stages.

One more important detail in Fig. 2.4 is that, *the mixing core* assumes gain one and the amplification part of the mixing stage is presented as a separate component. This is to motivate the discussion on distinct spurious frequency components which is generated by the mixing core. The discussion on this topic is also included in this chapter.

2.3.1 Nonlinearity in LNA

The first component that contributes to the nonlinearity-born interference in DCR is LNA. Basically, LNA is a high gain amplifier with a low noise figure (NF) [19, 62] which is placed after the antenna in telecommunication receivers. The low NF and the high gain of LNA are crucial to achieve low NF in the overall receiver chain and provide the subsequent downconversion stages in the receiver with adequately amplified signal and proper signal-to-noise ratio (SNR), of course, given the acceptable SNR at the LNA input. At the same time, LNA should support high dynamic range [19] as to be able to handle weak and relatively strong signals without generating spurious frequency components. This high dynamic range is of utmost importance, and equally hard/expensive to achieve, specifically in the context of multicarrier/multichannel direct conversion receivers in which the power difference between desired signal and so called blockers, i.e., the strong signals in the same band which is picked up by the antenna, can amount to several tens of dBs [6, 14, 19]. Failing to provide adequate LNA with proper dynamic range for such receivers results in odd- and even-order harmonics and intermodulation terms which are likely, depending on the blockers and desired signal frequencies, to hit the desired signal band.

To study the nonlinear *interference* profile of a mildly nonlinear LNA lets assume the signal model for the input of the LNA is the bandpass signal model similar to (2.4) and invoke on the derived inter/cross-modulation profile which is presented in the Appendix Section A.1 and described and summerized in the previous section. Now, it is established that the second-order intermodulations of each blocker fall at twice the blocker frequency as well as close to DC, for instance blocker at ω_1 generates $\frac{A_1^2(t)}{2}$ and $a_2\frac{A_1^2(t)}{2}\cos(2\omega_1 t + 2\phi_1(t))$. The DC components, stemming from LNA, are rejected by the AC coupling/bandpass filter between the LNA and subsequent mixer stage [6,32]. Moreover, the LNA-generated intermodulation terms at twice the blocker frequencies as such are not likely to interfere with the desired signal. Nevertheless, given the even-order nonlinearity characteristics of concatenated mixer stage, these components generate DC interfering intermodulation components at the mixer output (Fig. 2.5). These intermodulation terms in most practical cases are small and negligible. Otherwise, this problem can be circumvented by rejecting these high frequency terms after the LNA stage. All in all, we can conclude that the effect of the second(even)-order interference generated by LNA in one blocker scenario is considered negligible.

An LNA second-order cross-modulations terms stemming from *multiple* blockers are also categorically neglected in literature, as these cross-modulation terms hit frequencies far from the desired band, considering the bandwidth of the state-of-the-art receivers. For instance in the two-blocker example provided in the Appendix, the pairs of blockers second-order cross-modulation terms $a_2A_1(t)A_2(t)\cos\big((\omega_1+\omega_2)t+\phi_1(t)+\phi_2(t)\big)$ and $a_2A_1(t)A_2(t)\cos\big((\omega_1-\omega_2)t+\phi_1(t)-\phi_2(t)\big)$ are far from the desired signal band at ω_0 as the former component hits a much higher frequency than ω_0 and the latter component appears around DC. This conclusion is also valid for the cross-modulations between the desired signal and the blockers such as $a_2A_1(t)A_0(t)\cos\big((\omega_1+\omega_0)t+\phi_1(t)+\phi_0(t)\big)$ and $a_2A_1(t)A_0(t)\cos\big((\omega_1-\omega_0)t+\phi_1(t)-\phi_0(t)\big)$. One should note that the cross-modulation terms at $\omega_1-\omega_2$ hit the desired signal at ω_0 if $\omega_1 \gg \omega_2$ (Fig. 2.6) which in turn means the band that is amplified by LNA should be wide enough to capture both blockers which are located far from each other. This scenario is, certainly, plausible only considering the emerging concepts such as cognitive radio [63] with the decade-wideband receivers and therefore such intermodulation interference components should be considered in the second(even)-order nonlinearity-born spurious frequency profile of such radio receivers [6].

The third-order LNA intermodulation terms in the form of $a_3\frac{A_0^3(t)}{4}\cos(3\omega_0 t + 3\phi_0(t))$ hit the frequencies at three times the blocker frequencies which, again, with the current bandwidth for radio receivers are not likely to hit the desired signal band. Another set of inter/cross-modulation components stemming from third-order nonlinearity appear around the blockers frequencies

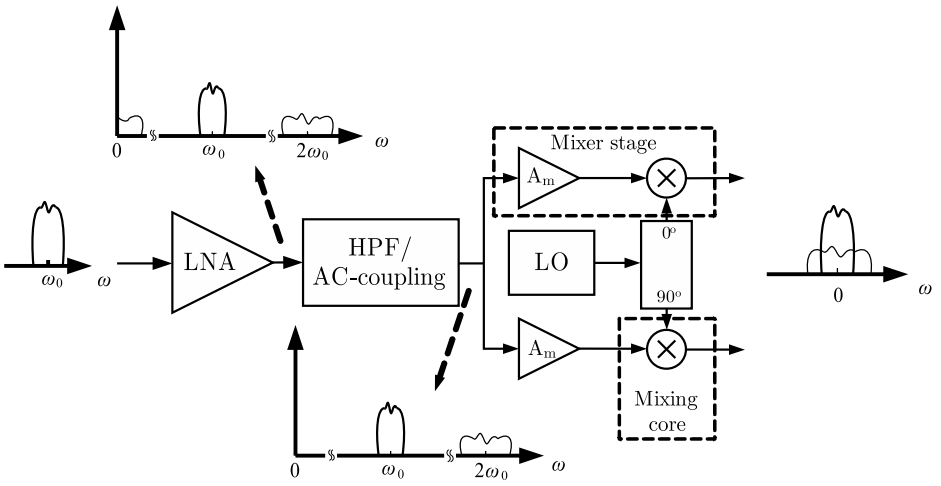

Figure 2.5: Interference generation as a result of LNA second-order (even-order) harmonics downconversion.

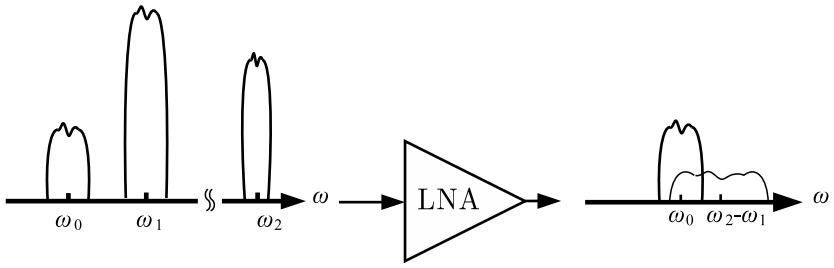

Figure 2.6: Second(even)-order cross-modulation interference in case of multiple blockers (here 2 blockers). In this scenario $\omega_2 - \omega_1$ should be close enough to ω_0 for the IMD term to overlap with the desired signal. Only positive frequencies are depicted here.

as self-distortion. Example of such a component is $a_3\big(\frac{3A_1^3(t)}{4} + \frac{3A_2^2(t)A_1(t)}{2} + \frac{3A_0^2(t)A_1(t)}{2}\big)\cos(\omega_1 t + \phi_1(t))$. Of course, the desired signal, too, suffers such self-distortion components which ultimately affect the detection of the desired signal symbols. But this type of interference is out of scope of this manuscript as we are concerned with only the interferences which are originated from the blockers. In turn, the third(odd)-order cross-modulation of multiple blockers hit in-band frequencies which can be occupied by the desired signal (Fig. 2.7). For instance, two blockers with center frequency of $f_1 = 2.1$ GHz and $f_2 = 2.2$ GHz can generate intermodulation terms at $2f_1 - f_2 = 2$ GHz and $f_1 - 2f_2 = 2.3$ GHz which can be well occupied by the desired signal.

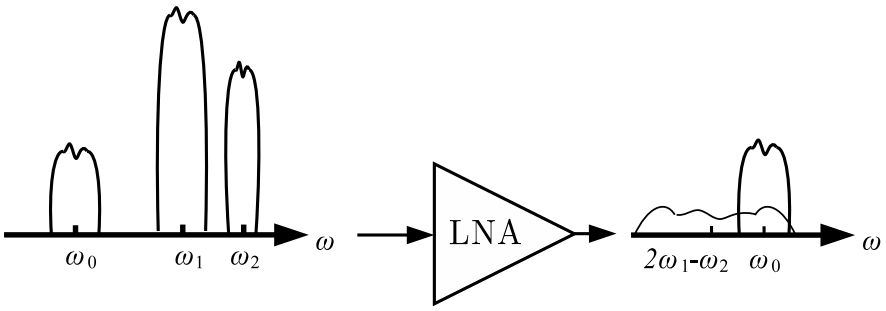

Figure 2.7: Cross-modulation interference generation as a result of LNA third-order (odd-order) nonlinearity in presence of multiple blockers (here 2 blockers). Only positive frequencies are depicted here.

2.3.2 Nonlinearities in Mixer and Subsequent Amplifier Stages

The RF signal after the LNA enters the mixing stage. In this stage the RF signal is further amplified and then is frequency translated to an IF or baseband by multiplying the RF signal to a local oscillator (LO) signal (Fig. 2.4). The amplification stage here generates inter/crossmodulation interferences similar to LNA. However, these interference terms can be more damaging compared to the ones generated by LNA as the signals entering the mixer amplification stage are already amplified by LNA therefore the interfering intermodulation terms, both even and odd-order terms, are much stronger compared to the ones stemming from LNA.

The mixer stage, generally, is followed by band-limitation filtering implementing part or all of receiver selectivity, depending on the radio architecture [14]. In the context of multichannel/multicarrier DCR, the output of this lowpass filter includes the desired signal as well as possible strong blockers. The desired signal, then, is selected from the downconverted band in the digital domain. However, before sampling and digitization the downconverted band, typically, requires another round of amplification in both I and Q paths [14]. The amplifiers in these two paths, similar to LNA, exhibit mild nonlinearity and can be modeled by third order polynomials. In most practical settings the nonlinearity characteristics of amplifiers in I and Q branches are different. This difference is reflected in the polynomial model in the form of different coefficients for I and Q nonlinearity models. These polynomial models for I and Q branches read

$$\begin{aligned} y_I(t) &= b_1 x_I(t) + b_2 x_I^2(t) + b_3 x_I^3(t) \\ y_Q(t) &= g_1 b_1 x_Q(t) + g_2 b_2 x_Q^2(t) + g_3 b_3 x_Q^3(t) \end{aligned} \tag{2.6}$$

The inter/cross-modulation profile of such nonlinearity models are already analyzed from overall complex signal perspective in the Appendix Section

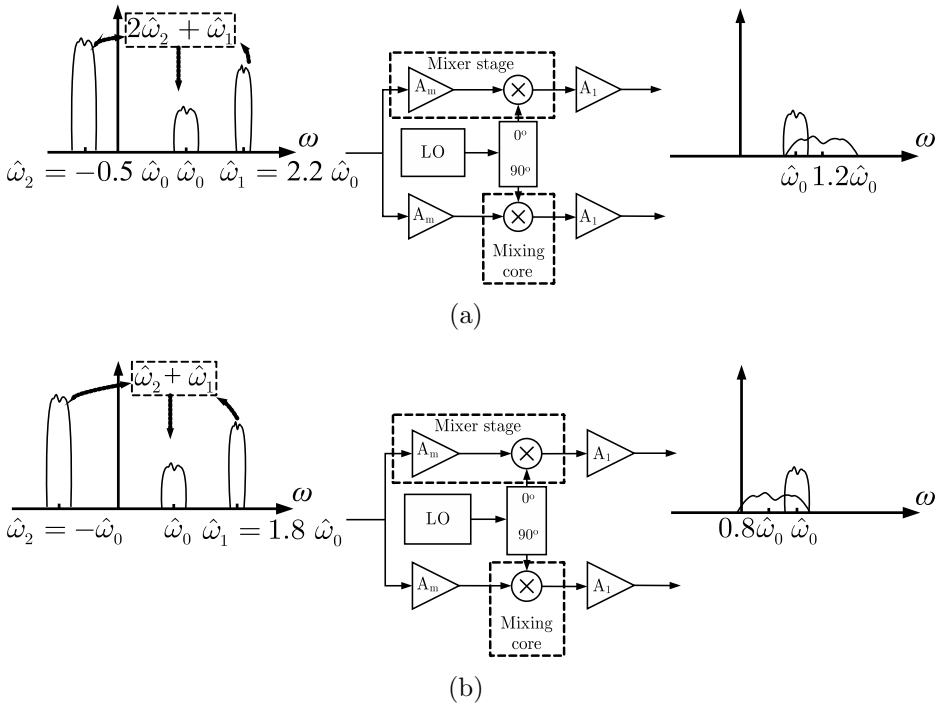

Figure 2.8: Cross-modulation interference generation as a result of I and Q third (odd)-order (a) and second (even)-order (b) nonlinearity in presence of multiple blockers (here 2 blockers). In these example the two blockers are located at $\hat{\omega}_1 = 2.2\hat{\omega}_0$ and $\hat{\omega}_2 = -0.5\hat{\omega}_0$ for the third-order case and $\hat{\omega}_1 = 1.8\hat{\omega}_0$ and $\hat{\omega}_2 = -\hat{\omega}_0$ for the second-order case. The baseband/IF version of the spectrums at the input and output are depicted.

A.2 and Subsection 2.2 for one desired signal and two blockers at $\hat{\omega_0}$, $\hat{\omega_1}$ and $\hat{\omega_2}$ (refer to signal model in (2.5)), respectively. Now, keeping in mind that the desired signal and both blockers in the provided analysis are located at much lower frequencies in compare with LNA case, it is easy to see that the second-order intermodulation terms such as $b_2(1+jg_2)\frac{A_1^2(t)}{2}$ and $b_2\frac{1-jg_2}{4}\frac{A_0^2(t)}{2}e^{j(2\hat{\omega}_0 t+2\phi_0(t))}$ can fall on top of the desired signal band. Moreover, again in contrast to LNA case, the second-order cross-modulation between blockers such as $b_2\frac{1-jg_2}{2}A_1(t)A_2(t)e^{j((\hat{\omega}_1+\hat{\omega}_2)t+\phi_1(t)+\phi_2(t))}$ are also capable of generating interference on the desired signal band. In addition, the third-order elements of the nonlinearity model can generate hosts of inter/cross-modulation interference similar to LNA third-order nonlinearity profile. Two examples, on how cross-modulation of two blockers can hit the desired signal band are depicted for third- and second-order case in Fig.2.8(a) and Fig 2.8(b), respectively.

In Chapter 3 we revisit this particular problem, i.e. the last stage nonlin-

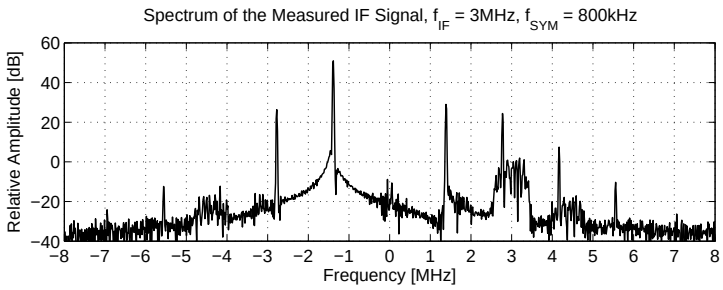

Figure 2.9: Measured IF signal spectrum with sinusoidal blocker at −1.4 MHz. The desired signal is QPSK modulated and located at +3 MHz.

earity after the I/Q downconversion, and propose a novel DSP interference cancellation (IC) method to mitigate the interference components resulting from the last-stage nonlinearity as well as LNA. This method, eliminates the need for highly selective channel selecting filters early in the receiver chain which is much desirable in future multi-standard radio receivers based on SDR and CR concepts. For now and to motivate the reader, the effect of the last stage amplification nonlinearity is demonstrated through a laboratory measurement example. In this experiment, the desired signal is quadrature phase-shift key (QPSK) modulated with 800 KHz symbol rate and located at 103 MHz RF carrier. I/Q downconversion with 100 MHz LO signal(s) translates the desired signal to $\hat{f}_0 = 3$ MHz IF. The strong blocker in this experiment is a sinusoidal at 98.6 MHz RF frequency, therefore the blocker after the downconversion falls at $\hat{f}_1 = -1.4$ MHz. The measured IF spectrum from Fig.2.9 evidences clear second-order distortion on top of the desired signal at $-2\hat{f}_1 = 2.8$ MHz which evidently results in high detection error rate for the desired signal (Fig.2.10). The measured spectrum also verifies the signal analysis models in Section 2.2, including symmetric nature of the even-order I/Q nonlinearity as the second-order nonlinearity in this experiment generates harmonic term at −2.8 MHz as well as 2.8 MHz. Furthermore, the non-symmetric nature of the odd-order I/Q nonlinearity is evident in Fig. 2.9 as the blocker generates a harmonic term only at $-3\hat{f}_1$ =4.2 MHz and there is no harmonic term at the corresponding mirror frequency. The cross-modulation terms from second-order nonlinearities are also visible in this figure, e.g. $\pm(\hat{f}_0 + \hat{f}_1) = \pm$ 1.6 MHz, $\pm(\hat{f}_0 - \hat{f}_1) = \pm$ 4.4 MHz. Finally, the fourth-order nonlinearity in the I/Q of the downconversion paths generates symmetric harmonic terms at $\pm 4\hat{f}_1 = \pm$ 5.6 MHz.

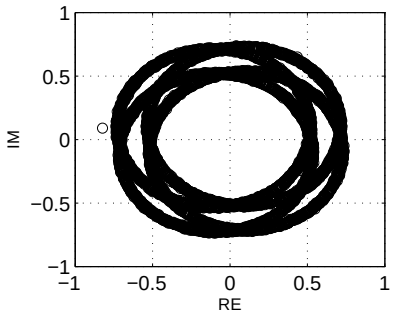

Figure 2.10: Effect of the harmonics and intermodulation interference on the baseband desired signal observations at symbol rate.

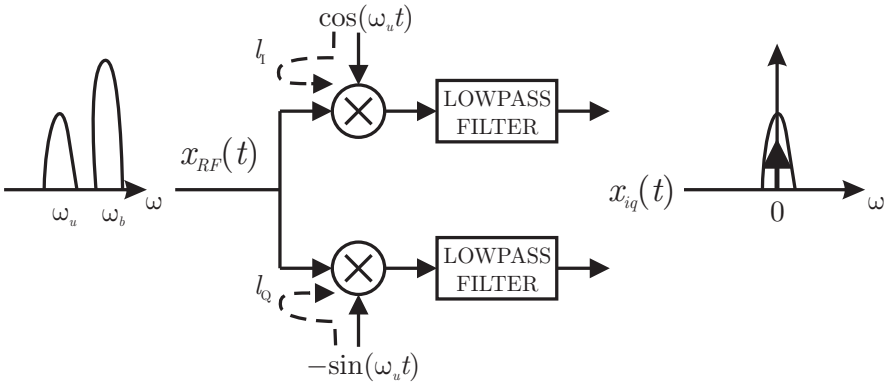

(a)

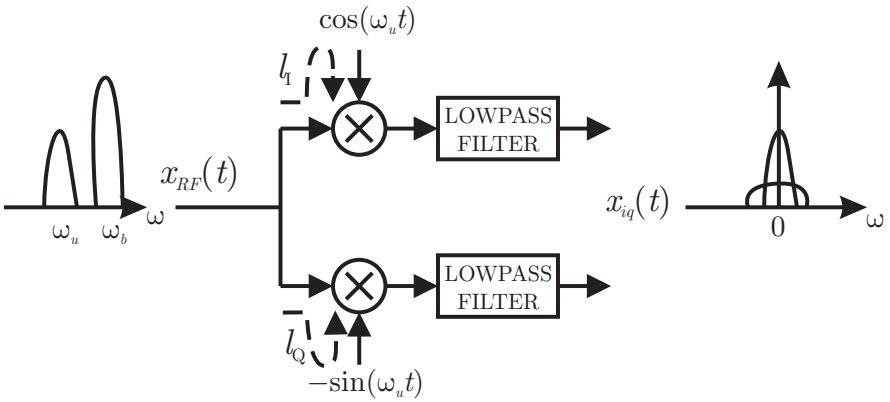

(b)

Figure 2.11: (a) Static offset as a result of LO signal self-mixing, (b) Dynamic offset as a result of the input RF signal self-mixing. Only the positive frequencies are depicted in the RF spectrum.

2.3.3 RF/LO leakage in mixing core

The mixing core, basically, translates the frequency of the RF signal to a baseband/IF frequency by multiplying the RF signal with a tone signal which, in turn, is generated by LO. The three ports of a mixing core, i.e., RF, IF and LO need to be completely isolated from each other, otherwise leakage and eventually self-mixing of LO and RF signals generates even-order intermodulation components around zero frequency, also known as *static and dynamic DC-offset* respectively [6, 13, 14, 31]. In the context of direct conversion receivers these DC-offset components can interfere with the desired signal given the desired signal is located at the same frequency range. In the following we give more insights into these offset generation mechanisms and the significance of this type of interference in the context of DCR.

Static DC offset

Consider a DCR which suffers from static offset due to self-mixing of LO signals (Fig. 2.11(a)). Received RF signal, $x_{RF}(t)$, can in general be written as

$$\begin{aligned} x_{RF}(t) &= 2\mathrm{Re}\Big[x_u(t)e^{j\omega_u t} + x_b(t)e^{j\omega_b t}\Big] \\ &= \Big[x_u(t)e^{j\omega_u t} + x_b(t)e^{j\omega_b t}\Big] \\ &+ \Big[x_u^*(t)e^{-j\omega_u t} + x_b^*(t)e^{-j\omega_b t}\Big] \end{aligned} \tag{2.7}$$

where $x_u(t)$ is the baseband equivalent desired signal and $x_b(t)$ is the corresponding baseband equivalent of the RF blocker located $\omega_b = \omega_u + \Delta\omega$.

To model the finite isolation between the mixers LO and RF ports, we use the leakage coefficients l_I and l_Q. In the ideal case, these leakage coefficients are zero representing infinite attenuation while in practice, the isolation is in the order of 40 to 60dB [14]. Considering then first the leakage of the LO signal(s) into the RF mixer input port(s), the down-converted I/Q signal $x_{down}(t)$ can be written as

$$\begin{aligned} x_{down}(t) = &\Big[\big(x_{RF}(t) + l_I\cos(\omega_u t)\big)\cos(\omega_u t)\Big] \\ &- j\Big[\big(x_{RF}(t) - l_Q\sin(\omega_u t)\big)\sin(\omega_u t)\Big] \end{aligned} \tag{2.8}$$

Subsequently, lowpass-filtered signal $x_{iq}(t)$ can be written as

$$x_{iq}(t) = x_u(t) + (l_\mathrm{I} + jl_\mathrm{Q}) \tag{2.9}$$

It is clear from (2.7) that the LO leakage generates static DC-offset on top of the desired signal $x_u(t)$ at the baseband. There are several methods available in the literature for mitigating this type of interference [13, 14, 31].

Dynamic DC offset

The process which yields the dynamic offset is presented in Fig. 2.11(b). In this case, the finite isolation between the RF and LO causes the self-mixing of RF signals. The downconverted signal $x_{down}(t)$ in this case is

$$\begin{aligned} x_{down}(t) &= x_{RF}(t)[\cos(\omega_u t) + l_I x_{RF}(t)] \\ &\quad + j x_{RF}(t)[-\sin(\omega_u t) + l_Q x_{RF}(t)] \\ &= x_{RF}(t)e^{-j\omega_u t} + (l_I + j l_Q)x_{RF}^2(t) \end{aligned} \tag{2.10}$$

where now l_I and l_Q represent the leakage attenuation of the RF into the mixer LO port. Applying lowpass filtering on the above signal in (2.10) yields then

$$x_{iq}(t) = x_u(t) + (l_I + j l_Q)(|x_b(t)|^2 + |x_u(t)|^2) \tag{2.11}$$

Thus the desired signal $x_u(t)$ is clearly interfered by its own squared-envelope as well as by the squared-envelope of the RF blocker. Assuming next that the desired signal $x_u(t)$ is significantly weaker than $x_b(t)$, (2.11) can be written as

$$x_{iq}(t) \approx x_u(t) + (l_I + j l_Q)\,|x_b(t)|^2 \tag{2.12}$$

Thus contrary to the static offset, dynamic offset shown in (2.11) and (2.12) in terms of the blocker squared-envelope, can degrade the quality of the desired signal $x_u(t)$, specially in cases of strong RF blocker. This is because the interference in (2.12) is proportional to $|x_b(t)|^2$ and thus the interference power in then proportional to $|x_b(t)|^4$. Based on this quadratic relation between the RF blocking signal and the generated dynamic offset interference component, it is clear that the interference effect is strongly dependent on the RF power of the original blocker as well as the leakage coefficients l_I and l_Q.

Based on above discussion two rather straight forward solutions can be conceived to remedy the dynamic DC offset issue. The first solution is to improve the isolation between different ports of the mixing core and the second is to use highly selective filters to suppress the interfering blockers already at RF stage. Both these methods are costly particularly in the context of state-of-the-art multi-front-end receiver designs with multiple downconversion paths. Moreover, the latter method is not an attractive option in future SDR and CR concepts in which flexible channel selection filtering is expected to be performed as late as possible in the receiver chain and in DSP regime. Thus, a digital signal processing based solution for offset interference suppression is described in Chapter 4.

CHAPTER 3

DIGITAL CANCELLATION OF INTERMODULATION IN DIRECT-CONVERSION RECEIVERS

In this chapter, an adaptive IC method to suppress inter/cross-modulation distortions caused by strong blocking signals on top of the desired signal bands as a result of LNA and last-stage amplification nonlinearities in DCR structure is introduced. The basics of operation for this IC method are also discussed. More detailed analysis and presentations on this method can be found in [P1] and [P4].

3.1 Basics of Interference Canceller Operation

In Chapter 2, the essential inter/cross-modulation distortion models from the complex communications waveforms point of view were introduced. Here, we simply assume that a collection of frequency channels is I/Q downconverted as a whole and some of the downconverted strong signals create interference on top of the weaker signals as the result of odd- and even- nonlinearities in the I/Q branches of the downconverter. Moreover, based on the discussion in Section 2.3.1, it is assumed that the LNA contributes to the interference profile only through odd-order cross-modulation terms, therefore the even-order inter/cross-modulation terms stemming from LNA are ignored. The basic compensation structure is presented in Fig. 3.1. The idea is to consider the

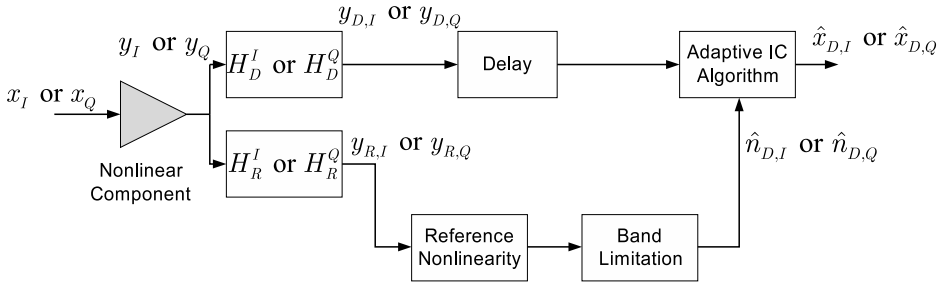

Figure 3.1: Proposed compensation structure. The upper branch captures the desired signal band and the lower branch generates an interference reference. These two signals are then processed by an adaptive interference canceller to suppress the nonlinear distortion effects from the signal of interest

detection of the interesting signals on a channel-by-channel basis, such that the band-split filtering stage first separates the desired signal band, around $\hat{\omega}_0$, and all the other signals. These effective filtering functions are denoted by H_D^I, H_D^Q, H_R^I and H_R^Q with their corresponding impulse responses $h_D^I(n)$, $h_D^Q(n)$, $h_R^I(n)$ and $h_R^Q(n)$, respectively. Here, "D" refers to "desired" and "R" to "reference" signal branches and superscript I and Q signify whether the filter belongs to I or Q branch. As the entire IC algorithm is implemented in digital domain discrete time notations are employed to describe the behavior of the compensation algorithm. Notice also that the processing depicted in Fig. 3.1 is carried out separately for the physical I and Q signal branches.

Filtering the nonlinear component output, the signals at the band-splitting filters output and for I and Q branches reads

$$\begin{aligned} y_{D,I}(n) &= h_D^I(n) * y_I(n) \approx x_{D,I}(n) + n_{D,I}(n) \\ y_{R,I}(n) &= h_R^I(n) * y_I(n) \approx x_{R,I}(n) + n_{R,I}(n) \\ y_{D,Q}(n) &= h_D^Q(n) * y_Q(n) \approx x_{D,Q}(n) + n_{D,Q}(n) \\ y_{R,Q}(n) &= h_R^Q(n) * y_Q(n) \approx x_{R,Q}(n) + n_{R,Q}(n) \end{aligned} \tag{3.1}$$

Here $y_I(n)$ and $y_Q(n)$ are the outputs of the nonlinear elements in I and Q branches of the I/Q downconverter, respectively. Moreover, in (3.1), $x_{D,I}(n)$, $x_{D,Q}(n)$, $x_{R,I}(n)$ and $x_{R,Q}(n)$ are the I/Q components of the original signals in the desired band and the reference bands, respectively. The spurious frequencies stemming from nonlinear component in the desired band and the reference band are denoted by $n_{D,I}(n)$, $n_{D,Q}(n)$, $n_{R,I}(n)$ and $n_{R,Q}(n)$, respectively. The idea in this structure is to regenerate the distorting inter/cross-modulation components $n_{D,I}(n)$ and $n_{D,Q}(n)$ by feeding the reference branch signals $y_{R,I}(n)$ and $y_{R,Q}(n)$ into a model of the nonlinear process (Fig.3.1).

Naturally, the nonlinear model generates the interfering as well as non-interfering inter/cross-modulation terms, therefore a band-limiter filter is required to isolate the interfering inter/cross-modulation terms, i.e. $\hat{n}_{D,I}(n)$ and $\hat{n}_{D,Q}(n)$ (Fig.3.1). After the generation of these terms an adaptive filtering stage is applied to "scale" the reproduced frequency components properly before being subtracted from the desired signal observation. The adaptive filter coefficients vectors, $\mathbf{w}_I(n) = [w_{0,I}(n), w_{1,I}(n), \ldots, w_{L-1,I}(n)]^T$ and $\mathbf{w}_Q(n) = [w_{0,Q}(n), w_{1,Q}(n), \ldots, w_{L-1,Q}(n)]^T$ can be adjusted, e.g., to minimize the power of the compensator output using the well-known least-mean-square (LMS) algorithm [64] as follows

$$\begin{aligned} \mathbf{w}_I(n+1) &= \mathbf{w}_I(n) + \mu\hat{\mathbf{n}}_{D,I}(n)\hat{x}_{D,I}(n) \\ &= \mathbf{w}_I(n) + \mu\hat{\mathbf{n}}_{D,I}(n)\big[y_{D,I}(n) - \mathbf{w}_I^T(n)\hat{\mathbf{n}}_{D,I}(n)\big] \\ &= \mathbf{w}_I(n) + \mu\hat{\mathbf{n}}_{D,I}(n)\big[x_{D,I}(n) + n_{D,I}(n) - \mathbf{w}_I^T(n)\hat{\mathbf{n}}_{D,I}(n)\big] \end{aligned} \tag{3.2}$$

and

$$\begin{aligned} \mathbf{w}_Q(n+1) &= \mathbf{w}_Q(n) + \mu\hat{\mathbf{n}}_{D,Q}(n)\hat{x}_{D,Q}(n) \\ &= \mathbf{w}_Q(n) + \mu\hat{\mathbf{n}}_{D,Q}(n)\big[y_{D,Q}(n) - \mathbf{w}_Q^T(n)\hat{\mathbf{n}}_{D,Q}(n)\big] \\ &= \mathbf{w}_Q(n) + \mu\hat{\mathbf{n}}_{D,Q}(n)\big[x_{D,Q}(n) + n_{D,Q}(n) - \mathbf{w}_Q^T(n)\hat{\mathbf{n}}_{D,Q}(n)\big] \end{aligned} \tag{3.3}$$

where outputs of the interference canceller in I and Q branches are $\hat{x}_{D,I}(n)$ and $\hat{x}_{D,Q}(n)$. Moreover, the adaptive filter input vectors for I and Q branches are $\hat{\mathbf{n}}_{D,I}(n) = [\hat{n}_{D,I}(n), \hat{n}_{D,I}(n-1), \ldots, \hat{n}_{D,I}(n-L+1)]^T$ and $\hat{\mathbf{n}}_{D,Q}(n) = [\hat{n}_{D,Q}(n), \hat{n}_{D,Q}(n-1), \ldots, \hat{n}_{D,Q}(n-L+1)]^T$, respectively. Also, μ is the step-size for the coefficients update of the LMS algorithm. Note that, in case the nonlinear device doesn't exhibit any memory here the adaptive filters in I and Q branches are reduced to one-tap. In practical implementation, the effective processing of second-order, third-order, etc. interference can be carried out individually, by having parallel reference signal branches (reference nonlinearity and adaptive filter stage) for each order of interest i.e. separate $\hat{n}_D(n)$ is generated for different orders of nonlinearity. In this way, the needed reference polynomials are simply quadratic, cubic, etc., operators, in the simplest case, and the corresponding adaptive filters process each order effects separately. Thus, in general, it should be noted that no detailed model of the nonlinear physical front-end is necessarily needed. The reference nonlinearity section simply regenerates the interfering frequency components which are then further modified by the online adaptive filter stage, controlling the actual interference cancellation process. In general, by adjusting the band-split filtering stage separating desired signal from the rest of the spectrum, this method is applicable independently of the position of the desired signal.

To establish a concrete understanding on the operation of this IC algorithm, two examples from the operation of this algorithm to compensate the

effects of a nonlinear LNA and nonlinearity in I/Q branches of a downconverter are presented here.

3.1.1 Case A: LNA Nonlinearity

In the first case, let's assume an LNA with a third-order polynomial characteristics as follows

$$y_{RF}(t) = a_1 x_{RF}(t) + a_2 x_{RF}^2(t) + a_3 x_{RF}^3(t) \tag{3.4}$$

where a_1, a_2 and a_3 are real-valued coefficients. The signal model for the LNA input is the three-signal model, which is used in previous chapter, including a desired signal and two blockers as follows

$$\begin{aligned} x_{RF}(t) = {} & A_0(t)\cos(\omega_0 t + \phi_0(t)) + A_1(t)\cos(\omega_1 t + \phi_1(t)) \\ & + A_2(t)\cos(\omega_2 t + \phi_2(t)) \end{aligned} \tag{3.5}$$

According to the detailed derivations for the inter/cross-modulations of such signal model which are presented in Appendix A.1, $y_{RF}(t)$ includes hosts of spurious components resulting from second- and third-order nonlinearities. On the other hand, it is already established in Chapter 2 that the dominant interference components caused by LNA on top of the desired signal are mainly the third(odd)-order cross-modulations of the blockers. Here, we assume $2\omega_1 - \omega_2 \approx \omega_0$ which means cross-modulation term $a_3 \frac{3A_1^2(t)A_2(t)}{4}\cos((2\omega_1 - \omega_2)t + 2\phi_1(t) - \phi_2(t))$ is the interfering term. Let's also assume that the nonlinearity-generated spurious components outside the desired band are significantly weaker compare to the blockers. Considering the above assumptions, the output of the LNA follows

$$\begin{aligned} y_{RF}(t) \approx {} & a_1 A_0(t)\cos(\omega_0 t + \phi_0(t)) \\ & + a_3 \frac{3A_1^2(t)A_2(t)}{4}\cos((2\omega_1 - \omega_2)t + 2\phi_1(t) - \phi_2(t)) \\ & + a_1 A_1(t)\cos(\omega_1 t + \phi_1(t)) + a_1 A_2(t)\cos(\omega_2 t + \phi_2(t)) \end{aligned} \tag{3.6}$$

The I/Q downconverted version of the LNA output, $y(t)$, then reads

$$\begin{aligned} y(t) \approx {} & a_1 A_0(t) e^{j(\hat{\omega}_0 t + \phi_0(t))} + a_3 \frac{3A_1^2(t)A_2(t)}{4} e^{j((2\hat{\omega}_1 - \hat{\omega}_2)t + 2\phi_1(t) - \phi_2(t))} \\ & + a_1 A_1(t) e^{j(\hat{\omega}_1 t + \phi_1(t))} + a_1 A_2(t) e^{j(\hat{\omega}_2 t + \phi_2(t))} \end{aligned} \tag{3.7}$$

Note that, the I/Q branches of the downconverter are assumed to be linear in this example. The discrete-time I/Q components of $y(t)$, i.e. $y_I(n)$ and

$y_Q(n)$, are written as follows

$$\begin{aligned} y_I(n) &= a_1 A_0(nT_s)\cos\left(\hat{\omega}_0 nT_s + \phi_0(nT_s)\right) \\ &\quad + a_3\frac{3A_1^2(nT_s)A_2(nT_s)}{4}\cos\left((2\hat{\omega}_1 - \hat{\omega}_2)nT_s + 2\phi_1(nT_s) - \phi_2(nT_s)\right) \\ &\quad + a_1 A_1(nT_s)\cos\left(\hat{\omega}_1 nT_s + \phi_1(nT_s)\right) + a_1 A_2(nT_s)\cos\left(\hat{\omega}_2 nT_s + \phi_2(nT_s)\right) \\ y_Q(n) &= a_1 A_0(nT_s)\sin\left(\hat{\omega}_0 nT_s + \phi_0(nT_s)\right) \\ &\quad + a_3\frac{3A_1^2(nT_s)A_2(nT_s)}{4}\sin\left((2\hat{\omega}_1 - \hat{\omega}_2)nT_s + 2\phi_1(nT_s) - \phi_2(nT_s)\right) \\ &\quad + a_1 A_1(nT_s)\sin\left(\hat{\omega}_1 nT_s + \phi_1(nT_s)\right) + a_1 A_2(nT_s)\sin\left(\hat{\omega}_2 nT_s + \phi_2(nT_s)\right) \end{aligned} \tag{3.8}$$

Here, T_s is the sampling time. Afterward, the signals $y_I(n)$ and $y_Q(n)$ are split into desired and reference bands. The signals in the desired and reference branches of IC algorithm reads from (3.1)

$$\begin{aligned} y_{D,I}(n) &\approx x_{D,I}(n) + n_{D,I}(n) \\ &= a_1 A_0(nT_s)\cos\left(\hat{\omega}_0 nT_s + \phi_0(nT_s)\right) \\ &\quad + a_3\frac{3A_1^2(nT_s)A_2(nT_s)}{4}\cos\left((2\hat{\omega}_1 - \hat{\omega}_2)nT_s + 2\phi_1(nT_s) - \phi_2(nT_s)\right) \\ y_{D,Q}(n) &\approx x_{D,Q}(n) + n_{D,Q}(n) \\ &= a_1 A_0(nT_s)\sin\left(\hat{\omega}_0 nT_s + \phi_0(nT_s)\right) \\ &\quad + a_3\frac{3A_1^2(nT_s)A_2(nT_s)}{4}\sin\left((2\hat{\omega}_1 - \hat{\omega}_2)nT_s + 2\phi_1(nT_s) - \phi_2(nT_s)\right) \\ y_{R,I}(n) &\approx x_{R,I}(n) + n_{R,I}(n) \approx x_{R,I}(n) \\ &= a_1 A_1(nT_s)\cos\left(\hat{\omega}_1 nT_s + \phi_1(nT_s)\right) + a_1 A_2(nT_s)\cos\left(\hat{\omega}_2 nT_s + \phi_2(nT_s)\right) \\ y_{R,Q}(n) &\approx x_{R,Q}(n) + n_{R,Q}(n) \approx x_{R,Q}(n) \\ &= a_1 A_1(nT_s)\sin\left(\hat{\omega}_1 nT_s + \phi_1(nT_s)\right) + a_1 A_2(nT_s)\sin\left(\hat{\omega}_2 nT_s + \phi_2(nT_s)\right) \end{aligned} \tag{3.9}$$

One should note that the spurious components on the reference branches are assumed to be negligible comparing to the blockers, hence $\mathbb{E}[|n_{R,I}(n)|^2] \ll \mathbb{E}[|x_{R,I}(n)|^2]$ and $\mathbb{E}[|n_{R,Q}(n)|^2] \ll \mathbb{E}[|x_{R,Q}(n)|^2]$. In order to regenerate the interfering component on top of the desired signal the isolated blockers in $y_{R,I}(n)$ and $y_{R,Q}(n)$ are passed through a simple cubic term. The output of the cubic element, then, reads

$$\begin{aligned} &y_{R,I}^3(n) = \\ &\frac{3a_1^3 A_1^2(nT_s)A_2(nT_s)}{4}\cos\left((2\hat{\omega}_1 - \hat{\omega}_2)nT_s + 2\phi_1(nT_s) - \phi_2(nT_s)\right) + \mathrm{Re}[\Xi_3^{IM/CM}] \\ &y_{R,Q}^3(n) = \\ &\frac{3a_1^3 A_1^2(nT_s)A_2(nT_s)}{4}\sin\left((2\hat{\omega}_1 - \hat{\omega}_2)nT_s + 2\phi_1(nT_s) - \phi_2(nT_s)\right) + \mathrm{Im}[\Xi_3^{IM/CM}] \end{aligned} \tag{3.10}$$

where all the third-order complex inter/cross-modulation terms outside the desired band, i.e. around $\hat{\omega}_0$, are denoted by $\Xi_3^{IM/CM}$. The outputs of the band limiting filters in I and Q branches, $\hat{n}_{D,I}(n)$ and $\hat{n}_{D,Q}(n)$, then read

$$\hat{n}_{D,I}(n) \approx \frac{3a_1^3 A_1^2(nT_s)A_2(nT_s)}{4}\cos\left((2\hat{\omega}_1 - \hat{\omega}_2)nT_s + 2\phi_1(nT_s) - \phi_2(nT_s)\right) \tag{3.11}$$

$$\hat{n}_{D,Q}(n) \approx \frac{3a_1^3 A_1^2(nT_s)A_2(nT_s)}{4}\sin\left((2\hat{\omega}_1 - \hat{\omega}_2)nT_s + 2\phi_1(nT_s) - \phi_2(nT_s)\right)$$

Comparing (3.9) and (3.11), one can notice that the difference between the actual interfering terms on top of the real and imaginary parts of the desired signal, i.e. $n_{D,I}(n)$ and $n_{D,Q}(n)$, and the corresponding regenerated versions of these terms at the band-limiting filters output, i.e. $\hat{n}_{D,I}(n)$ and $\hat{n}_{D,Q}(n)$, is a scaling factor a_3/a_1^3. This coefficient then can be estimated using the adaptive algorithm presented in (3.2) and (3.3) and finally the scaled version of the $\hat{n}_{D,I}(n)$ and $\hat{n}_{D,Q}(n)$ are subtracted from the desired branch which in turn cancel out the interfering terms generated by LNA.

3.1.2 Case B: Nonlinearity in I and Q Branches of the Downconverter

The second case studies the operation of IC algorithm in presence of nonlinear elements in the I/Q branches of an I/Q downconverter. The three-signal model is again used here for demonstration purpose. The complex baseband version of the downconverted signal before the nonlinear elements reads

$$x(t) = A_0(t)e^{j(\hat{\omega}_0 t + \phi_0(t))} + A_1(t)e^{j(\hat{\omega}_1 t + \phi_1(t))} + A_2(t)e^{j(\hat{\omega}_2 t + \phi_2(t))} \tag{3.12}$$

In this example we assumed third-order polynomial characteristics with equal coefficients for both I and Q branches. Therefore, the input/output relations of the I and Q nonlinear elements are defined as follow

$$\begin{aligned} y_I(t) &= b_1 x_I(t) + b_2 x_I^2(t) + b_3 x_I^3(t) \\ y_Q(t) &= b_1 x_Q(t) + b_2 x_Q^2(t) + b_3 x_Q^3(t) \end{aligned} \tag{3.13}$$

where b_1, b_2 and b_3 are real-valued coefficients. Furthermore, and for mathematical tractability, we assume that $\hat{\omega}_1 = \frac{\hat{\omega}_0}{3}$ and $\hat{\omega}_2 = \frac{2\hat{\omega}_0}{3}$ which in turn means the second-order cross-modulation term of the blockers at $\hat{\omega}_1 + \hat{\omega}_2$ and the third-order cross-modulation term at $2\hat{\omega}_2 - \hat{\omega}_1$ interfere with the desired signal at $\hat{\omega}_0$. With the above assumptions, the signal at the I/Q

downconverter output reads

$$\begin{aligned} y(t) \approx\ & b_1 A_0(t) e^{j(\hat{\omega}_0 t + \phi_0(t))} \\ & + b_2(1-j) A_1(t) A_2(t) \cos\left((\hat{\omega}_1 + \hat{\omega}_2)t + \phi_1(t) + \phi_2(t)\right) \\ & + b_3 \frac{3A_2^2(t) A_1(t)}{4} e^{j((2\hat{\omega}_2 - \hat{\omega}_1)t + 2\phi_2(t) - \phi_1(t))} \\ & + b_1 A_1(t) e^{j(\hat{\omega}_1 t + \phi_1(t))} + b_1 A_2(t) e^{j(\hat{\omega}_2 t + \phi_2(t))} \end{aligned} \tag{3.14}$$

The discrete-time I/Q components of $y(t)$, i.e. $y_I(n)$ and $y_Q(n)$, are written as follows

$$\begin{aligned} y_I(n) =\ & b_1 A_0(nT_s) \cos\left(\hat{\omega}_0 nT_s + \phi_0(nT_s)\right) \\ & + b_2 A_1(nT_s) A_2(nT_s) \cos\left((\hat{\omega}_1 + \hat{\omega}_2)nT_s + \phi_1(nT_s) + \phi_2(nT_s)\right) \\ & + b_3 \frac{3A_2^2(nT_s) A_1(nT_s)}{4} \cos\left((2\hat{\omega}_2 - \hat{\omega}_1)nT_s + 2\phi_2(nT_s) - \phi_1(nT_s)\right) \\ & + b_1 A_1(nT_s) \cos\left(\hat{\omega}_1 nT_s + \phi_1(nT_s)\right) + b_1 A_2(nT_s) \cos\left(\hat{\omega}_2 nT_s + \phi_2(nT_s)\right) \\ y_Q(n) =\ & b_1 A_0(nT_s) \sin\left(\hat{\omega}_0 nT_s + \phi_0(nT_s)\right) \\ & - b_2 A_1(nT_s) A_2(nT_s) \cos\left((\hat{\omega}_1 + \hat{\omega}_2)nT_s + \phi_1(nT_s) + \phi_2(nT_s)\right) \\ & + b_3 \frac{3A_2^2(nT_s) A_1(nT_s)}{4} \sin\left((2\hat{\omega}_2 - \hat{\omega}_1)nT_s + 2\phi_2(nT_s) - \phi_1(nT_s)\right) \\ & + b_1 A_1(nT_s) \sin\left(\hat{\omega}_1 nT_s + \phi_1(nT_s)\right) + b_1 A_2(nT_s) \sin\left(\hat{\omega}_2 nT_s + \phi_2(nT_s)\right) \end{aligned} \tag{3.15}$$

Afterward, the signals $y_I(n)$ and $y_Q(n)$ are split into desired and reference bands. The signals in the desired and reference branches of IC, from (3.1), reads

$$\begin{aligned} y_{D,I}(n) &\approx x_{D,I}(n) + n_{D,I}(n) \\ &= b_1 A_0(nT_s) \cos\left(\hat{\omega}_0 nT_s + \phi_0(nT_s)\right) \\ &\quad + b_2 A_1(nT_s) A_2(nT_s) \cos\left((\hat{\omega}_1 + \hat{\omega}_2)nT_s + \phi_1(nT_s) + \phi_2(nT_s)\right) \\ &\quad + b_3 \frac{3A_2^2(nT_s) A_1(nT_s)}{4} \cos\left((2\hat{\omega}_2 - \hat{\omega}_1)nT_s + 2\phi_2(t) - \phi_1(nT_s)\right) \\ y_{D,Q}(n) &\approx x_{D,Q}(n) + n_{D,Q}(n) \\ &= b_1 A_0(nT_s) \sin\left(\hat{\omega}_0 nT_s + \phi_0(nT_s)\right) \\ &\quad - b_2 A_1(nT_s) A_2(nT_s) \cos\left((\hat{\omega}_1 + \hat{\omega}_2)nT_s + \phi_1(nT_s) + \phi_2(nT_s)\right) \\ &\quad + b_3 \frac{3A_2^2(nT_s) A_1(nT_s)}{4} \sin\left((2\hat{\omega}_2 - \hat{\omega}_1)nT_s + 2\phi_2(nT_s) - \phi_1(nT_s)\right) \\ y_{R,I}(n) &\approx x_{R,I}(n) + n_{R,I}(n) \approx x_{R,I}(n) \\ &= b_1 A_1(nT_s) \cos\left(\hat{\omega}_1 nT_s + \phi_1(nT_s)\right) + b_1 A_2(nT_s) \cos\left(\hat{\omega}_2 nT_s + \phi_2(nT_s)\right) \\ y_{R,Q}(n) &\approx x_{R,Q}(n) + n_{R,Q}(n) \approx x_{R,Q}(n) \\ &= b_1 A_1(nT_s) \sin\left(\hat{\omega}_1 nT_s + \phi_1(nT_s)\right) + b_1 A_2(nT_s) \sin\left(\hat{\omega}_2 nT_s + \phi_2(nT_s)\right) \end{aligned} \tag{3.16}$$

Again, similar to LNA case it is assumed that the spurious components on the reference branches are negligible comparing to the blockers. In order to regenerate the second-order interfering component on top of the desired signal the isolated blockers in $y_{R,I}(n)$ and $y_{R,Q}(n)$ are passed through simple quadratic elements. The outputs of the second-order elements, then, read

$$\begin{aligned} &y^2_{R,I}(n) = \\ &b_1^2 A_1(nT_s)A_2(nT_s)\cos\left((\hat{\omega}_1+\hat{\omega}_2)nT_s+\phi_1(nT_s)+\phi_2(nT_s)\right)+\mathrm{Re}[\Xi_2^{IM/CM}] \\ &y^2_{R,Q}(n) = \\ &b_1^2 A_1(nT_s)A_2(nT_s)\cos\left((\hat{\omega}_1+\hat{\omega}_2)nT_s+\phi_1(nT_s)+\phi_2(nT_s)\right)+\mathrm{Im}[\Xi_2^{IM/CM}] \end{aligned} \tag{3.17}$$

where all the complex second-order inter/cross-modulation terms outside the desired band, i.e. around $\hat{\omega}_0$, are denoted by $\Xi_2^{IM/CM}$. The output of the band-limiting filters for the quadratic elements in I and Q branches, i.e. $\hat{n}^{(2)}_{D,I}(n)$ and $\hat{n}^{(2)}_{D,Q}(n)$ from Fig. 3.2, reads

$$\begin{aligned} \hat{n}^{(2)}_{D,I}(n) &= b_1^2 A_1(nT_s)A_2(nT_s)\cos\left((\hat{\omega}_1+\hat{\omega}_2)nT_s+\phi_1(nT_s)+\phi_2(nT_s)\right) \\ \hat{n}^{(2)}_{D,Q}(n) &= b_1^2 A_1(nT_s)A_2(nT_s)\cos\left((\hat{\omega}_1+\hat{\omega}_2)nT_s+\phi_1(nT_s)+\phi_2(nT_s)\right) \end{aligned} \tag{3.18}$$

It is clear then that the second-order interference in the desired branch of the IC algorithm in (3.16) is the scaled version of the regenerated interference which is presented in (3.18). Thus, proper scaling of the $\hat{n}^{(2)}_{D,I}(n)$ and $\hat{n}^{(2)}_{D,Q}(n)$ using the mentioned adaptive algorithm and subtracting the result eliminates the second-order interference from the desired signal band.

To suppress the third-order interference separate paths with cubic elements are employed in the IC algorithm reference paths. The cubic term outputs, in turn, are written as

$$\begin{aligned} &y^3_{R,I}(n) = \\ &\frac{3b_1^3 A_2^2(nT_s)A_1(nT_s)}{4}\cos\left((2\hat{\omega}_2-\hat{\omega}_1)nT_s+2\phi_2(nT_s)-\phi_1(nT_s)\right)+\mathrm{Re}[\Xi_3^{IM/CM}] \\ &y^3_{R,Q}(n) = \\ &\frac{3b_1^3 A_2^2(nT_s)A_1(nT_s)}{4}\sin\left((2\hat{\omega}_2-\hat{\omega}_1)nT_s+2\phi_2(nT_s)-\phi_1(nT_s)\right)+\mathrm{Im}[\Xi_3^{IM/CM}] \end{aligned} \tag{3.19}$$

The outputs of the band limiting filters in I and Q branches, $\hat{n}^{(3)}_{D,I}(n)$ and

$\hat{n}^{(3)}_{D,Q}(n)$ from Fig. 3.2, read

$$\hat{n}^{(3)}_{D,I}(n) = \frac{3b_1^3 A_2^2(nT_s)A_1(nT_s)}{4}\cos\left((2\hat{\omega}_2 - \hat{\omega}_1)nT_s + 2\phi_2(nT_s) - \phi_1(nT_s)\right) \tag{3.20}$$

$$\hat{n}^{(3)}_{D,Q}(n) = \frac{3b_1^3 A_2^2(nT_s)A_1(nT_s)}{4}\sin\left((2\hat{\omega}_2 - \hat{\omega}_1)nT_s + 2\phi_2(nT_s) - \phi_1(nT_s)\right)$$

Here, similar to second-order case, the third-order interfering terms are regenerated up to a scaling factor. The scaling factor is estimated using the LMS adaptive algorithm mentioned above and the final scaled version of the regenerated interfering terms are subtracted from the desired signal branches of the IC algorithm in both I and Q branches.

In the above examples two following assumptions are used for the operation of IC algorithm

- $\mathbb{E}[|n_R(n)|^2] \ll \mathbb{E}[|x_R(n)|^2]$ which means the power of the blockers are significantly higher than all the inter/cross-modulations that fall in the reference branches of IC algorithm.
- $n_D(n)$ is dominated by inter/cross-modulations of the blockers.

Hereafter, we justify the validity of these two assumptions in practical receivers again invoking on the three-signal model and I/Q nonlinearity case. Needless to say that the same arguments can be extended for the nonlinear LNA case. According to two-blocker scenario the spurious frequencies generated by *third-order* nonlinearity that can hit the *reference band* are as follows (Table A.4 in the Appendix)

Self-distortion components (e.g. $\frac{b_3(1+g_3)}{2}(\frac{3A_1^3(t)}{4} + \frac{3A_2^2(t)A_1(t)}{2} + \frac{3A_0^2(t)A_1(t)}{2})e^{j(\hat{\omega}_1 t+\phi_1(t))}$) These components hit the blockers frequencies. However, as the nonlinear component is assumed to be mild, i.e. $b_3 \ll b_1$, then these interfering components are orders of magnitude weaker than the blockers themselves and can be neglected.

Cross-modulations of two blockers (e.g. $\frac{b_3(1+g_3)}{2}(\frac{3A_1^2(t)A_2(t)}{4}e^{j((2\hat{\omega}_1-\hat{\omega}_2)t+2\phi_1(t)-\phi_2(t))})$) Again with the mild linearity assumption in mind, these components can be ignored as they are significantly weaker comparing to the power of the original blockers.

Cross-modulations of the desired signal and one blocker (e.g. $\frac{b_3(1+g_3)}{2}\frac{3A_1^2(t)A_0(t)}{4}e^{j((2\hat{\omega}_1-\hat{\omega}_0)t+2\phi_1(t)-\phi_0(t))}$) The envelopes of these components are proportional to the desired signal envelope and as the desired signal is significantly weaker than the blockers these components are insignificant.

Cross-modulations of the desired signal and *both* blockers (e.g $\frac{b_3(1+g_3)}{2}\frac{6A_0(t)A_1(t)A_2(t)}{4}e^{(j(\hat{\omega}_1-\hat{\omega}_2+\hat{\omega}_0)t+\phi_1(t)-\phi_2(t)+\phi_0(t))}$) The envelopes of these components are also proportional to the desired signal envelope and as the desired signal is significantly weaker than the blockers these components are insignificant.

As for the *second-order* nonlinearity the terms that can hit the reference band are listed below (Table A.4 in the Appendix)

IMD term from interaction of the desired signal and one blocker (e.g. $b_2(1+jg_2)A_1(t)A_0(t)\cos((\hat{\omega}_1-\hat{\omega}_0)t+\phi_1(t)-\phi_0(t))$) The nonlinear component assumed to be mild $b_2 \ll b_1$. Moreover, the envelopes of these components are proportional to the weak desired signal envelope. All in all, these components can be ignored in comparison to strong blockers in reference band.

IMD term from interaction of the two blockers (e.g. $b_2(1-jg_2)A_1(t)A_2(t)\cos((\hat{\omega}_1+\hat{\omega}_2)t+\phi_1(t)+\phi_2(t))$) Again, these components can be ignored with the mild nonlinearity assumption $b_2 \ll b_1$.

Following the above discussion, it is possible to conclude that in practical implementations the assumption $\mathbb{E}[|n_R(n)|^2] \ll \mathbb{E}[|x_R(n)|^2]$ is valid. Nevertheless, with the mild nonlinearity and weak desired signal assumption the results of above examples can be extended to the higher order nonlinearity and larger number of blockers. To examine the second assumption, i.e. $n_D(n)$ should be only generated by the blockers captured in the reference branch, we again refer to the example which is presented in the Appendix Section A.2. A closer look at the derivations for second- and third-order spurious frequencies (Tables A.4 and A.3 in the Appendix) shows that all the components interfering with desired band can be ignored comparing to the blockers second- and third-order cross-modulations, considering the weak desired signal and mild nonlinearity assumptions. This, in turn, means the dominant interference on top of the desired signal band is generated by the blockers which are captured in the reference band.

3.2 Computer Simulation and Laboratory Measurement Examples

To illustrate the basic idea of the proposed compensation principle, purely computer simulation based results are presented here first. In this experiment, the desired signal is QPSK modulated signal located at f_0 =103 MHz RF carrier with roughly 1-MHz RF bandwidth. The blocker in this case is an amplitude modulated (AM) at f_1 =98.95 MHz RF center frequency with 100

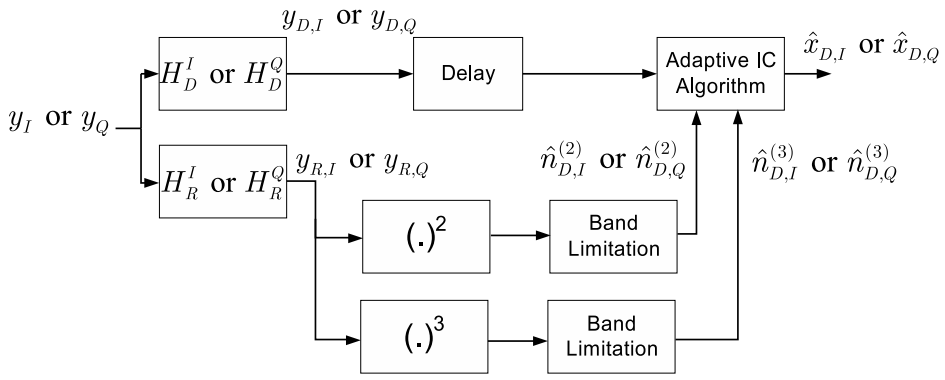

Figure 3.2: Detailed representation of the IC algorithm designed for compensation of second- and third-order cross-modulation interfering terms.

kHz modulating tone and 20% modulation index and the power difference between the blocker and the desired signal is set to 40 dB. The LO frequency in this experiment is set to 100 MHz and third-order nonlinearity is implemented in the I/Q downconversion process. After the downconversion the desired signal and the blocker are located at $\hat{f}_0$ =3 MHz and $\hat{f}_1 = -1.05$ MHz. Moreover, as the result of third-order nonlinearity process the AM blocker generates harmonics at 2.85, 3.15 and 3.45 MHz and intermodulation terms at 2.95, 3.05, 3.25 and 3.35 MHz which all fall on top of the desired signal at IF. The obtained results are illustrated in Fig. 3.3, in terms of the downconverted complex signal spectrum as well as demodulated desired signal at symbol rate without and with digital compensation. The adaptation of the IC coefficients are implemented using the LMS algorithm which is described in previous section. Without compensation, the demodulated desired signal is useless as such. However, by using the proposed compensator, virtually all the essential interference can be suppressed, resulting in close-to perfect QPSK signal constellations as can be seen in Fig. 3.3.

Next results obtained using actual laboratory signal measurements are reported. For illustration, exactly the same RF waveform setups as in Subsection 2.3.1 is used. The desired signal is QPSK modulated with 800 kHz symbol rate and located at 103 MHz RF carrier. The pulse-shape is a raised-cosine pulse with 30% roll-off, yielding roughly 1 MHz RF bandwidth. Notice that "down-scaled" RF frequencies in the order of 100 MHz are used simply to facilitate the measurement system implementation (cabling requirements, etc.) and do not play any other role here. I/Q downconversion with 100 MHz LO signal(s) translates the desired signal to 3 MHz IF. The strong blocker in this experiment is a sinusoidal at 98.6 MHz RF frequency. This results in second-order harmonic distortion component on top of the desired signal at 2.8 MHz (after I/Q downconversion). After I/Q downconverting the signals

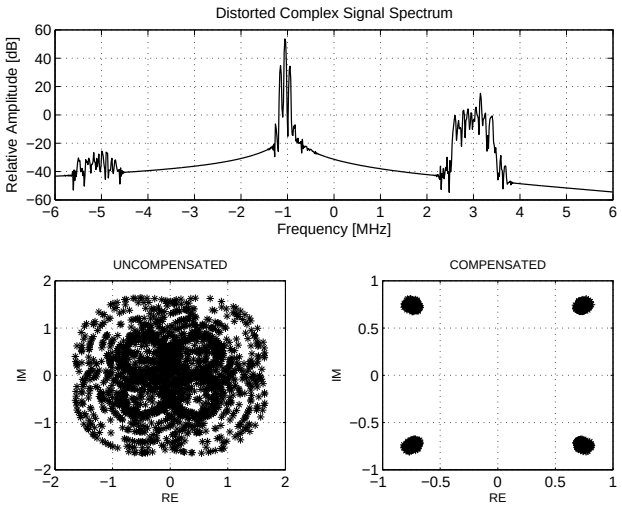

Figure 3.3: Top: Simulated spectrum of the downconverted complex signal with third-order distortion. The desired signal is QPSK modulated and located at +3 MHz IF. Bottom: Baseband desired signal observations at symbol rate without and with compensation.

down to IF, the I and Q signals are lowpass filtered, sampled and digitized. In the basic experiments, the power difference of the strong blocking signal and the desired one is set to 40 dB to model a typical yet challenging example case. Moreover, the sampling frequency in the I and Q branches is here 32 MHz, the resolution of the used ADC's is 14 bits and the available sample memory per captured I/Q data block is 265K samples. Fig. 3.4 shows the measured IF signal spectrum with sinusoidal blocking signal, evidencing again clear second-order harmonic distortion on top of the desired signal. In this case when processing measured signals, one sample memory (two consecutive samples) is incorporated also in the digital compensation stage to account for the possible (yet unknown) memory effects of the measured receiver analog front-end. Fig. 3.5 shows example realizations of the adaptive filter coefficients during the compensator adaptation, evidencing clean convergence in roughly 20,000 iterations or so with the selected step-size values. In general, the selection of the step-size affects both the convergence rate and the average steady-state performance. Notice that if sufficient computational resources are available, re-iteration over the same received data block can also be used in practice. Furthermore, once the convergence is established, it is likely sufficient to update the coefficients only rather rarely, in order to keep track of the possible effects of changing nonlinear characteristics.

In order to obtain further insight into the operation of the proposed compensator, especially when considerable additive noise is present in the signals, a new set of measurements are carried out. For illustration purposes,

the focus is on the previous second-order interference case, with considerable amount of additive white (over the whole measurement band-width) noise being included in the measurements. The in-band SNR ranges roughly from 0 to 10 dB. The noisy signals are then processed using the compensator and both the uncompensated and compensated signals are detected, in a symbol-by-symbol manner, and the corresponding detection error rates are evaluated. In this case, the original RF power of the interfering carrier is slightly decreased, compared to earlier experiments, such that the in-band carrier-to-interference ratio is roughly 6 dB without compensation. Otherwise, with the earlier setup, the error rate of the uncompensated signal would have been almost constant, independently of the actual additive noise level.

The obtained results are shown in Fig. 3.6. For reference we also evaluate the error rate performance with the blocking signal turned off, in order to get proper reference against which to compare the error rates of the uncompensated and compensated signals. Here, as also earlier when experimenting and illustrating the symbol rate signals, all the synchronization (symbol timing recovery, carrier phase and frequency offset estimation and compensation) information is obtained by digitally processing the observed signal. Thus there will also be some residual error and distortion in the signal entering the data detection due to finite accuracy of the used synchronization techniques. This explains the gap of 0.7-0.8 dB between the measured reference and theoretical reference curves in Fig. 3.6. However, the most important message is that the detection error rate of the compensated system is practically identical to that of the measured reference. The difference at raw (uncoded) error rates in the order of 10^{-2} to 10^{-3} is only around 0.2-0.25 dB. This gives further confidence on the proposed compensation technique, in the sense that reliable operation is demonstrated under very low SNR's. This is crucial in any practical system, and especially in CDMA type systems where the typical chip-level SNR's indeed range around 0 dB.

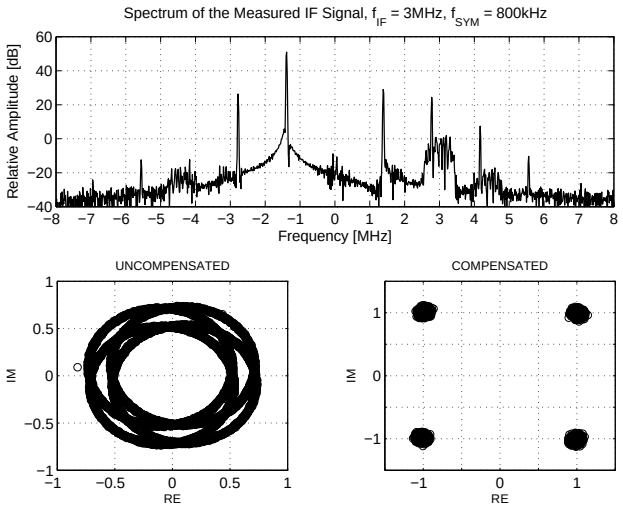

Figure 3.4: Upper part: Measured IF signal spectrum with sinusoidal blocker. The desired signal is QPSK modulated and located at +3 MHz IF. Lower part: Baseband desired signal observations at symbol rate without and with compensation.

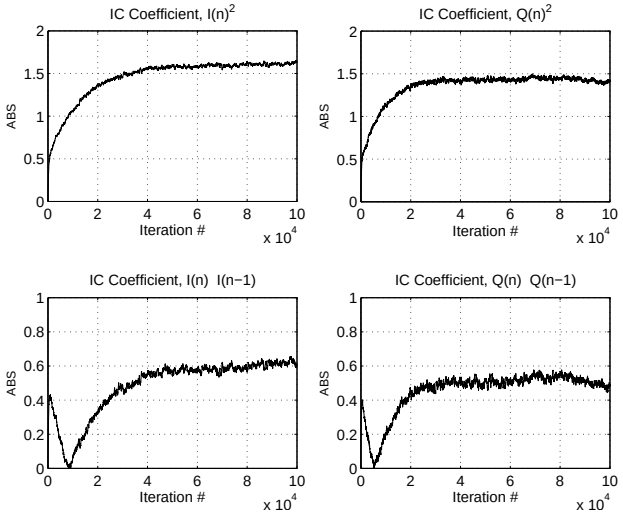

Figure 3.5: Example realization of the adaptive IC coefficients. Quadratic elements coefficients for I/Q branches of IC algorithm (top row) and memory elements coefficients for I/Q branches of IC algorithm (bottom row).

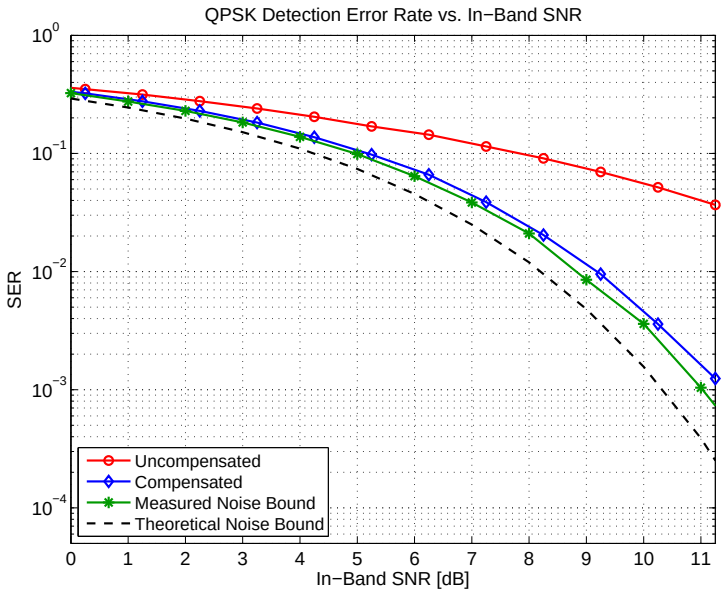

Figure 3.6: Symbol error rate (SER) performance with measured signals as a function of additive noise level. QPSK modulated desired signal and sinusoidal blocker. The in-band carrier-to-interference (C/I) ratio is around 6 dB without compensation.

CHAPTER 4

DIGITAL MITIGATION OF DYNAMIC OFFSET IN DIVERSITY RECEIVERS

4.1 Modeling Dynamic Offset in Diversity Receiver

The mechanism resulting in dynamic DC-offset interference in DCR is already explained in Subsection 2.3.3. For convenience, we repeat the expression for the downconverted desired signal including the dynamic DC-offset effect in the following

$$x_{iq}(t) = \zeta_u x_u(t) + |\zeta_b|^2 (l_I + j l_Q) |x_b(t)|^2 + x_\gamma(t) \tag{4.1}$$

In order to construct a more realistic model, the effects of additive white Gaussian noise (AWGN) as well as the desired signal and blocker channel gains are also included in (4.1) where $x_\gamma(t)$ is a zero-mean white Gaussian noise. Also the relative complex channel gains of the desired signal and the blocker at ω_u and ω_b are represented by ζ_u and ζ_b, respectively. Hereafter, a novel method for mitigation of dynamic DC-offset interference in two-antenna diversity receiver systems is addressed. The proposed method is motivated by high cost and rigidness of traditional approaches (see Subsection 2.3.3) in dealing with dynamic DC-offset interference in the context of modern multi-antenna SDR/CR receivers. The choice of two receiver paths, without loss of generality, is to keep the discussion practically oriented and applicable in mobile devices, where the two-antenna receiver case is indeed feasible.

Overall signal model for the two-receiver case under RF self-mixing can essentially be written from (4.1) as

$$\begin{bmatrix} x_{iq,1}(t) \\ x_{iq,2}(t) \end{bmatrix} = \begin{bmatrix} \zeta_{u,1} & |\zeta_{b,1}|^2 (l_{I,1} + jl_{Q,1}) \\ \zeta_{u,2} & |\zeta_{b,2}|^2 (l_{I,2} + jl_{Q,2}) \end{bmatrix} \begin{bmatrix} x_u(t) \\ |x_b(t)|^2 \end{bmatrix} + \begin{bmatrix} x_{\gamma,1}(t) \\ x_{\gamma,2}(t) \end{bmatrix} \quad (4.2)$$

where the subscripts 1 and 2 refer to the two antennas. The above equation is written in a more compact form using matrix notation in the following as

$$\mathbf{x}_{iq}(t) = \mathbf{Z} \begin{bmatrix} x_u(t) \\ |x_b(t)|^2 \end{bmatrix} + \mathbf{x}_\gamma(t) \quad (4.3)$$

where $\mathbf{Z}$ is the channel plus leakage coefficients mixing matrix. The columns of $\mathbf{Z}$ are in effect channels for the desired signal and the dynamic DC component, $\mathbf{Z} = [\mathbf{z}_u \ \mathbf{z}_b]$. There, effective system basis vectors are $\mathbf{z}_u = [\zeta_{u,1} \ \zeta_{u,2}]^T$ and $\mathbf{z}_b = [|\zeta_{b,1}|^2(l_{I,1} + jl_{Q,1}) \ |\zeta_{b,2}|^2(l_{I,2} + jl_{Q,2})]^T$. As in the single-antenna case, it is also clear from (4.2) and (4.3) that the signal-to-interference-plus-noise ratio (SINR) of the baseband observations are strongly affected by the offset interference relative to $|x_b(t)|^2$. Fortunately, there are linear diversity methods available to improve the SINR by mitigating interference and/or additive noise by linearly combining the downconverted signals from the two front-ends. In continuation we briefly describe number of these methods, first at general level and then more specifically applied to offset suppression task.

4.2 Spatial Processing Methods

Let's assume a general case of a receiver with M antennas and front-ends in which the observed signals $x_1(t), ..., x_M(t)$ are linear combinations of $N \leq M$ mutually independent source signals $u_1(t), ..., u_N(t)$. The relation between the signal sources and observed signals using matrix notations reads

$$\mathbf{x}(t) = \mathbf{H}_u \begin{bmatrix} u_1(t) \\ \vdots \\ u_N(t) \end{bmatrix} + \mathbf{x}_\gamma(t) \quad (4.4)$$

where $\mathbf{x}(t) = [x_1(t), x_2(t), ..., x_M(t)]^T$ is the vector of the observed signals, $\mathbf{H}_u = [\mathbf{h}_{u,1}, \mathbf{h}_{u,2}, ..., \mathbf{h}_{u,N}]$ is the *mixing matrix* with $\mathbf{h}_{u,i} = [h_{u,i}^{(1)}, h_{u,i}^{(2)}, ..., h_{u,i}^{(M)}]^T$ where $h_{u,i}^{(k)}$ is complex-valued coefficient of the i^{th} independent source in the k^{th} observed signal, i.e., $x_k(t)$. Moreover, $\mathbf{x}_\gamma(t) = [x_{\gamma,1}(t), x_{\gamma,2}(t), ..., x_{\gamma,M}(t)]^T$ is the vector of zero-mean Gaussian noise in which $\mathbb{E}[|x_{\gamma,i}(t)|^2] = \sigma^2$ for $\forall i$. Here we define a interference suppression matrix $\mathbf{W}_D = [\mathbf{w}_{D,1}, \mathbf{w}_{D,2}, ..., \mathbf{w}_{D,N}]$ with $\mathbf{w}_{D,i} = [w_{D,i}^{(1)}, w_{D,i}^{(2)}, ..., w_{D,i}^{(M)}]^T$ where $w_{D,i}^{(k)}$ are complex-valued coefficients.

The improvement in S(I)NR is achieved by multiplying the observed signal vector $\mathbf{x}(t)$ by $\mathbf{W}_D^H$ which yields

$$\mathbf{y}(t) = \mathbf{W}_D^H \mathbf{x}(t) \tag{4.5}$$

The vector at the output of the interference suppression matrix is $\mathbf{y}(t) = [y_1(t), y_2(t), ..., y_N(t)]^T$. The matrix $\mathbf{W}_D^H$ can be selected to invert the effect of the mixing matrix, $\mathbf{H}_u$, which means $\mathbf{W}_D^H = (\mathbf{H}_u^H \mathbf{H}_u)^{-1} \mathbf{H}_u^H$ given matrix $\mathbf{H}_u$ is a full-rank matrix here. In literature this method is referred to as *zero forcing* (ZF) [36,65]. The ZF method aims at removing the interference from the desired signal however it neglects the noise component. Therefore, ZF method can result in amplification of the independent noise element or *noise enhancement* [36,65]. Another widely used linear spatial processing method is motivated by match filter (MF) and is called maximum ratio combining (MRC) [66] also known in literature as matrix match filter (MMF) [36]. The received signal vector in MRC is transformed using Hermitian of the mixing matrix i.e. $\mathbf{W}_D^H = \mathbf{H}_u^H$. Therefore, the linearly transformed vector $\mathbf{y}(t)$ reads,

$$\begin{aligned} \mathbf{y}(t) &= \mathbf{W}_D^H \mathbf{H}_u \begin{bmatrix} u_1(t) \\ \vdots \\ u_N(t) \end{bmatrix} + \mathbf{W}_D^H \mathbf{x}_\gamma(t) \\ &= \mathbf{H}_u^H \mathbf{H}_u \begin{bmatrix} u_1(t) \\ \vdots \\ u_N(t) \end{bmatrix} + \mathbf{H}_u^H \mathbf{x}_\gamma(t) \end{aligned} \tag{4.6}$$

Now MRC provides diversity for individual source signals against channel fading but it does not take the intermixing of the signals into account. In effect, only if $\mathbf{H}_u$ is orthogonal matrix, meaning that $\mathbf{H}_u^H \mathbf{H}_u$ is a diagonal matrix, then the MRC also separates the source signals. In the general case with non-orthogonal $\mathbf{H}_u$, MRC is thus clearly suboptimal [66].

Another method which provides a compromise between MRC and ZF when both noise and interference are present is called SINR maximizing generalized Eigen-filter (M-GEF) [33, 54, 55]. This linear transform is the natural reference in all performance evaluations as it yields the best SINR among the linear transforms [54]. The transform for the source signal $u_i(t)$ is formally given by

$$y_i(t) = \mathbf{w}_{D,i}^H \mathbf{x}(t) \tag{4.7}$$

and the solution $\mathbf{w}_{D,i}$ maximizing the SINR with $u_i(t)$ as the desired signal in $y_i(t)$ can be written as [33, 54]

$$\mathbf{w}_{D,i}^{opt} = \arg\max_{\mathbf{w}_{D,i}} \{ \frac{\mathbf{w}_{D,i}^H \mathbf{R}_u \mathbf{w}_{D,i}}{\mathbf{w}_{D,i}^H (\mathbf{R}'_u + \sigma^2 \mathbf{I}) \mathbf{w}_{D,i}} \} \tag{4.8}$$

in which

$$\mathbf{R}_u = \mathbb{E}[\mathbf{h}_{u,i}\mathbf{h}_{u,i}^H]$$
$$\mathbf{R}'_u = \sum_{j=1,j\neq i}^{N} \mathbb{E}[\mathbf{h}_{u,j}\mathbf{h}_{u,j}^H] \tag{4.9}$$

In practice, $\mathbf{w}_{D,i}$ can be calculated using the generalized Eigen-value filtering approach [33,34,54], i.e. $\mathbf{w}_{D,i}$ is equal to the Eigen-vector of the matrix $(\mathbf{R}'_u + \sigma^2\mathbf{I})^{-1}\mathbf{R}_u$ corresponding to its largest Eigen-value. The largest Eigenvalue itself is the maximum SINR achievable by any linear filter [33, 34, 54].

One important note on the discussed spatial processing methods so far is that implementing any of the described methods requires the knowledge of the mixing matrix and the noise variance in the receiver side. In most practical cases these values are not readily available for the receiver and needs to be estimated by transmitting extra symbols as training sequences. Therefore, devising a blind method to yield maximum SINR without the knowledge of the mixing matrix and noise power levels, although computationally more demanding, eliminates the need for transmission of these extra symbols. In this context one blind method that provides powerful tools and algorithms is independent component analysis (ICA) [67,68]. In the following section first we argue that the dynamic DC-offset issue in two-front-end receiver context, as it is formulated in (4.2), should be viewed as the special case of (4.4) and therefore implementing the spatial processing methods presented above mitigate the dynamic DC-offset component to various extends. Thereafter, the application of ICA-based algorithms in this context, which is published in [P3], is introduced and finally, the performance of widely-implemented ICA-based algorithm against the mentioned spatial processing methods are demonstrated through the results which are obtained from computer simulation experiments [P3].

4.2.1 Dynamic Offset Suppression Using ICA

In its basic form, ICA can recover multiple statistically independent source signals, up to scale and permutation by just observing linear mixtures of them [67, 68] similar to the one presented in (4.4). Although, the complete separation of the interfering sources and desired signal in a noisy environment is not theoretically possible [33,55], Nevertheless, the SINR provided by ICA, as such, is extremely close to the maximum achievable SINR by any linear method [33]. Thus in the context of diversity receivers, ICA can be considered as a practical method of joint interference rejection and diversity combining.

The model (4.3) fits to the general instantaneous mixing model which is required by ICA, i.e. two formal statistically independent source signals $x_u(t)$ and $|x_b(t)|^2$ are linearly mixed and two (or more) separate observation from

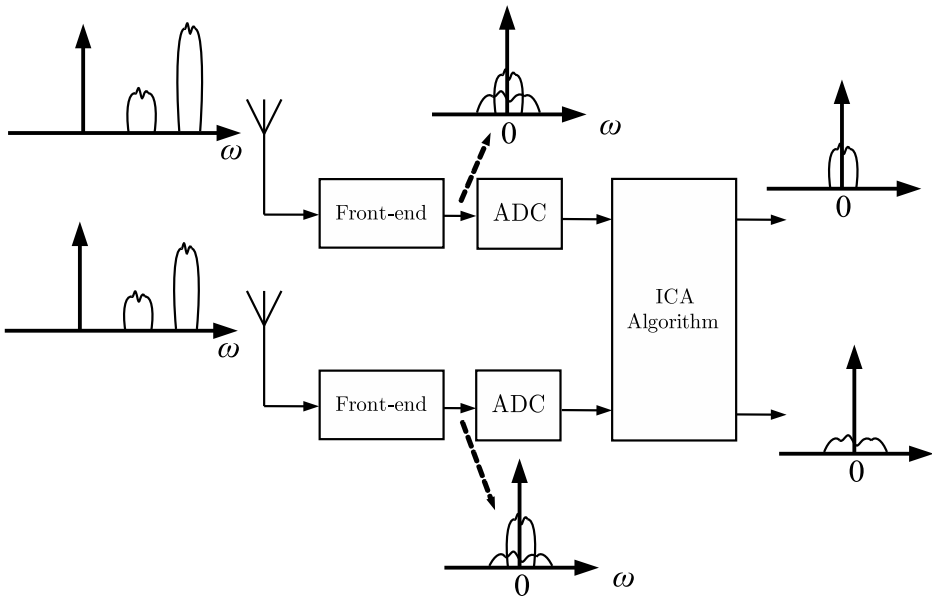

Figure 4.1: A conceptual presentation of a receiver with two front-ends implementing ICA algorithm to mitigate the dynamic DC-offset.

their mixtures are available to the receiver. Furthermore, assuming different channels and/or different leakage coefficients for the different receivers, the models in (4.2) and (4.3) are always identifiable. The operation principle of the ICA algorithm in mitigating dynamic DC-offset in two-front-end receiver is depicted in Fig. 4.1. The ICA algorithm in dynamic DC-offset mitigation application maximizes the SINR both for desired signal and for the offset component at its output ports. However, in this particular application the desired signal is the output we are interested in and the DC-offset is discarded. To assess the obtainable offset interference rejection capability of the ICA-based approach, a series of computer simulation results is provided here. A similar two-receiver case as in the previous section is assumed. In the first simulation case the desired signal and the blocker modulations are QPSK and for the second simulation case the modulations for both desired signal and blocker are 16QAM. In the simulation setup, channel coefficients $\zeta_{u,1}$, $\zeta_{u,2}$, $\zeta_{b,1}$ and $\zeta_{b,2}$ are drawn randomly from the complex Gaussian distribution with zero mean and variance of one. The additive noise sequences ($x_{\gamma,1}(t)$ and $x_{\gamma,2}(t)$) are white Gaussian noise with given power levels defined in the Table 4.1, depending on the desired signal modulation type. Each experiment consists of receiving the two receivers' signals for 50,000 symbol intervals, over which the ICA is then applied for mitigating the offset interference. The practical ICA algorithm used here is the equivariant adaptive source identification (EASI) algorithm [68]. In this algorithm the interference suppression matrix, $\mathbf{W}_{EASI}^{H}$, is iteratively updated according to the following

rule

$$\mathbf{W}_{EASI}^{H}(t+1) = \mathbf{W}_{EASI}^{H}(t) - \mu_{EASI}\mathbf{M}(\mathbf{t})\mathbf{y}(\mathbf{t})\mathbf{W}_{EASI}^{H}(t) \tag{4.10}$$

in which μ_{EASI} is a scalar step size and the update matrix $\mathbf{M}(\mathbf{t})$ is defined as

$$\mathbf{M}(\mathbf{t}) = \mathbf{y}(t)\mathbf{y}^{H}(t) - \mathbf{I} + \mathfrak{f}[\mathbf{y}(t)]\mathbf{y}^{H}(t) - \mathbf{y}(\mathbf{t})\mathfrak{f}[\mathbf{y}(t)]^{H} \tag{4.11}$$

Here $\mathbf{y}(t) = \mathbf{W}_{EASI}^{H}(t)\mathbf{x}_{iq}(t)$, $\mathbf{I}$ denotes identity matrix and $\mathfrak{f}[.]$ is an arbitrary nonlinear function. In these experiments $\mathfrak{f}[.]$ is a simple third-order nonlinearity and adaptation step-size corresponding to convergence in the stated block length of 50,000 symbol intervals. The average output SINR is calculated for comparing the performance of the ICA-based processing against M-GEF reference (forming a theoretical bound for any linear interference cancellation method). In addition, assuming known channel state, also ZF and MRC are also implemented for comparison, in which only either the interference (ZF) or additive noise (MRC) is conceptually taken into account. The average SINR performances are obtained by averaging over 1000 different realization of channel coefficients. The RF-LO leakage coefficients are in the order of -50 dB to -60 dB, which represent state-of-the-art.

The simulation parameters are summarized in Table 4.1. The obtained output SINR results as a function of the in-band signal-to-interference ratio (SIR) before compensation, for the case 1 and 2 are presented in Fig. 4.2 and fig. 4.3, respectively. The interference free curve shows the average output SINR in case that the dynamic offset interference could be avoided totally in RF front-end. In the first set of experiments (case 1), QPSK waveforms are utilized and the additive noise SNR at the receiver input is 5dB per receiver. Without any other interference and ideal MRC, the output S(I)NR would be 5+3 = 8dB. As shown in Fig. 4.2, the overall output SINR of the ICA method as a function of the RF blocker power is somewhere between 8dB and 5dB. In the most challenging case of −30dB input SIR, the offset interference is totally masking the desired signal, before compensation. At the compensator output, the SINR is still around +5dB as shown in the figure. In the other set of experiments (case 2), 16QAM waveforms are assumed and thus the additive noise SNR is also higher, being here 10dB per receiver at the input. With 3dB MRC gain, without any interference, 13dB S(I)NR would then be obtained. Again varying the blocker power resulting in in-band SIR's in the order of −30dB to 20dB, the output SINR after ICA processing is from 13dB to 9dB. Thus again it can be concluded that most offset interference is effectively mitigated.

4.2.2 RF Dimensioning Example

We address, here, the question how much the ICA-based mitigation can relax certain RF constraints in the receiver design. Again we consider a diversity

Table 4.1: Simulation parameters used for experiments.

	Case 1	Case 2
Desired Signal	QPSK (0 dBm)	16QAM (0 dBm)
Blocker	QPSK [10 to 48 dBm]	16QAM [10 to 48 dBm]
RF-LO Leakage	[-54 to -56 dB]	[-54 to -56 dB]
In-band SNR	5 dB	10 dB

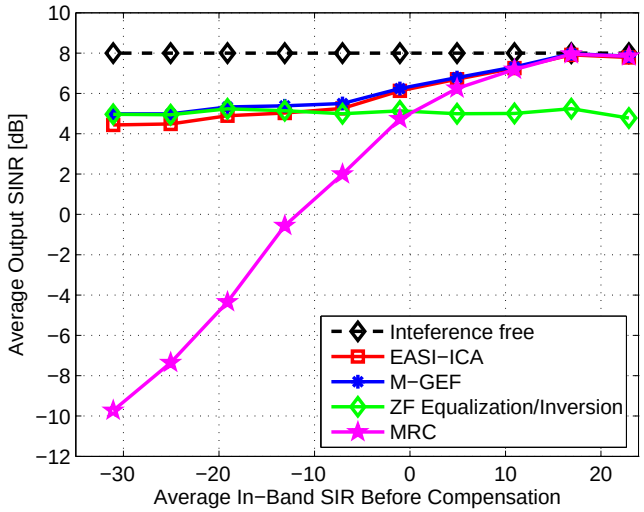

Figure 4.2: Case 1: The desired signal and the blocker are both QPSK and the in-band SNR for desired signal is 5dB. Averaging is performed over 1000 realizations of the channel coefficients.

receiver with two antennas, and for target SINR definitions, QPSK desired signal waveform is assumed. The target is to yield a minimum of 5dB in-band SINR at compensator output (detector input) corresponding to a raw detection error rate in the order of $10^{-1} \ldots 10^{-2}$.In the front-end design, the RF LNA gain $G_{LNA} = 20$dB the RF-LO leakage coefficients are assumed to be -60dB. Then the maximum permitted power of the blocker $x_b(t)$ is calculated for both ICA-based mitigation method and ordinary MRC when the output SINR of both methods is equal to the mentioned 5dB. The desired signal power level at mixer input is given by

$$p_{x_u(t)} = -99 + G_{LNA} - 3 = -82 \quad [\text{dBm}] \tag{4.12}$$

Here, it is assumed that the desired signal level at the antenna input is at a nominal sensitivity level of -99dBm and 3dB loss due to splitting the signal into the I and Q paths are considered in the above equation. Now, Fig. 4.2 shows that to achieve the output SINR of 5dB, the respective values of

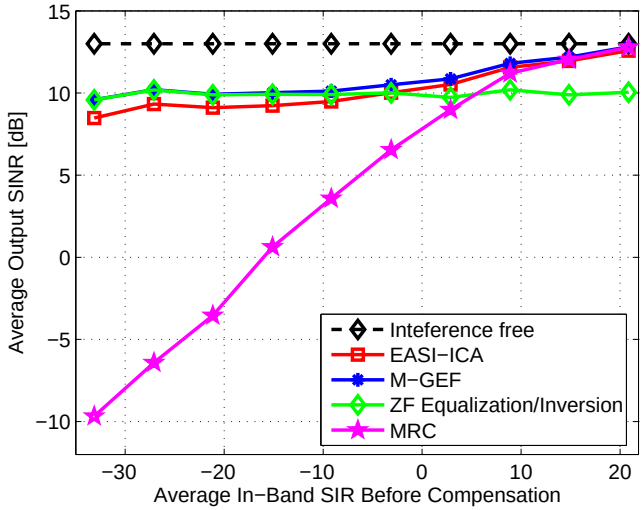

Figure 4.3: Case 2: The desired signal and the blocker are both 16QAM and the in-band SNR for desired signal is 10dB. Averaging is performed over 1000 realizations of the channel coefficients.

minimum needed input SIR for ICA-based method and MRC are around -30dB and 0dB. From (4.12) and these input SIR values, the maximum allowable power of the dynamic offset interference for ICA- and MRC-based receivers can be calculated as

$$\begin{aligned} p_{|x_b(t)|^2(\text{ICA})} &= -82 + 30 = -52 \quad [\text{dBm}] \\ p_{|x_b(t)|^2(\text{MRC})} &= -82 + 0 = -82 \quad [\text{dBm}] \end{aligned} \tag{4.13}$$

then the relation between the power of the blocking signal $x_b(t)$ at RF LNA input and the power of the dynamic offset component at baseband is of the form

$$p_{x_b(t)} = \frac{p_{|x_b(t)|^2} - L}{2} - G_{LNA} + 3 \tag{4.14}$$

where $L = 20\log_{10}(l_I) = 20\log_{10}(l_Q) = -60$ dB. Therefore, the maximum tolerable RF power of blocking signal at the RF LNA input in case of ICA-based receiver and MRC method from (4.13) and (4.14) reads

$$\begin{aligned} p_{x_b(t)(\text{ICA})} &= \frac{-52 + 60}{2} - 20 + 3 = -13 \quad [\text{dBm}] \\ p_{x_b(t)(\text{MRC})} &= \frac{-82 + 60}{2} - 20 + 3 = -28 \quad [\text{dBm}] \end{aligned}$$

The above calculation shows that by implementing the ICA-based method for mitigating the dynamic offset it is possible to relax the attenuation constrains of the RF bandpass filter up to 15dB when compared to ordinary

MRC processing. In addition, as it is mentioned earlier in this chapter using the ICA-based method the overall receiver DSP functionalities are simplified compared to MRC-based receiver in the sense that no channel estimation is needed in the ICA-based receiver.

CHAPTER 5

NONLINEARITY MODELING AND LINEARIZATION TECHNIQUES IN RADIO TRANSMITTERS

Communication waveforms with a highly time-variant envelope, like orthogonal frequency division multiplexing (OFDM) [38], are widely deployed in spectrally efficient digital data transmission links. However, these waveforms, due to their high peak-to-average power ratio (PAPR), impose stringent requirements on the linearity of the components in transmitter and receiver chains, most notably on the power amplifier (PA). A nonlinear PA can compromise the information integrity of the signals with high PAPR and generate excessive interference in neighboring channels. Thus, to facilitate efficient utilization of the available frequency band without interfering with neighboring channels, a sufficiently linear PA should be deployed in the transmitter. Unfortunately, the linearity and the power efficiency in PAs are contradictory design constrains [18, 39, 40, 69].

One prominent solution to the linearity versus power efficiency dilemma is the utilization of linearizers [69–72], i.e., to implement an efficient nonlinear PA in the transmitter but compensate for the nonlinearity effects using additional circuitry and/or sophisticated signal processing algorithms. This chapter includes some essential basics on nonlinear PAs and linearization techniques particularly aimed at motivating the reader for the presentation of the main contributions of this manuscript on feedforward linearization technique which is discussed in more detail in Chapters 6 and 7.

5.1 Characterizing Input/Output Relation in RF PA

5.1.1 Bussgang Theory

Given a zero-mean Gaussian distributed signal $x(t)$ is the input of an instantaneous nonlinearity and $y(t)$ is the corresponding output, then according to the Bussgang theorem [73]

$$\mathbb{E}[y(t)x^*(t)] = \alpha_G \times \mathbb{E}[x(t)x^*(t)] \tag{5.1}$$

One of the results of this theorem is that the output of an instantaneous nonlinearity with a zero-mean Gaussian distributed input is a scaled version of the input signal plus an IMD term $d(t)$ that is uncorrelated with the input signal i.e.,

$$y(t) = \alpha_G x(t) + d(t) \tag{5.2}$$

in which $\mathbb{E}[x(t)d(t-\tau)] = 0\ \forall\tau$ and the desired signal gain at the nonlinearity output is denoted by α_G which remains constant for a given variance of the $x(t)$. Although the Bussgang theorem requires Gaussian input signal, it is also applicable when the distribution of the input signal is close to Gaussian (e.g. OFDM with large number of active subcarriers) [37]. As a result, Bussgang theory is considered a powerful tool in baseband equivalent analysis of communication signals involving nonlinear PA and has been invoked on numerously in literature [41, 46, 74, 75].

5.1.2 PA Behavioral Modeling

Lets assume signal $x_{RF}(t) = A(t)\cos(\omega_0 t + \phi(t))$ as the input of an RF PA where $A(t)$ and $\phi(t)$ are the actual envelope and phase functions of its equivalent complex baseband signal $x(t) = A(t)e^{j\phi(t)}$. For mathematical tractability, lets assume a simple third-order polynomial nonlinearity for the RF PA, i.e.

$$\begin{aligned} y_{RF}(t) &= a_1 x_{RF}(t) + a_2 x_{RF}^2(t) + a_3 x_{RF}^3(t) \\ &= \frac{a_2 A^2(t)}{2} + \Big[a_1 A(t) + \frac{3a_3 A^3(t)}{4}\Big]\cos(\omega_0 t + \phi(t)) \\ &\quad + \frac{a_2 A^2(t)}{2}\cos(2\omega_0 t + 2\phi(t)) + \frac{a_3 A^3(t)}{4}\cos(3\omega_0 t + 3\phi(t)) \end{aligned} \tag{5.3}$$

where $y_{RF}(t)$ is RF PA output. It is clear from (5.3) that the PA output includes a self-distortion intermodulation term $(\frac{3a_3A^3(t)}{4})\cos(\omega_0 t + \phi(t))$ around input signal center frequency ω_0 which interfere with the in-band signal. Moreover, with 3 times the bandwidth of the input signal it creates

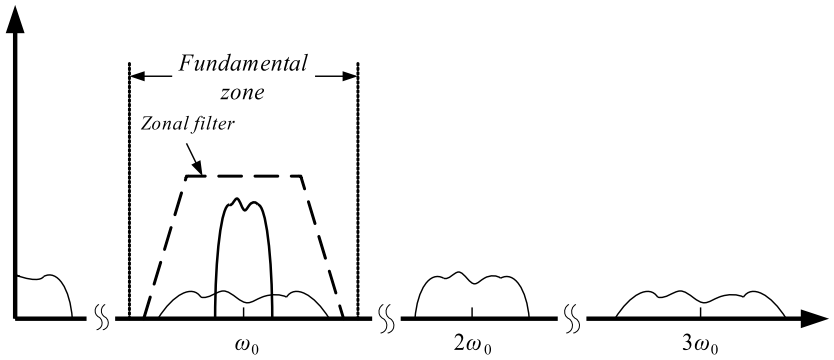

Figure 5.1: Conceptual demonstration for intermodulation terms generated as the result of 2nd and third order nonlinearity. The original signal is located around ω_0. The fundamental zone and the zonal filter are also depicted in this figure.

interference close to the original signal center frequency ω_0 and on the neighboring channels. This phenomenon is referred to in literature as *spectral regrowth* [18, 40, 60]. The other intermodulation terms in (5.3) are far from the original input center frequency as they hit DC, $2\omega_0$, $3\omega_0$, respectively. In modeling RF PAs it is usually assumed that these *harmonics* of the original input signal can be safely removed by implementing a linear bandpass filter [18] also known as zonal filter [76] as the RF frequency is typically assumed to be much larger than the largest envelope frequency of the signal. Consequently, the behavioral models, i.e. the models that describe the input/output relation in the RF PA, are often proposed assuming only the intermodulation terms around and in close vicinity of ω_0. This zone in which the behavioral models are valid are known in literature as the fundamental zone (Fig. 5.1.2).

Now, considering only the fundamental zone it is clear that the center frequency of the RF signal has no influence on the nonlinear behavior of the PA and it is possible to describe the input/output relation of the nonlinearity by the effect of the nonlinearity on the complex envelope of the baseband signal. The example nonlinearity in (5.3) demonstrates this statement as the component in the fundamental zone is $\left[a_1 A(t) + \frac{3a_3 A^3(t)}{4}\right] \cos(\omega_0 t + \phi(t))$ and comparing this term to the input RF signal it is possible to describe the nonlinearity effect in terms of the complex envelope of the PA input/output. In the following we describe such behavioral models which are often used in the literature. The starting point is the complex baseband equivalent behavioral model for a linear PA

$$y(t) = \alpha_{Lin} \times x(t) = \alpha_{Lin} \times A(t) e^{j\phi(t)} \tag{5.4}$$

which means that the RF PA simply amplifies the PA input signal with the *constant* amplitude gain of α_{Lin} which is the linear gain of the PA. However, in practice the PA gain is not constant for the entire range of the input signal envelope. In other words, the overall gain of the PA, $\alpha_A(A(t))$, decreases for large signal amplitudes and $\alpha_A(A(t)) \leq \alpha_{Lin}$ [18]. This so called *gain compression* is generally quantified by 1dB compression point (P1dB) which is the input/output power of the PA in which the PA gains drops by 1 dB. Of course, the compression point of a PA can be described also, depending on the characteristic of the PA, by P3dB which is the input/output power of a PA in which the power gain of the PA drops by 3dB.

One method to depict the input/output characteristic of a PA is to sketch $|\alpha_A(A(t))|^2$ or $\alpha_A(A(t))$ against input signal power or input signal amplitude, respectively. Another equivalently informative presentation method for characterizing $\alpha_A(A(t))$ is so called amplitude modulation to amplitude modulation (AM-AM) plot which is the output power/amplitude of the PA against its input power/amplitude [18, 60].

There are several behavioral models proposed in the literature to approximate a PA AM-AM characteristics. Some of these approximations are technology specific, for instance solid-state power amplifier (SSPA) AM-AM transfer function introduced first in [77] is of the form

$$\alpha_A(A(t)) = \alpha_{Lin} \frac{A(t)}{\left(1 + \left[(\frac{\alpha_{Lin} A(t)}{A_0})^2\right]^p\right)^{\frac{1}{2p}}} \tag{5.5}$$

In which, p determines the smoothness of the AM-AM curve between linear region and saturation. A_0 in turn represents the saturation level for the PA. In Fig. 5.2 the expression in (5.5) is depicted for different values for p and A_0. Another more generic way to approximate a PA AM-AM characteristics for a wider range of PAs is to use baseband polynomial [78] which is defined as follows

$$y(t) = \sum_{l=1}^{L} c_l \; x(t)|x(t)|^{l-1} \tag{5.6}$$

The polynomial model includes only odd order components i.e., $c_l = 0$ when l is even. Now, when the coefficients of the baseband polynomial model are real numbers, i.e., $c_l \in \mathbb{R}$ then this model exclusively approximates $\alpha_A(A(t))$ [78–80].

Another distortion attributed to real world nonlinear PAs is the envelope-dependent phase shift also known as amplitude modulation to phase modulation (AM-PM) distortion [18,60]. This characteristic of the RF PA is usually demonstrated by AM-PM plot in which the phase shift introduced by an RF

PA is sketched against the input signal envelope/power. Considering both AM-AM and AM-PM distortion, the output of a memoryless nonlinear PA is written as

$$y_{RF}(t) = \alpha_A\big(A(t)\big)\cos\big(\omega_0 t + \phi(t) + \psi_A(A(t))\big) \tag{5.7}$$

One example from these types of PAs is traveling-wave tube amplifiers (TWTA). A closed-form expression to capture the AM-AM and AM-PM transfer function of TWTA, also known as Saleh model [76, 81], is presented below as

$$\alpha_A\big(A(t)\big) = \frac{\chi_a A(t)}{1+\kappa_a A^2(t)} \quad \psi_A\big(A(t)\big) = \frac{\chi_\psi A^2(t)}{1+\kappa_\psi A^2(t)} \tag{5.8}$$

in which χ_a, κ_a, χ_ψ and κ_ψ are design parameters of Saleh model. The PAs with AM-AM and AM-PM characteristics can be characterized in more general form using baseband polynomial similar to (5.6) with the difference that the coefficients c_l should be complex numbers [78–80]. Fig.5.3(b), Fig. 5.3(a) and Fig. 5.3(c) show the AM-AM, AM-PM and gain vs input signal power curves for a fifth order approximation of PA characteristic functions. The coefficients of the baseband polynomial are listed below as

$$\begin{aligned} c_1 &= 14.974 + j0.0519 \\ c_3 &= -27.0954 + j4.9680 \\ c_5 &= 21.3936 + j0.4305 \end{aligned} \tag{5.9}$$

The underlying assumption for modeling a PA with AM-AM and AM-PM curve is that the PA AM-AM and AM-PM transfer functions don't change throughout the frequency of the operation i.e., $\alpha_A(A(t))$ and $\psi_A(A(t))$ are independent of frequency. Again, in practice and particularly in wideband applications this assumption is not valid and both gain and phase shift introduced by PA are functions of frequency and the input-output relation for these types of PA is written as

$$y_{RF}(t) = \alpha_A\big(A(t),\omega\big)\cos\big(\omega_0 t + \phi(t) + \psi_A(A(t),\omega)\big) \tag{5.10}$$

One example of frequency dependent gain for an actual PA (AG503-86 by Watkins Johnson) is demonstrated in Fig.5.4. The PA output in these type of PAs doesn't have instantaneous relation to the PA input and is dependent also to prior values of the input signal i.e. exhibit *memory effect* [60, 76]. There are numerous attempts to present closed-form expressions for the PAs exhibiting memory effect. One example of these closed-form expressions is the frequency dependent TWTA model in which all the parameters in (5.8) are assumed to be frequency-dependent and is proposed to model TWTA PAs in wideband applications [81]. Another, rather more general, approach

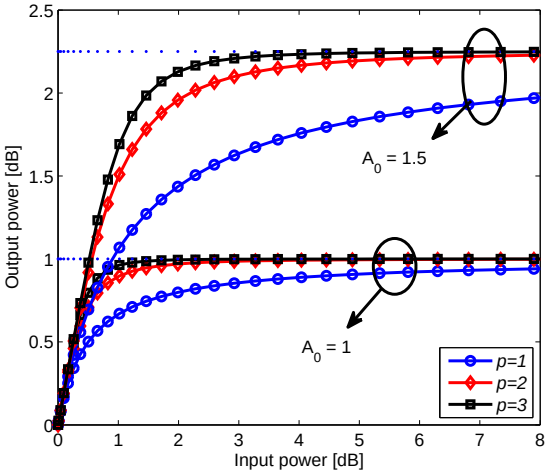

Figure 5.2: The AM-AM characteristics of SSPA from (5.5) for different values of p and A_0.

to model PAs exhibiting memory effect is to describe their input/output relation using Volterra series [76, 78].
In principle, Volterra series is the most general form of polynomial that includes the memory effect. The baseband representation of Volterra series considering only the fundamental zone of the nonlinearity is as follows [76],

$$y(t) = \sum_{l=1}^{(N+1)/2} \int_{-\infty}^{\infty} \int_{-\infty}^{\infty} \cdots \int_{-\infty}^{\infty} h_{2l-1}(\tau_1, \tau_2, \cdots, \tau_{2l-1}) d\tau_1 d\tau_2 \cdots d\tau_{2l-1} \times \prod_{r=1}^{l} x(t-\tau_r) \prod_{p=l+1}^{2l-1} x^*(t-\tau_p) \tag{5.11}$$

in which h_{2l-1}s are *low-pass equivalent kernels* of the Volterra series, $x(t-\tau_r)$ and $x(t-\tau_p)$ are the delayed version of the input signal and N is the number of Volterra kernels which is used in the passband Volterra model. One major issue with modeling nonlinearities in PAs with memory using Volterra series as such is the large number of coefficients in the model. Therefore, in practical applications and in particular for modeling nonlinear PAs exhibiting short-term memory [71, 76] simplified versions of Volterra series are used in which some of the Volterra kernels are ignored. Examples of these types of simplified models are two-box models (e.g., Wiener, Hammerstein) and three-box models (e.g., Wiener-Hammerstein (WH)). One common aspect of these simplified models is the fact that memory behavior of the nonlinear device is modeled as linear transfer functions concatenated with a memoryless nonlinearity. For instance, the Wiener model includes a linear filter followed

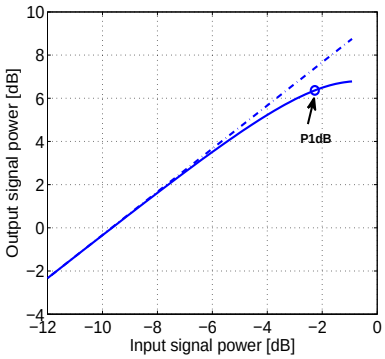

(a) AM-AM characteristics.

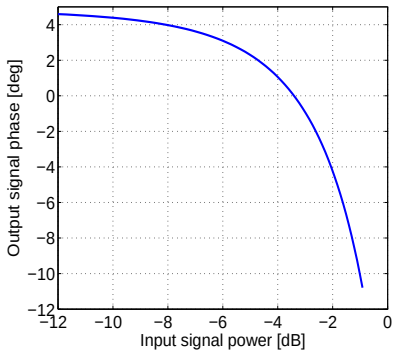

(b) AM-PM characteristics.

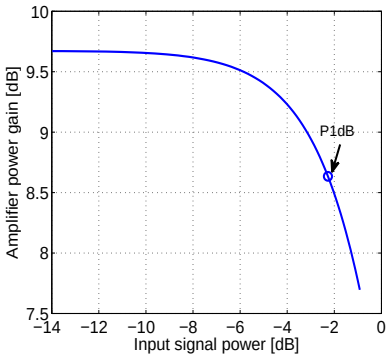

(c) Gain vs input signal power.

Figure 5.3: Different characteristic curves for a fifth order approximation of an actual PA presented in [79]. The P1dB point for this PA is also noted in this figure.

by a static/memoryless nonlinearity (Fig.5.5(a)) and the baseband equivalent input/output relation of this model can be described as follows

$$y(t) = g[h_1(t) * x(t)] = g\left[\int_{-\infty}^{\infty} h_1(\tau)x(t-\tau)d\tau\right] \tag{5.12}$$

in which $h_1(t)$ is the impulse response of H_1, the linear portion of Wiener model, and $g[.]$ is the static nonlinearity behavioral model. Hammerstein model in turn consists of a static nonlinearity followed by a linear filter (Fig.5.5(b)). The input/output relation of Hammerstein model consequently reads

$$y(t) = h_2(t) * g[x(t)] = \int_{-\infty}^{\infty} h_1(\tau)g[x(t-\tau)]d\tau \tag{5.13}$$

in which $h_2(t)$ is the impulse response of H_2, the linear portion of Hammerstein model. Finally, Wiener-Hammerstein is the combination of two linear

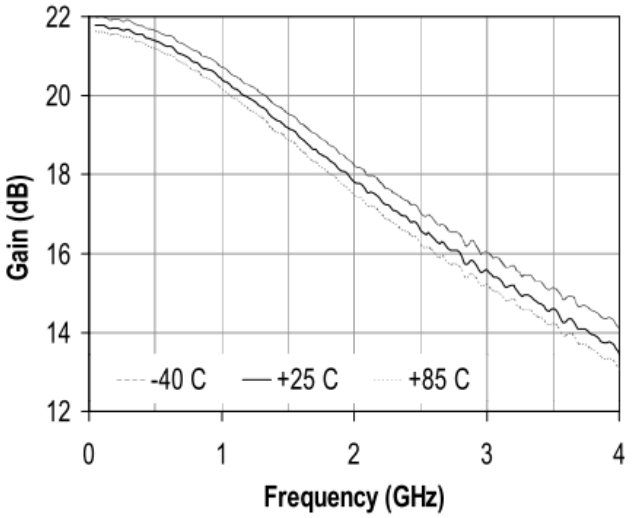

Figure 5.4: Gain dependent behavior of an actual PA (AG503-86) [courtesy of Watkins Johnson].

filters with an static nonlinearity in between, Fig.5.5(c), the input/output relation of which reads

$$y(t) = h_2(t) * g[h_1(t) * x(t)] = \int_{-\infty}^{\infty} h_2(\lambda) g\Big[\int_{-\infty}^{\infty} h_1(\tau) x(t-\lambda-\tau) d\tau\Big] d\lambda \tag{5.14}$$

Depending on the circuit level information from PA, it is possible to implement one of the specialized models which are already described in this section e.g., Saleh model as the memoryless nonlinearity $g[.]$. However, implementing baseband polynomial (5.6) as the static part provides a more general model to describe more variety of PAs input/output responses.

5.2 Linearization Techniques

It is already established earlier in this chapter that nonlinear PA in a transmitter in general generates self-distorting IMD terms as well as interference outside the transmitting band in the form of spectral regrowth. These interfering frequency components are hard to mitigate using linear bandpass filtering as they are in and close to the desired signal band. On the other hand, various communication standards restrict the level of distortion that a transmitter inflicts on in-band signal and outside its transmission band. For instance, the maximum level of distortion that a transmitter front-end including PA is allowed to create on top of itself is set using error vector

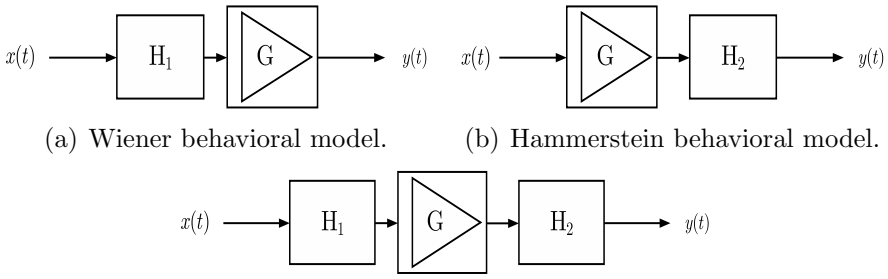

(a) Wiener behavioral model. (b) Hammerstein behavioral model.

(c) Wiener-Hammerstein model.

Figure 5.5: Wiener, Hammerstein and Wiener-Hammerstein behavioral models. H_1 and H_2 are linear filters with $h_1(t)$ and $h_2(t)$ as their impulse response, respectively. The input/output relation for memoryless/static nonlinearity G is represented by function $g[.]$.

magnitude (EVM) [39, 82] which is defined as follows

$$\text{EVM}(in\%) = 100\sqrt{[1 + |\mathbf{d}|^2] - 2\mathbf{d}\cos(\phi_e)} \tag{5.15}$$

in which $\mathbf{d}$ is the measured vector at the output of the transmitter and ϕ_e is the phase error or the phase between measured vector and ideal reference vector. Moreover, the maximum power that a transmitter can emit outside the transmission band is set by, for instance, maximum allowable adjacent channel power ratio (ACPR) [39, 76] in which ACPR is defined as the ratio between the in band signal power to the power of regrowth components in a neighboring band with specified center frequency and bandwidth. One solution to keep the ACPR and the self-interference of the transmitter within the permitted limit is to implement highly linear PA amplifiers such as class A [18, 40] amplifiers. On the other hand, low power efficiency of these class of PAs means these PAs can not be deployed where the power efficiency of the transmitter has high priority [18, 39, 40].

Another solution to meet the required ACPR is to implement more nonlinear, more efficient PAs (e.g., class AB or class B [18,40]) in the transmitter with back-off in the input signal (IBO) or output signal (OBO). The back-off in this context is simply implemented by reducing the input/output signal power to avoid the nonlinear region of the nonlinear PA. Of course, the backed-off PA is not exploited to its maximum power rating and therefore its power efficiency decreases [18,40]. This fact is depicted in Fig. 5.6. All in all, linearity and power efficiency are by design two contradictory requirements, therefore enhancing on former results in degrading the latter and vice versa. One prominent solution to the linearity versus power efficiency dilemma is the utilization of linearizers [69–72], i.e., to implement an efficient nonlinear PA in the transmitter but compensate for the nonlinearity effects using additional circuitry and/or sophisticated signal processing algorithms. Among

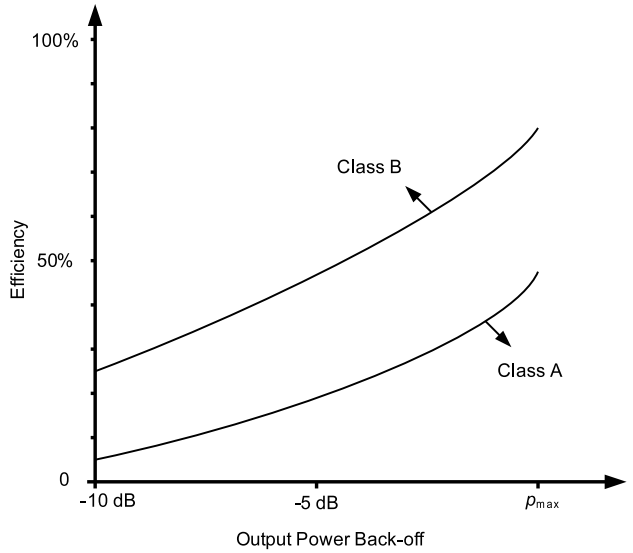

Figure 5.6: Typical efficiency for different classes of amplifiers [82]. Class AB efficiency falls between two limits set by the curves for class A and class B.

the various methods of linearization we briefly describe digital predistortion (DPD) [70–72, 83, 84] in this chapter as a promising and active, yet developing, area of research in linearization field. Moreover, feedforward linearizer as a more established linearization method, and the focus of the rest of this manuscript, is also concisely introduced in this chapter and then discussed in more detail in Chapters 6 and 7.

5.2.1 Digital Predistortion (DPD) linearization

One promising and active, yet developing, area of research in linearization field is baseband/RF digital predistortion (DPD) [70–72, 83, 84]. These types of linearizers typically rely on flexible yet rather complex digital signal processing (DSP) algorithms to invert the nonlinear characteristic of the PA by *predistorting* the PA input to the effect that the overall response of the DPD and PA becomes linear (Fig. 5.7). The first step in designing a DPD is to find a behavioral model that most accurately describes the system level input/output relation of the PA at hand including nonlinearity characteristics and memory effect. This in fact is the most crucial step in designing a DPD as choosing a wrong model for the PA can degrade the performance of DPD. The next step in designing DPD is to find the behavioral model for the DPD based on the assumed PA behavioral model. DPD linearizers are flexible as they can be used with variety of PAs by just changing the parameters of the DPD particularly when more generalized behavioral models e.g., Volterra model and its simplified versions are used for implementing

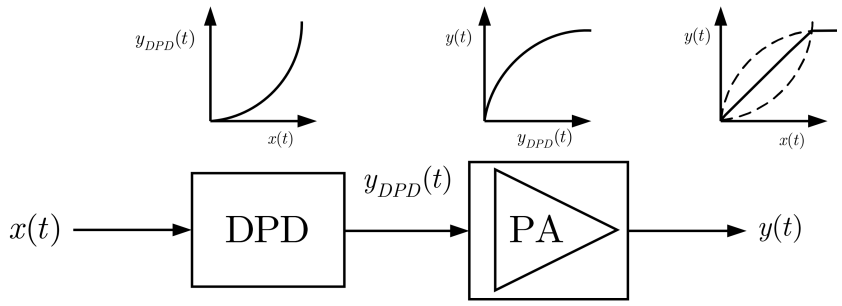

Figure 5.7: Digital predistortion basic operation. DPD transfer characteristics is basically an *expander* to compensate the saturating PA characteristics.

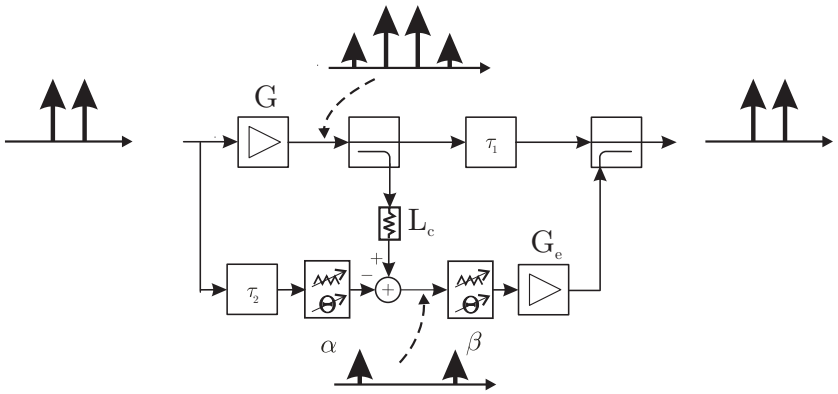

Figure 5.8: Feedforward Lineariztion concept demonstrated using two tone signal as the input of the core PA.

DPD. Moreover, evermore powerful and low-power digital processors provide the opportunity to implement complex DPD models with good power efficiency [69, 72, 79, 85, 86]. On the other hand, in practice since many times the core PAs have saturating type behavior, and the DPD as an inverse of the underlying nonlinearity acts as an expander, the PAPR of the signal entering the core PA is actually increased (compared to the case when there is no DPD). This gives the conclusion, which is fairly well-understood in the literature that DPD typically works well only with relatively mild nonlinearities [69,72,85,86], or it needs to be coupled and jointly designed with PAPR limitation methods. Moreover, DPD in general is not suitable in applications where extremely high linearity is expected from the transmitter (carrier-to-intermodulation-interference ratio $>$ 50 dB) [39, 69, 72, 87]. Such linearity requirements are particularly important in cellular basestations to minimize the intermodulation interferences as the result of the near-far problem [39].

5.2.2 Feedforward Linearizer

The feedforward linearizer is based on the principle of mitigating the interfering IMD frequency components by regenerating and subtracting these components from the PA output at RF. The conceptual diagram of a feedforward linearizer is depicted in Fig. 5.8. In general, feedforward linearizer PA is unconditionally stable, PA model independent and well suited for modern wideband wireless telecommunication applications [39, 41–45]. Moreover, feedforward linearizers can typically handle waveforms with wide bandwidth as well as cases with stringent linearity constraints [39, 69, 85, 87, 88]. The next two chapters of this manuscript are devoted to more detailed analysis of the feedforward linearizer as well as introducing a novel DSP-oriented feedforward linearizer concept as a versatile extension of more traditional all-RF linearizer.

CHAPTER 6

OPERATION AND SENSITIVITY ANALYSIS OF FEEDFORWARD PA LINEARIZER

6.1 Feedforward linearizer Operation Principle

Feedforward principle is one of the most established methods among linearization techniques [39, 41–45]. Feedforward linearizer consists of two separate circuits, signal cancellation (SC) and error cancellation (EC). The SC circuit extracts the intermodulation distortion (IMD) components from the PA output, the PA being referred to as *the core PA* from this point on. The EC circuit then subtracts the isolated IMD components, with correct gain and phase, from the core PA output [39, 41–43]. We start the analysis of feedforward linearizer, illustrated in Fig. 6.1, from the SC circuit and by writing the input/output relation of the core PA. It is deducted from the Bussgang theorem [73] that the output of a memoryless nonlinearity with a zero-mean Gaussian distributed input is a scaled version of the input signal plus an IMD term uncorrelated with the input signal. Although the Bussgang theorem requires a Gaussian input signal, it is also applicable when the distribution of the input signal is close to Gaussian (e.g., OFDM with a large number of active subcarriers) [37]. Therefore, assuming the core PA is memoryless, its output can be written as,

$$v_{a,RF}(t) = \alpha_G v_{m,RF}(t) + v_{d,RF}(t) \tag{6.1}$$

The core PA output, the core PA input, and the IMD components are denoted by $v_{a,RF}(t)$, $v_{m,RF}(t)$, and $v_{d,RF}(t)$, respectively. The desired signal gain of

the core PA is α_G. Subsequently, the discrete-time baseband equivalent of (6.1) reads

$$v_a(n) = \alpha_G\, v_m(n) + v_d(n) \tag{6.2}$$

Given perfect delay match between the lower and the upper branches of the SC circuit, the output of the SC circuit yields

$$\begin{aligned} v_e(n) &= \sqrt{l_c} v_a(n) - \alpha v_m(n) \\ &= \left(\alpha_G \sqrt{l_c} - \alpha\right) v_m(n) + \sqrt{l_c} v_d(n) \end{aligned} \tag{6.3}$$

The power loss of the attenuator $\mathrm{L_c}$ is denoted by l_c and the complex valued coefficient α represents the gain and the phase rotation provided by the vector modulator in the SC circuit. The SC circuit output is then phase and amplitude corrected using the vector modulator in the EC circuit. Afterward the resulting signal is amplified by the error amplifier and finally subtracted from the core PA output. Hence, the overall feedforward linearizer output reads

$$\begin{aligned} v_o(n) &= v_a(n) - \beta\sqrt{g_e} v_e(n) \\ &= \left(\alpha_G \left(1 - \beta\sqrt{g_e l_c}\right) + \alpha\beta\sqrt{g_e}\right) v_m(n) + \left(1 - \beta\sqrt{g_e l_c}\right) v_d(n) \end{aligned} \tag{6.4}$$

where the small signal gain of the error amplifier is presented by g_e and the complex valued coefficient β represents the gain and phase rotation provided by the vector modulator in the EC circuit. Considering the overall output expression for the feedforward linearizer in (6.4) the optimum coefficients for the SC and EC circuits are

$$\begin{aligned} \alpha_{opt} &= \alpha_G \sqrt{l_c} \\ \beta_{opt} &= 1/\sqrt{g_e l_c} \end{aligned} \tag{6.5}$$

These values for α and β maintain the original gain of the core PA and eliminates the IMD terms at the feedforward linearizer output yielding $v_o(n) = v_{o,opt}(n) = \alpha_G v_m(n)$ [39, 41].

6.2 Linearizer Performance Under the SC and EC Coefficient Errors

The optimum coefficients presented in previous section guarantees complete mitigation of the IMD terms and preserves the gain of the core PA. However, the optimum values for α and β are functions of the linear gain of the core PA, attenuation of the path in the SC circuit and error amplifier gain, respectively. The nominal values of these circuit parameters are already known, up to the

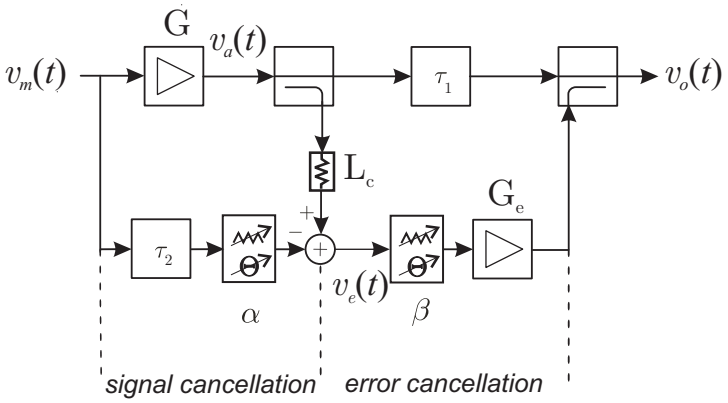

Figure 6.1: Baseband equivalent feedforward power amplifier linearizer structure.

tolerances of the circuit components, in production stage and can be used to calibrate SC and EC circuits. Unfortunately, the characteristics of the circuit components changes during the life time of the feedforward linearizer due to environment parameters and aging of the components. Hence, the original estimated values for α and β are no longer adequate and the performance of feedforward linearizer in terms of IMD mitigation and provided gain is affected. In the following we study the effects of the errors in the SC and EC circuit coefficients on the performance of feedforward linearizer when the core PA exhibits memory and in the case of the memoryless core PA. More detailed presentation and analysis on this topic can be found in [P5]

6.2.1 Memoryless Core PA

As shown in the previous Section, the optimum values of the feedforward coefficients,α_{opt} and β_{opt}, eliminate the IMD components and provide the required amplification for the input signal. However, any coefficient deviation from the optimum value causes the degradation of performance in feedforward structure in terms of IMD attenuation and reduction in the overall desired signal gain. To study the effects of such deviations in the feedforward coefficients, we deploy the signal-to-interference ratio (SIR) as the performance measure of the linearizer. The interference in this context is the IMD component, and thus based on (6.2), the basic expression for the SIR at the core PA output can be formulated as

$$\mathrm{SIR}_a = \frac{|\alpha_G|^2 \mathbb{E}[|v_m(n)|^2]}{\mathbb{E}[|v_d(n)|^2]} = \frac{|\alpha_G|^2 p_m}{p_d} \tag{6.6}$$

Here p_m is the power of the input signal and p_d the power of the corresponding IMD component at the core PA output. Based on (6.4), the corresponding

SIR at the overall linearizer output, in turn, is of the form

$$\mathrm{SIR}_o = \frac{|\alpha_G + \beta\alpha\sqrt{g_e} - \beta\alpha_g\sqrt{g_e l_c}|^2 p_m}{|1 - \beta\sqrt{g_e l_c}|^2 p_d} \tag{6.7}$$

Clearly, the optimum coefficients α_{opt} and β_{opt} lead to infinite suppression of IMD, and also any deviation from these optimal values result in imperfect IMD suppression.

Next, in order to explore the relationship between the coefficient deviation and the feedforward linearizer performance, a new measure is introduced. This measure, called *relative* SIR (r-SIR) in the following, is the ratio between SIR_o and SIR_a and represents the improvement in the signal quality obtained by employing the linearizer. Now, the expression for this r-SIR can be directly obtained using (6.6) and (6.7), and reads

$$\mathrm{r-SIR} = \frac{\mathrm{SIR}_o}{\mathrm{SIR}_a} = \frac{|\alpha_G + \beta\alpha\sqrt{g_e} - \beta\alpha_G\sqrt{g_e l_c}|^2}{|\alpha_G|^2|1 - \beta\sqrt{g_e l_c}|^2} \tag{6.8}$$

Then, for analysis purposes, we further define the normalized coefficient errors of the SC and EC circuits as

$$\begin{aligned} \xi_\alpha &= \frac{\alpha - \alpha_{opt}}{\alpha_{opt}} = \frac{\alpha}{\alpha_G\sqrt{l_c}} - 1 \\ \xi_\beta &= \frac{\beta - \beta_{opt}}{\beta_{opt}} = \beta\sqrt{l_c g_e} - 1 \end{aligned} \tag{6.9}$$

Writing now α and β in terms of the normalized errors ξ_α and ξ_β in (6.8) reads

$$\mathrm{r-SIR} = \frac{|1+\xi_\alpha + \xi_\alpha\xi_\beta|^2}{|\xi_\beta|^2} \tag{6.10}$$

One very interesting conclusion obtained from (6.10) is that the improvement in the SIR, with any reasonable range for ξ_α and ξ_β (i.e. $|\xi_\alpha + \xi_\alpha\xi_\beta| \ll 1$), is directly proportional to the reciprocal of $|\xi_\beta|^2$. This, in turn, directly implies that the accuracy of the EC circuit coefficient is the critical factor in order to achieve good linearization performance, while the accuracy requirement for the SC coefficient is much lower. Moreover, expressing (6.3) in terms of ξ_α reads

$$v_e(n) = -\xi_\alpha\left(\alpha_G\sqrt{l_c}\right)v_m(n) + \sqrt{l_c}v_d(n) \tag{6.11}$$

Therefore, very large errors in ξ_α causes insufficient attenuation of the main signal component in the SC circuit which consequently degrades the efficiency of the error amplifier and the desired signal gain of the linearizer. It is worth noting also that in the case where different adaptive or iterative methods

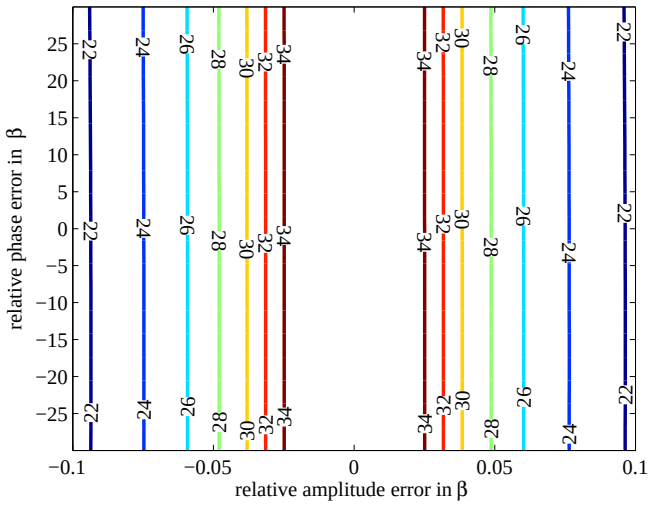

Figure 6.2: Achievable r-SIR levels [in dB] with respect to ξ_β. The relative error in ξ_α is 0.2 in amplitude and 10 degree in phase.

are used to obtain the SC and EC loop coefficients simultaneously, errors or deviations in ξ_α can also significantly increase the deviations in ξ_β [41].

Some example graphical illustrations of the achievable r-SIR levels with example coefficient deviations of $\{|\xi_\beta| \leq 0.1$, -30° $\leq \angle\xi_\beta \leq 30°\}$ and $\{|\xi_\alpha|$=0.2, $\angle\xi_\alpha$=10°$\}$ are presented in Fig. 6.2. Clearly, based on the figure, high r-SIR values (and thus high IMD attenuations) are obtainable despite the poor accuracy of ξ_α, as long as the relative errors in β are small (e.g., up to 30 dB for $\xi_\beta = 5 \times 10^2$). This figure also demonstrates that errors in the phase of β do not affect the r-SIR significantly. This is ,of course, clear from (6.10) already. Fig. 6.3, in turn, shows the achievable r-SIR with $\{|\xi_\alpha| \leq 0.1$, -30° $\leq \angle\xi_\alpha \leq$ 30°$\}$ and $\{|\xi_\beta|$=0.2, $\angle\xi_\beta$=10°$\}$. This clearly verifies and demonstrates the earlier conclusion that the linearizer operation, in terms of IMD reduction (here r-SIR) is fairly robust against inaccuracies in α.

6.2.2 Core PA Exhibiting Memory

In this Section, we extend the analysis of the previous Section to the more practical case in which the core PA exhibits mild frequency-selectivity in its response, i.e., contains memory. To model such memory in the core PA, the widely-applied Wiener model, depicted in Figure 6.4, is selected. The Wiener model is generally a cascade of a linear time-invariant filter (modeling the memory) and a memoryless nonlinearity (modeling the IMD). Now, generalizing the previous derivations, the output of the core PA can first be written

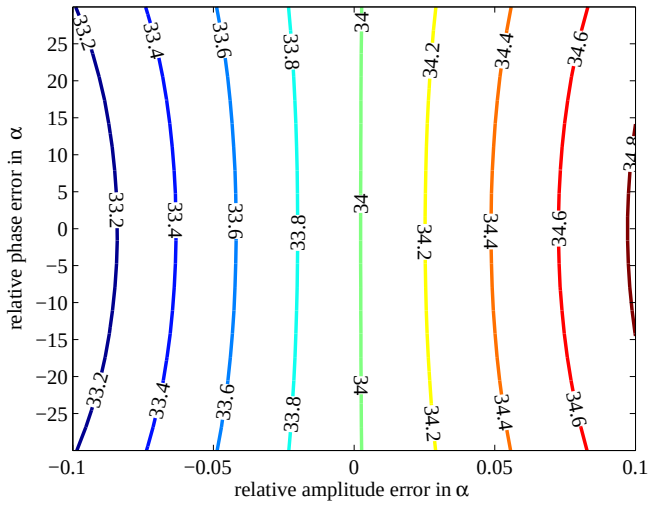

Figure 6.3: Achievable r-SIR levels [in dB] with respect to ξ_α. The relative error in ξ_β is 0.2 in amplitude and 10 degree in phase.

as

$$v_{a,RF}(t) = \alpha_G \int_{-\infty}^{+\infty} h(\tau) v_{m,RF}(t-\tau) d\tau + v_{d,RF}(t) \tag{6.12}$$

For analysis purposes, the corresponding causal discrete-time baseband equivalent signal is defined as

$$v_a(n) = \alpha_G \sum_{k=0}^{N-1} h(k) v_m(n-k) + v_d(n) \tag{6.13}$$

For notational convenience in the later analysis, we further assume that the linear filter $h(t)$ modeling the memory is a normalized minimum phase FIR filter (i.e., h(0)=1) of length N. This is clearly justified since the frequency-selectivity of practical amplifiers is typically rather mild within any reasonable observation bandwidth. Then, after some fairly straight-forward manipulations, the output of the SC circuit can be written as

$$v_e(n) = (\alpha_0 \sqrt{L_c} - \alpha) v_m(n) + \sum_{k=1}^{N-1} h(k) v_m(n-k) + \sqrt{L_c} v_d(n) \tag{6.14}$$

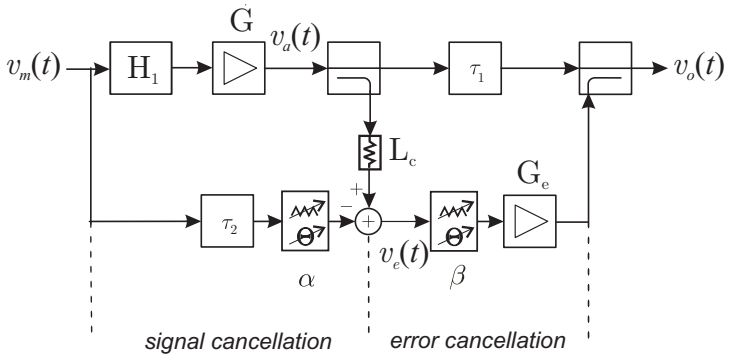

Figure 6.4: Baseband equivalent feedforward power amplifier linearizer structure withe a core PA that exhibits memory. Here the core PA is modeled by concatenation of a finite impulse response (FIR) filter and a memoryless nonlinear function.

Now, substituting (6.13) and (6.14) in (6.4) yields the output of the feedforward structure as

$$v_o(n) = (\alpha_G(1-\beta\sqrt{g_e l_c}) + \alpha\beta\sqrt{g_e})v_m(n) \tag{6.15}$$
$$+ \alpha_G(1-\beta\sqrt{g_e l_c})\sum_{k=1}^{N-1} h(k)v_m(n-k) + (1-\beta\sqrt{g_e l_c})v_d(n)$$

Here one can notice the interesting fact that setting the feedforward parameters to the optimum values derived in the case of memoryless PA in Section 6.2.1 (i.e. $\alpha_{opt} = \alpha_G\sqrt{l_c}$ and $\beta_{opt} = 1/\sqrt{g_e l_c}$), nulls both the IMD as well as the memory term and also provides the desired amplification for the input signal.

Next, in order to define the relationship between the coefficient errors and the performance of the feedforward linearizer with memory, we determine the r-SIR again in a similar manner as in the memoryless case. First, based on (6.13), the SIR at the output of the core PA reads

$$\mathrm{SIR}_{\mathrm{a-Wiener}} = \frac{|\alpha_G|^2 p_m}{|\alpha_G|^2 \mathrm{E}[|\sum_{k=1}^{N-1} h(k)v_m(n-k)|^2] + p_d} \tag{6.16}$$

Note that the linear distortion is also treated as interference.The corresponding SIR at the feedforward linearizer output is obtained using (6.15) and reads

$$\mathrm{SIR}_{\mathrm{o-Wiener}} = \frac{1}{|1-\beta\sqrt{g_e l_c}|^2} \times \frac{|\alpha_G + \beta\alpha\sqrt{g_e} - \beta\alpha_G\sqrt{g_e l_c}|^2 p_m}{|\alpha_G|^2 \mathbb{E}[|\sum_{k=1}^{N-1} h(k)v_m(n-k)|^2] + p_d} \tag{6.17}$$

Then, the relative SIR (r-SIR) is obtained as the ratio of (6.16) and (6.17), and using also the earlier definitions of ξ_α and ξ_β, is given by

$$\mathrm{r-SIR}_{\mathrm{Wiener}}=\frac{|\alpha_G+\beta\alpha\sqrt{g_e}-\beta\alpha_0\sqrt{g_e l_c}|^2}{|\alpha_G|^2|1-\beta\sqrt{g_e l_c}|^2}=\frac{|1+\xi_\alpha+\xi_\alpha\xi_\beta|^2}{|\xi_\beta|^2} \tag{6.18}$$

which, basically, is the same expression for $\mathrm{r-SIR}$ for the memoryless case in 6.10. Note that, in the memory case as opposed to the memoryless case, the interference component is assumed to contain not only the IMD but also the memory components (linear distortion). This interpretation of interference is mainly motivated by the feedforward linearizer concept in which any component at the PA output other than the scaled version of the input signal is considered to be interference and is canceled out at the linearizer output. The expression for r-SIR in (6.8) and (6.18) provides designers with a tool to calculate the maximum permitted deviation in the adjustment of the SC and EC circuit coefficients depending on the linearization requirement in terms of IMD mitigation. The maximum permitted deviation of the coefficients in turn have an impact on the choice of estimation algorithm parameters (e.g., step size and number of samples in adaptive algorithms) which is used in the estimation of these coefficients. One practical application example of expressions in (6.8) and (6.18) is presented in [P5].

CHAPTER 7

DSP-ORIENTED FEEDFORWARD AMPLIFIER LINEARIZER

A major obstacle in the way of feedforward linearizer to become the dominant method of linearization is the rigid and bulky nature of this structure as it is currently implemented entirely in the RF segment of the transmitter front-end. This is particularly at odds with recent paradigm-shifting data transmission system design concepts such as software-defined radio (SDR) [3] and cognitive radio [63].

In the DSP-oriented implementation of feedforward linearizer (DSP-FF) [P2], [P6], on the other hand, the lower branches of EC and SC circuits are completely implemented in baseband DSP rather than analog RF. As a result, the IMD components which are needed to linearize the core PA are extracted entirely in the DSP portion of the transmitter. At implementation level, additional demodulator and modulator together with proper data converters are needed, compared to all-RF feedforward linearizers. It should be noted, however, that also the so-called all-RF linearizers actually utilize similar additional circuitry and DSP algorithms to calibrate and possibly also track the changes of the SC and EC circuit components [41, 43, 46, 89–93]. Thus in this sense, the hardware complexities of the existing linearizers and the proposed one are fairly similar with the difference that here also major part of the core linearization processing is done in DSP.

7.1 DSP-FF Basic Operation Principle

The DSP-FF shown in Fig.7.1 is structurally similar to the all-RF feedforward linearizer - it consists of separate SC and EC circuits. However, these circuits in DSP-FF are implemented partly in DSP regime using I/Q demodulator

and analog-to-digital converter (ADC) as well as digital-to-analog converter (DAC) and I/Q modulator. Both the SC and EC circuits employ two coefficients in the form of a widely-linear filter [94] to counter for the differences in the characteristics of the couplers, attenuators and amplifiers, and also for the gain and the phase imbalances of the used I/Q modulator (IQM) and demodulator (IQD) in the IMD extraction and subtraction process [P2], [P6].

The three devised RF switches - S_1,S_2, and S_3 in Fig.7.1 - are used to isolate the RF section of SC from EC circuit in calibration stages. Using different combinations (open/close) of these switches it is possible to estimate the coefficients of EC and SC circuits independently. As for Fig. 7.1, the amplifier is in the transmission mode when the RF switches S_1 and S_2 are closed and S_3 is open. In the following, principal signal analysis of the proposed linearizer is carried out.

7.1.1 SC Circuit Signal Analysis

Invoking on the Bussgang theorem, the ideal discrete-time baseband equivalent digital version of the core PA output is given in (6.2). Here the core PA output is downconverted to the baseband using practical IQD circuitry which yields

$$\begin{aligned} v_{a,iq}(n) &= \sqrt{l_c}\, k_{d,1} v_a(n) + \sqrt{l_c}\, k_{d,2} v_a^*(n) \\ &= \left[\sqrt{l_c}\, \alpha_G\, k_{d,1}\, v_m(n) + \sqrt{l_c}\, k_{d,1} v_d(n)\right] + \\ &\left[\sqrt{l_c}\, \alpha_G^*\, k_{d,2}\, v_m^*(n) + \sqrt{l_c}\, k_{d,2} v_d^*(n)\right]. \end{aligned} \tag{7.1}$$

The downconverted digital core PA output is denoted by $v_{a,iq}(n)$. Here l_c models all the signal losses from the core PA output to the baseband (i.e coupler, attenuator, ADC and IQD). The impairments in the IQD yield imperfect image signal attenuation [15]. Therefore, the conjugate terms $v_m^*(n)$ and $v_d^*(n)$ appear in $v_{a,iq}(n)$. The imbalance coefficients [15] of the IQD are represented by $k_{d,1}$, $k_{d,2}$. Hereafter, the DSP-FF analysis is performed using matrix interpretation which is mainly motivated by the block-based estimation algorithms for estimation of EC and SC circuit which are described later in this chapter. The matrix representation of (7.1) over a block of N samples reads,

$$\mathbf{V}_{a,iq} = \mathbf{V}_m \mathbf{\Lambda}_G \mathbf{K}_d^T + \mathbf{V}_d \mathbf{K}_d^T \tag{7.2}$$

where

$$\mathbf{\Lambda}_G = \begin{bmatrix} \alpha_G & 0 \\ 0 & \alpha_G^* \end{bmatrix}, \qquad \mathbf{K}_d = \sqrt{l_c} \begin{bmatrix} k_{d,1} & k_{d,2} \\ k_{d,2}^* & k_{d,1}^* \end{bmatrix}$$

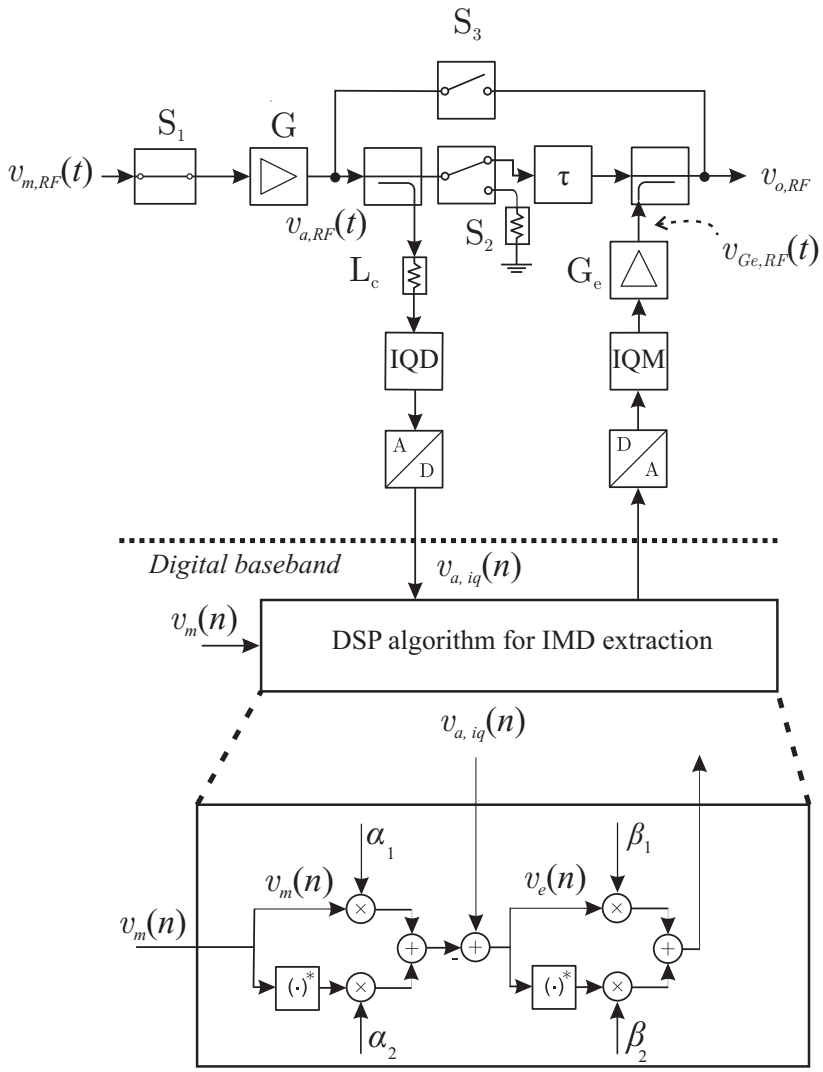

Figure 7.1: DSP-oriented feedforward power amplifier linearizer structure.

and the matrices $\mathbf{V}_m$, $\mathbf{V}_d$ and $\mathbf{V}_{a,iq}$ are fashioned as $\mathbf{V}_m = [\mathbf{v}_m \;\; \mathbf{v}_m^*]$,$\mathbf{V}_d = [\mathbf{v}_d \;\; \mathbf{v}_d^*]$ and $\mathbf{V}_{a,iq} = [\mathbf{v}_{a,iq} \;\; \mathbf{v}_{a,iq}^*]$. The vectors $\mathbf{v}_{a,iq}$, $\mathbf{v}_m$ and $\mathbf{v}_d$ are constructed from the samples of $v_{a,iq}(n)$, $v_m(n)$ and $v_d(n)$, respectively, as $\mathbf{v}_{a,iq} = [v_{a,iq}(1),\ v_{a,iq}(2),\ \ldots\ , v_{a,iq}(N)]^T$, $\mathbf{v}_m = [v_m(1),\ v_m(2),\ \ldots\ , v_m(N)]^T$ and $\mathbf{v}_d = [v_d(1),\ v_d(2)\ \ldots\ , v_d(N)]^T$.

The SC circuit extracts the IMD term from $v_{a,iq}(n)$ by processing the digital transmit data $v_m(n)$ with a widely-linear filter and subtracting it

from $v_{a,iq}(n)$. This is written here as

$$\begin{aligned} v_e(n) &= v_{a,iq}(n) - (\alpha_1 v_m(n) + \alpha_2 v_m^*(n)) \\ &= \left[\left(\sqrt{l_c}\,\alpha_G\,k_{d,1} - \alpha_1\right)\,v_m(n) + \sqrt{l_c}\,k_{d,1}v_d(n)\right] + \\ &\quad \left[\left(\sqrt{l_c}\,\alpha_G^*\,k_{d,2} - \alpha_2\right)\,v_m^*(n) + \sqrt{l_c}\,k_{d,2}v_d^*(n)\right] \end{aligned} \tag{7.3}$$

The two coefficients α_1 and α_2 are implemented in the form of a widely-linear filter to cancel out the input signal component as well as its conjugate. The SC circuit output can be written in matrix form following (7.2) and (7.3) as

$$\mathbf{V}_e = \mathbf{V}_{a,iq} - \mathbf{V}_m\mathbf{A}^T = \mathbf{V}_m\left(\mathbf{\Lambda}_G\mathbf{K}_d^T - \mathbf{A}^T\right) + \mathbf{V}_d\mathbf{K}_d^T \tag{7.4}$$

where

$$\mathbf{A} = \begin{bmatrix} \alpha_1 & \alpha_2 \\ \alpha_2^* & \alpha_1^* \end{bmatrix}$$

The matrix $\mathbf{V}_e$ is constructed using the vectors $\mathbf{v}_e$ and $\mathbf{v}_e^*$ as $\mathbf{V}_e = [\mathbf{v}_e \;\; \mathbf{v}_e^*]$ in which the vector $\mathbf{v}_e$ is constructed from the samples of $v_e(n)$, i.e., $\mathbf{v}_e = [v_e(1),\; v_e(2),\; \ldots\; , v_e(N)]^T$. The optimum value for the matrix $\mathbf{A}$ eliminates all the input signal components from $\mathbf{V}_{a,iq}$, setting $\mathbf{V}_e = \mathbf{V}_{e,opt} = \mathbf{V}_d\mathbf{K}_d^T$ or in signal notations

$$v_{e,opt}(n) = \sqrt{l_c}\,(k_{d,1}v_d(n) + k_{d,2}v_d^*(n)) \tag{7.5}$$

Therefore, the optimum SC coefficients read from (7.4) as $\mathbf{\Lambda}_G\mathbf{K}_d^T - \mathbf{A}_{opt}^T = \mathbf{O}$ or

$$\mathbf{A}_{opt} = \begin{bmatrix} \alpha_{1,opt} & \alpha_{2,opt} \\ \alpha_{2,opt}^* & \alpha_{1,opt}^* \end{bmatrix} = \mathbf{K}_d\mathbf{\Lambda}_G \tag{7.6}$$

Note that $\mathbf{\Lambda}_G$ is a diagonal matrix and therefore $\mathbf{\Lambda}_G^T = \mathbf{\Lambda}_G$. The optimum values for α_1 and α_2, from (7.6), are thus

$$\begin{aligned} \alpha_{1,opt} &= \sqrt{l_c}\alpha_G k_{d,1} \\ \alpha_{2,opt} &= \sqrt{l_c}\alpha_G^* k_{d,2} \end{aligned} \tag{7.7}$$

7.1.2 EC Circuit Signal Analysis

The role of EC circuit is to linearly amplify the IMD term which is extracted by SC circuit and to subtract it from the core PA output. A widely-linear filter with two coefficients, β_1 and β_2, is utilized also here in EC circuit to compensate for the finite image attenuation [16] in IQD, from the IMD component point of view, and in IQM as well as phase/gain imbalance between

L_c and G_e. Therefore, the IMD term at the EC circuit output, or the whole signal at the EC circuit output when $\alpha_1 = \alpha_{1,opt}$ and $\alpha_2 = \alpha_{2,opt}$, reads

$$\begin{aligned} v_{de}(n) &= \sqrt{g_e}\Big(k_{m,1}(\beta_1 v_{e,opt} + \beta_2 v_{e,opt}^*) + k_{m,2}(\beta_1 v_{e,opt} + \beta_2 v_{e,opt}^*)^*\Big) \\ &= k_{t,1}\, v_d(n) + k_{t,2}\, v_d^*(n) \end{aligned} \tag{7.8}$$

The I/Q imbalance coefficients for IQM are represented by $k_{m,1}$ and $k_{m,2}$ while the overall I/Q imbalance coefficients of IQD, IQM, and the widely-linear filter in the EC circuit are given by

$$\begin{aligned} k_{t,1} &= \sqrt{l_c g_e}\Big(k_{m,1}\left(\beta_1 k_{d,1} + \beta_2 k_{d,2}^*\right) + k_{m,2}\left(\beta_1^* k_{d,2}^* + \beta_2^* k_{d,1}\right)\Big) \\ k_{t,2} &= \sqrt{l_c g_e}\Big(k_{m,1}\left(\beta_1 k_{d,2} + \beta_2 k_{d,1}^*\right) + k_{m,2}\left(\beta_1^* k_{d,1}^* + \beta_2^* k_{d,2}\right)\Big) \end{aligned} \tag{7.9}$$

Considering blocks of N samples of $v_{de}(n)$ and $v_d(n)$, the expression relating the IMD term at the PA output and DSP-FF output, presented in (7.8), can be written in matrix form as

$$\mathbf{V}_{de} = \mathbf{V}_d\left(\mathbf{K}_m \mathbf{B} \mathbf{K}_d\right)^T \tag{7.10}$$

where

$$\mathbf{B} = \begin{bmatrix} \beta_1 & \beta_2 \\ \beta_2^* & \beta_1^* \end{bmatrix}, \qquad \mathbf{K}_m = \sqrt{g_e}\begin{bmatrix} k_{m,1} & k_{m,2} \\ k_{m,2}^* & k_{m,1}^* \end{bmatrix}$$

and the matrix $\mathbf{V}_{de} = [\mathbf{v}_{de} \;\; \mathbf{v}_{de}^*]$ where $\mathbf{v}_{de} = [v_{de}(1)\; v_{de}(2)\; \ldots\; v_{de}(N)]^T$. The optimum EC circuit coefficients, $\beta_{1,opt}$ and $\beta_{2,opt}$, should cancel out the imbalance effects of IQD and IQM as well as the imbalances between L_c and G_e from the IMD components point of view. That means the generated IMD estimate coming from the EC circuit, $v_{de}(n)$, equals the original IMD term $v_d(n)$, i.e., $v_{de}(n) = v_d(n)$. Thus, based on (7.10), the optimum EC circuit coefficients fulfill $\mathbf{K}_m \mathbf{B}_{opt} \mathbf{K}_d = \mathbf{I}_{2\times 2}$ meaning

$$\mathbf{B}_{opt} = \begin{bmatrix} \beta_{1,opt} & \beta_{2,opt} \\ \beta_{2,opt}^* & \beta_{1,opt}^* \end{bmatrix} = \mathbf{K}_m^{-1}\mathbf{K}_d^{-1} \tag{7.11}$$

The optimum EC coefficients in terms of IQD and IQM imbalance coefficients read from (7.11) as

$$\begin{aligned} \beta_{1,opt} &= \frac{k_{m,1}^* k_{d,1}^* + k_{m,2} k_{d,2}^*}{\sqrt{g_e l_c}\left(|k_{m,1}|^2 - |k_{m,2}|^2\right)\left(|k_{d,1}|^2 - |k_{d,2}|^2\right)} \\ \beta_{2,opt} &= -\frac{k_{m,1}^* k_{d,2} + k_{m,2} k_{d,1}}{\sqrt{g_e l_c}\left(|k_{m,1}|^2 - |k_{m,2}|^2\right)\left(|k_{d,1}|^2 - |k_{d,2}|^2\right)} \end{aligned} \tag{7.12}$$

7.2 Least-Squares Methods for SC and EC Coefficient Estimation

In practice, the exact values of l_c, α_G, and g_e as well as the I/Q modulator and demodulator imbalance characteristics $k_{m,1}$, $k_{m,2}$, $k_{d,1}$, and $k_{d,2}$ defining the previously-derived optimum solutions for $\mathbf{A}_{opt}$ and $\mathbf{B}_{opt}$ are all unknown. Thus some practical parameter estimation mechanisms are needed to calibrate the linearizer. Here in this Section, a two-step LS model fitting approach is proposed. These algorithms are designed to estimate the coefficients of SC and EC circuits independent from each other. As a result, the inaccuracies in the estimation of either coefficients don't affect the estimation of the other set of coefficients. This is an advantage compared to the algorithms that estimate these coefficients jointly as proposed e.g. in [41], which suffer from this inter-dependance.

One should take note that the estimation methods which are proposed in the following are, in fact, calibration algorithms and specifically designed for the initial calibration of the linearizer in production stage. These algorithms can also be used to track the changes in the circuitry during the normal operation of the DSP-FF. However, during the estimation period, the data transmission will be interrupted.

7.2.1 Estimating SC Coefficients α_1 and α_2

As derived in Section 7.1.1 in (7.6), the optimum SC coefficients α_1 and α_2 depend on $\mathbf{K}_d\mathbf{\Lambda}_G$. In order to estimate $\mathbf{K}_d\mathbf{\Lambda}_G$ using LS model fitting, the principle depicted in Fig. 7.2 is proposed. Here the RF switches S_2 and S_3 are open while S1 is closed. Note that while open, S_2 should be terminated properly to allow the power flow through the preceding coupler with minimum power reflection (Fig. 7.2). The signal $v_{m,RF}(t)$ is fed to the core PA. Thereafter the core PA output $v_{a,RF(t)}$ is downconverted to the baseband and digitized. M_α samples of the baseband signals $v_{a,iq}(n)$ and $v_m(n)$ are stored in two matrices $\mathbf{V}_{a,iq}$ and $\mathbf{V}_m$ respectively. The relation between the two matrices reads from (7.2) and (7.6)

$$\mathbf{V}_{a,iq} = \mathbf{V}_m\mathbf{A}_{opt}^T + \mathbf{V}_d\mathbf{K}_d^T + \mathbf{V}_\gamma \tag{7.13}$$

The matrix $\mathbf{V}_\gamma = [\mathbf{v}_\gamma\ \mathbf{v}_\gamma^*]$ where $\mathbf{v}_\gamma = [v_\gamma(1), v_\gamma(2), ..., v_\gamma(M_\alpha)]^T$ and $v_\gamma(n)$ models the baseband digital version of the measurement noise which is assumed to be zero-mean, white and Gaussian. Thereafter, the least squares (LS) estimator for $\mathbf{A}_{opt}$ reads

$$\begin{aligned}\mathbf{A}_{LS,\gamma} &= \left(\mathbf{V}_m^\dagger\mathbf{V}_{a,iq}\right)^T \\ &= \mathbf{A}_{opt} + \mathbf{K}_d(\mathbf{V}_m^\dagger\mathbf{V}_d)^T + (\mathbf{V}_m^\dagger\mathbf{V}_\gamma)^T\end{aligned} \tag{7.14}$$

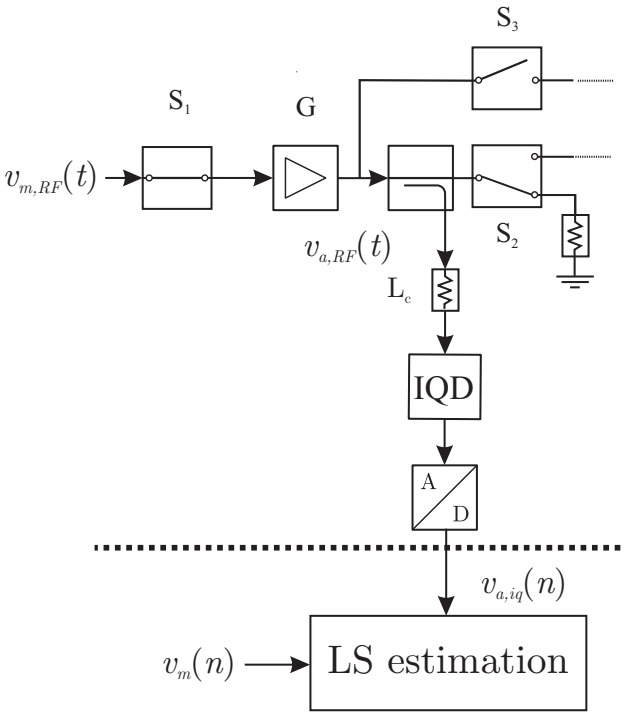

Figure 7.2: Estimating α_1 and α_2 in calibration stage.

The behavioral analysis of this estimator in terms of convergence to the optimum value $\mathbf{A}_{opt}$ in general and for arbitrary values of M_α is not a straight forward task. However, assuming ergodic input signal and measurement noise, $\mathbf{A}_{LS,\gamma} = \mathbf{A}_{opt}$ when $M_\alpha \to \infty$ [P2]. Rewriting the preceding statement in terms of actual SC circuit coefficients yields,

$$\begin{aligned} \alpha_{1,LS}^{\infty} &= \alpha_{1,LS}\Big|_{M_\alpha \to \infty} = \alpha_{1,opt} \\ \alpha_{2,LS}^{\infty} &= \alpha_{2,LS}\Big|_{M_\alpha \to \infty} = \alpha_{2,opt} \end{aligned} \tag{7.15}$$

7.2.2 Estimating EC Coefficients β_1 and β_2

Like shown in Subsection 7.1.2 in (7.11) the optimum EC coefficients are defined by $\mathbf{B}_{opt} = \mathbf{K}_m^{-1}\mathbf{K}_d^{-1}$. Thus to estimate this product using again LS model fitting, the setup depicted in Fig.7.3 is proposed here. In this set up, S_3 is closed while S_1 and S_2 are open. A test signal, $v_{in}(n)$, is injected into the modulator branch of EC circuit. The signal which is used for the transmission can be equally well used as the test signal here. The test signal is then downconverted to the baseband and is digitized using IQD and ADC, respectively. The relation between the input and output test signals is then

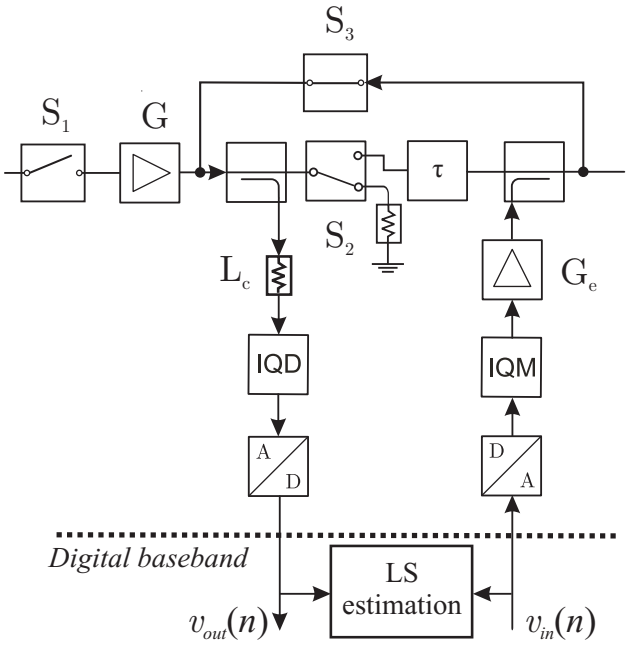

Figure 7.3: Estimating β_1 and β_2 in calibration stage.

given by

$$v_{out}(n) = \sqrt{g_e l_c}\Big(\quad (k_{d,1}k_{m,1} + k_{d,2}k^*_{m,2})v_{in}(n) + (k_{d,1}k_{m,2} + k_{d,2}k^*_{m,1})v^*_{in}(n)\Big) \tag{7.16}$$

Thereafter, M_β samples of the input and the output test signals are stored in $\mathbf{v}_{in} = [v_{in}(1), v_{in}(2), ..., v_{in}(M_\beta)]^T$ and $\mathbf{v}_{out} = [v_{out}(1), v_{out}(2), ..., v_{out}(M_\beta)]^T$, respectively. Finally, the matrices $\mathbf{V}_{in} = [\mathbf{v}_{in}\ \mathbf{v}^*_{in}]$ and $\mathbf{V}_{out} = [\mathbf{v}_{out}\ \mathbf{v}^*_{out}]$ are formed. Including the measurement noise term $\mathbf{V}_\gamma$, the matrix $\mathbf{V}_{out}$ can now be written in terms of $\mathbf{V}_{in}$ as

$$\mathbf{V}_{out} = \mathbf{V}_{in}(\mathbf{K}_d\mathbf{K}_m)^T + \mathbf{V}_\gamma \tag{7.17}$$

and the estimator for EC coefficients yields then

$$\mathbf{B}_{LS,\gamma} = (\mathbf{V}^\dagger_{out}\mathbf{V}_{in})^T = \left(\left(\mathbf{V}_{in}\left(\mathbf{K}_d\mathbf{K}_m\right)^T + \mathbf{V}_\gamma\right)^\dagger \mathbf{V}_{in}\right)^T \tag{7.18}$$

The detailed analysis in [P2] reveals that this estimator doesn't converge to the desired value even when $M_\beta \to \infty$. The underlying cause of this performance degradation is that the measurement noise in this estimator creates error in $\mathbf{V}_{out}$ as this matrix is formed from the samples of $v_{out}(n)$. Therefore, the problem at hand is different from typical LS where the errors

are considered only in the observed vector or in our case $\mathbf{V}_{in}$. These types of LS problems, known as errors-in-variables or Data Least-Squares (DLS), have been addressed widely in the literature in other applications [95, 96]. Here, the induced large sample coefficient estimation errors are defined as

$$\begin{aligned}\epsilon_{\beta,1}^{\infty} &= \beta_{1,LS}\Big|_{M_\beta\to\infty} - \beta_{1,opt} \\ \epsilon_{\beta,2}^{\infty} &= \beta_{2,LS}\Big|_{M_\beta\to\infty} - \beta_{2,opt}\end{aligned} \tag{7.19}$$

These errors are direct functions of the optimum EC coefficients, IQD and IQM I/Q imbalance coefficients as well as the signal-to-measurement-noise ratio. Closed form expressions for $\epsilon_{\beta,1}^{\infty}$ and $\epsilon_{\beta,2}^{\infty}$ are presented in the following [P2].

$$\begin{aligned}\mathbf{\Sigma}_B^{\infty} = &\left(\frac{\det\left((\mathbf{K}_d\mathbf{K}_m)^*(\mathbf{K}_d\mathbf{K}_m)^T\right)}{\det\left((\mathbf{K}_d\mathbf{K}_m)^*(\mathbf{K}_d\mathbf{K}_m)^T + \mathbf{\Upsilon}_{SNR,in}^{-1}\right)} - 1\right)\mathbf{B}_{opt} \\ &+ \frac{(\mathbf{K}_d\mathbf{K}_m)^H\mathbf{\Upsilon}_{SNR,in}^{-1}}{\det\left((\mathbf{K}_d\mathbf{K}_m)^*(\mathbf{K}_d\mathbf{K}_m)^T + \mathbf{\Upsilon}_{SNR,in}^{-1}\right)}\end{aligned} \tag{7.20}$$

where

$$\mathbf{\Sigma}_B^{\infty} = \begin{bmatrix} \epsilon_{\beta,1}^{\infty} & \epsilon_{\beta,2}^{\infty} \\ (\epsilon_{\beta,2}^{\infty})^* & (\epsilon_{\beta,1}^{\infty})^* \end{bmatrix}, \qquad \mathbf{\Upsilon}_{SNR,in} = \begin{bmatrix} \frac{p_{in}}{p_\gamma} & 0 \\ 0 & \frac{p_{in}}{p_\gamma} \end{bmatrix}$$

Here, p_{in} and p_γ are the powers of the input test signal and measurement noise,respectively.

7.3 DSP-FF Linearization Performance Analysis

The main function of DSP-FF is to mitigate the IMD components generated by the core PA. Hence, the ratio between the power of IMD distortion component at the core PA output and DSP-FF output is a natural measure for the performance of DSP-FF. We refer to this measure as intermodulation attenuation ratio (IMDA_r). The detail analysis in [P2] shows that under circularity assumption on the IMD term, i.e. $\mathbb{E}[v_d^2(n)] = 0$, and for $M_\beta \to \infty$ the IMDA_r reads

$$\begin{aligned}\text{IMDA}_r\big|_{M_\beta\to\infty} &= \text{IMDA}_r^{\infty} = \frac{p_d}{p_{d,o}} \\ &= \frac{1/g_e l_c}{\left|k_{m,1}k_{d,1}\epsilon_{\beta,1}^{\infty} + k_{m,1}k_{d,2}(\epsilon_{\beta,2}^{\infty})^*\right|^2 + \left|k_{m,2}^* k_{d,1}\epsilon_{\beta,2}^{\infty} + k_{m,2}^* k_{d,2}(\epsilon_{\beta,1}^{\infty})^*\right|^2}\end{aligned} \tag{7.21}$$

where p_d and $p_{d,o}$ are the IMD distortion powers at the core PA and DSP-FF output respectively. It is interesting to note here that IMDA_r^{∞} is independent of the error in the SC coefficients. Moreover, as it is already mentioned in 7.2.2, closed form expression for $\epsilon_{\beta,1}^{\infty}$ and $\epsilon_{\beta,2}^{\infty}$ and their conjugate are available in (7.20). Therefore, for given DSP-FF circuit parameters - g_e, l_c,$k_{d,1}$,$k_{d,2}$,$k_{m,1}$ and $k_{m,2}$ - and signal-to-measurement noise ratio, the IMDA_r^{∞} is analytically predictable using (7.21).

Although IMDA_r is representative for the main function of DSP-FF,i.e. IMD distortion mitigation, it can not alone paint a complete picture for overall performance of this linearizer. Nevertheless, a large IMDA_r always indicates that the IMD distortion components at the DSP-FF output is properly mitigated. However, large IMDA_r may also be achieved by merely implementing input/output *power back-off* which defeats the very idea of implementing the DSP-FF and results in poor overall power efficiency [40]. Therefore, a measure representing the relation between the input and output power of the DSP-FF, hand in hand with IMDA_r, provides complete insight into DSP-FF performance. Such a measure is defined here as the gain of the DSP-FF for the desired signal. Ideally, the DSP-FF gain should be equal to the desired signal gain provided by the core PA. However, any error in the estimation of DSP-FF circuit coefficients, especially the SC circuit coefficients, degrade the desired signal gain. Fortunately, as the large sample analysis of the SC circuit estimator shows in (7.15), $\alpha_{1,LS}^{\infty} = \alpha_{1,opt}$ and $\alpha_{2,LS}^{\infty} = \alpha_{2,opt}$. Therefore, for sufficiently large number of samples used in the estimation of SC circuit coefficients the DSP-FF and the core PA desired signal gains are equal. For more detailed analysis of the effects of SC and EC coefficient errors on the DSP-FF gain please refer to [P2].

7.3.1 Operation and Performance Under Core PA with Memory

The above analysis on the operation of DSP-FF and the performance of the EC and SC coefficients estimators can be extended to the case where the core PA exhibits memory. The detailed treatments of these topics are provided in [P2]. Here, we provide only the essential conclusions and outcomes of the analysis in [P2]. Firstly it is shown in [P2] that the memory characteristics of the core doesn't have any effect on the optimum coefficients of the EC circuit and the EC optimum coefficients in case of the core PA with memory are identical to the memoryless case. Moreover, the analysis presented in [P2] shows the errors in estimation of the EC coefficients are independent of the core PA memory and in both memory and memoryless case can be expressed with (7.20).

The IMDA_r^{∞} for DSP-FF with the core PA which is modeled by WH

behavioral model (Fig. 5.5(c)) reads [P2]

$$\mathrm{IMDA}_r^{wh,\infty} = \frac{p_d^{wh}}{p_{d,o}^{wh,\infty}} \tag{7.22}$$

The superscript *wh* denotes the signal values and variables in DSP-FF analysis for the case of the PA with Wiener-Hammerstein behavioral model. The power of the IMD terms at the WH PA and DSP-FF output are denoted here by p_d^{wh} and $p_{d,o}^{wh,\infty}$, respectively. All in all, with a circularity assumption for the IMD term, i.e. $E[v_d(n)\, v_d(n+l)] = 0 \;\forall\; l$, and some straight forward math it is possible to show that $\mathrm{IMDA}_r^{wh,\infty} = \mathrm{IMDA}_r^{\infty}$ [P2]. Here, one should pay especial attention to the fact that $\mathrm{IMDA}_r^{wh,\infty}$ represents the amount of reduction in the power of the IMD component *and* its delayed (filtered) versions.

The SC circuit analysis in the case of the core with memory, where the behavioral model of the PA is again assumed to be WH, shows that the optimum values for SC circuit coefficients are in the following form [P2]

$$\mathbf{A}_{opt}^{wh} = \mathbf{K}_d \mathbf{\Lambda}_G \mathcal{H}_T^d \tag{7.23}$$

where $\mathcal{H}_T^d$ is defined as

$$\mathcal{H}_T^d = \begin{bmatrix} h_T(d) & 0 \\ 0 & h_T^*(d) \end{bmatrix}$$

Here, $h_T(n) = h_1(n) * h_2(n)$ where $h_1(n)$ and $h_2(n)$ are the finite impulse response (FIR) pre- and post-filter impulse responses of the WH model, respectively, d is the delay of the overall WH structure in samples and $*$ is the convolution operator. The same setup as the memoryless case can be used to estimate the optimum SC coefficients. In particular case of WH core PA the LS estimator for SC coefficients reads [P2]

$$\mathbf{A}_{LS}^{wh} = \left(\mathbf{V}_{m,L_T-d}^{\dagger}\, \mathbf{V}_{a,iq} \right)^T \tag{7.24}$$

where $\mathbf{V}_{m,L_T-d} = [\mathbf{v}_{m,L_T-d} \mathbf{v}_{m,L_T-d}^*]$ where the vector $\mathbf{v}_{m,L_T-d} = [v_m(L_T - d + 1), \ldots, v_m(L_T + M_\alpha - d)]^T$ and L_T is the number of taps in $h_T(n)$. It is demonstrated through analysis in [P2] that SC coefficients estimator $\mathbf{A}_{LS}^{wh}$ approaches to its optimum values as the number of samples which is used in the estimation grows sufficiently large, i.e. $\mathbf{A}_{LS}^{wh,\infty} = \mathbf{A}_{opt}^{wh}$, even in presence of measurement noise. As the result, similar to the memoryless case, the overall gain of the WH PA is preserved by DSP-FF linearizer [P2].

7.4 Simulation and Numerical Examples

The first set of experiments is performed to verify and demonstrate the analytical results on the errors in the estimation of β_1 and β_2 in the presence of measurement noise which is stated in Subsection 7.2.2. It follows then by another experiment verifying the analytical expression for IMDA_r^{∞} in (7.21). The second batch of experiments verifies the analytical results on the SC circuit coefficients estimation error and their effect on the DSP-FF desired signal gain which was presented in Section 7.3. The signals which are used through out these experiments are OFDM signals with 1024 subcarriers of which 300 are active around the center-frequency except for the DC bin. The memoryless core PA which is used in the simulations is modeled by a baseband polynomial [79] of the form

$$y(n) = \sum_{l=1}^{L} c_l \; x(n)|x(n)|^{l-1} \tag{7.25}$$

The polynomial model includes only odd order components i.e. $c_l = 0$ when l is even. The coefficients values are taken from a class AB power amplifier model [79]

$$\begin{aligned} c_1 &= 14.974 + j0.0519 \\ c_3 &= -27.0954 + j4.9680 \\ c_5 &= 21.3936 + j0.4305 \end{aligned} \tag{7.26}$$

A WH is used in the simulations involving a core PA with memory. The static part of the WH model in this simulations is a SSPA model [77] with $p = 2$ and the clipping level of $A_0 = 1$. The pre- and post-filter in this WH model are complex-valued infinite impulse response (IIR) filters of the following form

$$\begin{aligned} H_1(z) &= \frac{(1 + 0.2j) + (0.3 + 0.1j)z^{-1}}{(1 + 0.1j) + (-0.2 + 0.05j)z^{-1}} \\ H_2(z) &= \frac{(1 + 0.2j) + (0.3 + 0.1j)z^{-2}}{(1 + 0.1j) + (0.2 + 0.05j)z^{-2}} \end{aligned} \tag{7.27}$$

Finally, the imbalance values for IQD and IQM are 5%, 6°, 6% and 7°, respectively, which represent a realistic example scenario.

7.4.1 EC Circuit Coefficients Error and IMDA_r: Memoryless Core PA

The curves in Fig. 7.4 represent the errors in the estimation of EC circuit coefficients. The simulated curves are obtained for different sample numbers

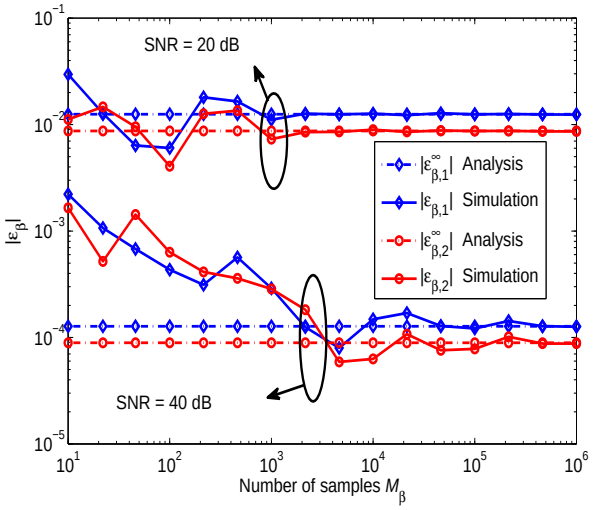

Figure 7.4: Computer simulated $|\epsilon_{\beta,1}|$ and $|\epsilon_{\beta,2}|$ vs. sample size M_β, as well as the analytical large sample quantities $|\epsilon^{\infty}_{\beta,1}|$ and $|\epsilon^{\infty}_{\beta,2}|$ for two different signal-to-measurement-noise ratios 20dB and 40dB. The solid lines are from the simulation and the analytical dot dashed lines are the errors predicted by the large sample analysis (7.20).

which is used in LS estimation and for different signal-to-measurement-noise ratios. These errors are compared to the closed form expression for $|\epsilon^{\infty}_{\beta,1}|$ and $|\epsilon^{\infty}_{\beta,2}|$ in (7.20). The simulation curves clearly match the analytical predictions as M_β gets sufficiently large.

The next computer simulated experiment is to verify the accuracy of the expression for IMDA$_r$ in (7.21). First, IMDA$_r^{\infty}$ is obtained for the different number of samples used in the estimation of β_1 and β_2, and for the signal-to-measurement-noise ratios of 20 and 40 dB. The core PA operating point in this experiment is set to 5 dB input back-off (IBO) from 1 dB compression point. Thereafter, the IMDA$_r^{\infty}$ in (7.21) is calculated for the corresponding signal-to-measurement-noise ratios. The results presented in Fig. 7.5 show that using the closed-form expression in (7.21), it is possible to predict the large sample performance of DSP-FF with great accuracy for practical ranges of signal-to-measurement noise ratios.

7.4.2 DSP-FF Desired Signal Gain

Another set of experiments is designed aimed to verify and demonstrate the large sample performance of SC circuit coefficient estimator and the effect of the estimation error in SC and EC coefficients on the desired signal gain at DSP-FF output which were stated in the Subsection 7.2.1 and Section 7.3. The simulation setup remains otherwise as it is described in the preceding

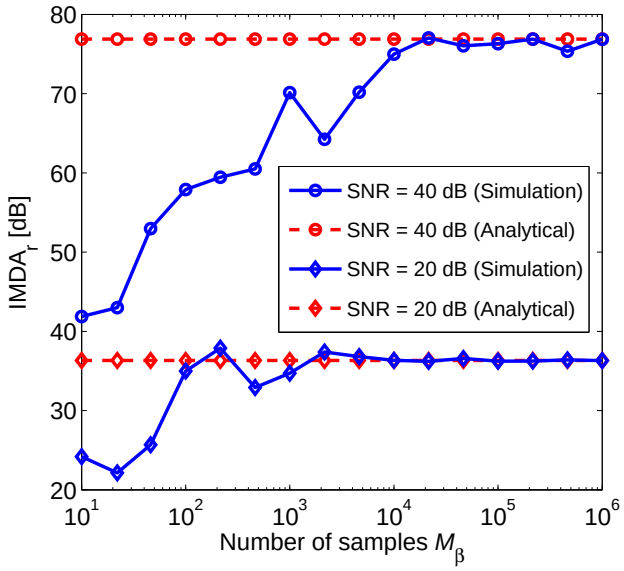

Figure 7.5: IMDA_r vs. number of samples M_β used in the LS estimator for β_1 and β_2. The experiment is performed for 20dB and 40dB signal-to-measurement-noise ratios. The operation point of the core PA is 5dB IBO from 1dB compression point. The solid lines are the results of computer simulations and the dashed lines are analytical results obtained from (7.21).

subsection. In the first experiment, the estimation of SC circuit coefficients is performed as described in Subsection 7.2.1. The estimation of α_1 and α_2 is performed under two different signal-to-measurement noise ratios, 20 dB and 40 dB. The core PA is operated at 5 dB IBO from its 1 dB compression point. The number of samples which are used to estimate SC coefficients is varied from 10 to 10^6. The results of this experiment in Fig. 7.6 show that the errors in $\alpha_{1,LS}$ and $\alpha_{2,LS}$ are significantly reduced as the number of samples reaches 10^3 and practically vanishes when the number of samples approaches 10^6. This experiment also demonstrates that the measurement noise does not affect the performance of the estimator. This result is again clearly in line with the large sample analysis of the EC circuit estimator presented in Subsection 7.2.1. In the second experiment, the desired signal gain of the DSP-FF is simulated. The core PA is operated at 5, 8 and 10 dB IBO from 1 dB compression point. The number of samples used in the estimation of the SC coefficients is varied from 10 to 10^6. The estimation of α_1 and α_2 is performed for two different values of signal-to-measurement-noise ratios, 20 dB and 40 dB. The results of this experiments presented in Fig. 7.7 depict the desired signal gain of the DSP-FF and the core PA against each other. It is observed from this figure that the DSP-FF gain for desired signal matches the core PA desired signal gain when M_α is sufficiently large, independent

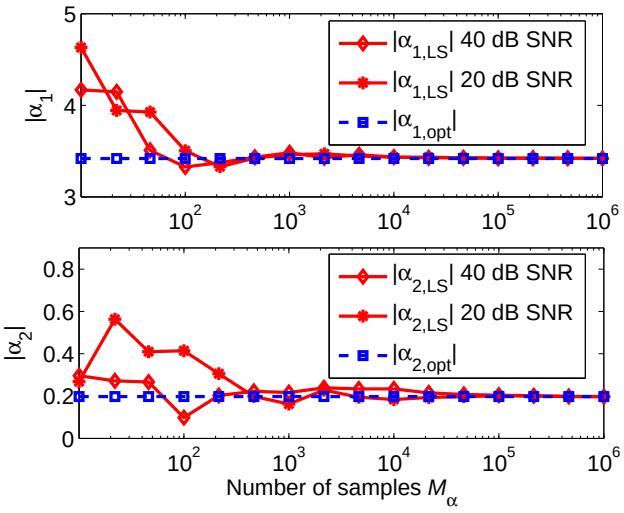

Figure 7.6: Computer simulated $|\alpha_{1,LS}|$ and $|\alpha_{2,LS}|$ against $|\alpha_{1,opt}|$ and $|\alpha_{2,opt}|$ for different number of samples M_α used in the SC circuit LS estimator. The signal-to-measurement-noise ratios are 20dB and 40dB and the operation point of the core PA is 5dB IBO from 1dB compression point.

of measurement noise level. This is again in line with the earlier analytical results. One should also note that according to these results, the effect of errors in the estimation of $\beta_{1,LS}$ and $\beta_{2,LS}$ is insignificant as the number of samples to estimate EC circuit coefficients is here only 100 and the signal-to-measurement-noise ratio is set to 20 dB which yields high estimation errors in the order of 10^{-2} in the EC circuit coefficients (Fig.7.4).

7.4.3 IMDA$_r$ and DSP-FF Overall Gain: WH PA

This set of simulated experiments is designed to demonstrates IMDA$_r$ and overall gain performance of the DSP-FF when the core PA exhibits memory effect. The setup for the experiment is identical to the previously described simulations with a difference that the core PA is the WH model which is described at the beginning of this section. The input signal power is set in such a way that the SSPA model is driven at 3 dB compression point to ensure extreme nonlinear behavior. The outcomes of the experiments presented in Fig. 7.8 and Fig. 7.9 verify that the closed-from expressions of (7.20) and (7.21) are equally valid for a core PA with memory. This is well in line with the results already stated in Subsection 7.3.1. The power spectrum of the PA output and the corresponding DSP-FF output for one realization of the above described experiment is depicted in Fig. 7.10 for illustration purposes. The LS coefficients are estimated under 40dB signal-to-measurement-noise ratio. The number of samples used in LS estimations

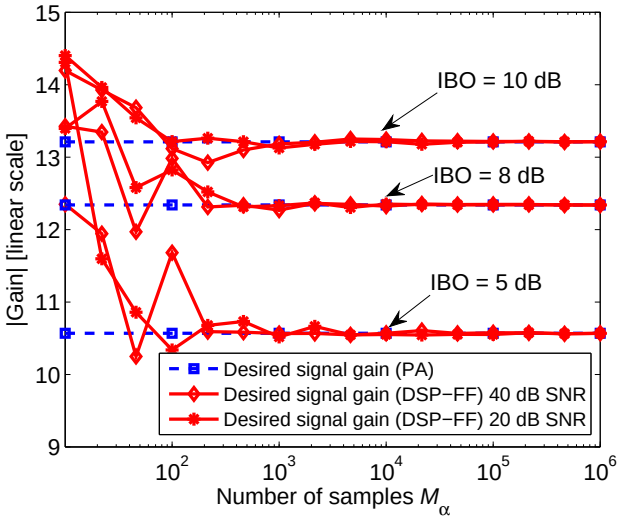

Figure 7.7: Desired signal gain of the core PA and the overall DSP-FF structure vs. number of samples M_α used in the SC circuit LS estimator. The results are depicted for 5dB, 8dB and 10dB IBOs from 1dB compression point of the core PA. The signal-to-measurement-noise ratios in estimation of α_1 and α_2 are 20dB (star) and 40dB (diamond). The estimation of β_1 and β_2 is always performed under signal-to-noise ratio of 20dB with $M_\beta = 100$ samples.

are 10^5 and 100 for EC and SC circuits, respectively. The comparison of the core PA output power spectrum and the linearized one shows that the DSP-FF in use effectively mitigates the IMD components. One should also note that due to EC circuit coefficients estimation inaccuracies, stemming from measurement noise, the IMD components are not entirely eliminated. Thus, since the core PA exhibits memory, also the remaining IMD components contain memory, which in turn manifest itself as the residual memory effects visible in Fig. 7.10. As predicted with analysis, Fig. 7.11 confirms that the large sample estimation of SC circuit coefficients indeed converge to their optimum values in case of a core PA with memory. The preservation of the core PA desired signal gain for a memory PA, which is again predicted with analysis, is also depicted in Fig. 7.12.

7.4.4 Laboratory Measurement Experiment

A measurement setup is also devised to demonstrate the performance of the DSP-FF with real-world electronics. A PA is driven, first, close to its maximum output power rating which creates high levels of spectral regrowth at the core PA output. Thereafter, using DSP-FF, the attenuation of the spectral regrowth is demonstrated.

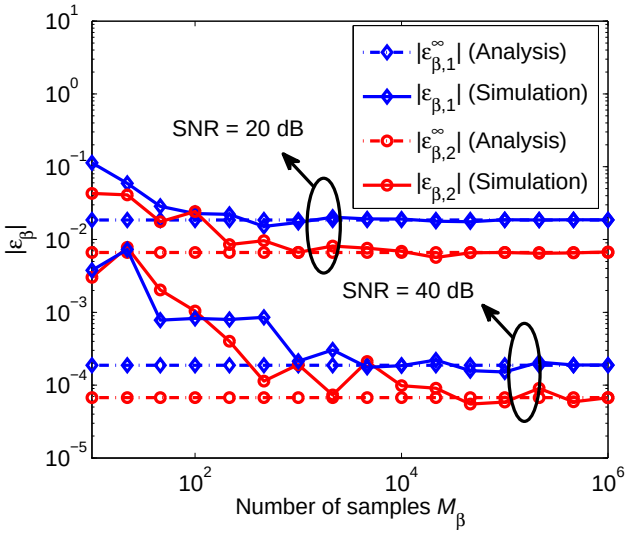

Figure 7.8: Computer simulated $|\epsilon_{\beta,1}|$ and $|\epsilon_{\beta,2}|$ vs. sample size M_β, as well as the analytical large sample quantities $|\epsilon^\infty_{\beta,1}|$ and $|\epsilon^\infty_{\beta,2}|$ for two different signal-to-measurement-noise ratios 20dB and 40dB. The core PA is WH. The solid lines are from the simulation and the analytical dot dashed lines are the errors predicted by the large sample analysis (7.20).

The setup which is designed to estimate SC circuit coefficients is based on Fig.7.2. The vector $\mathbf{v}_m$ is generated from $v_m(n)$ which is a 4.5 MHz LTE [2] uplink signal sampled at 7.68 MHz. This vector is generated first in MATLAB and loaded to a vector signal generator (SMJ from Rohde & Schwartz). The vector signal generator produces the continuous-time RF signal $v_{m,RF}(t)$ at 1 GHz center frequency and delivers that to the core PA which is built around the gain block AG503-86 from Watkins Johnson (WJ) which is designed as a class B amplifier. The maximum nominal output power of this particular PA is 18 dBm at 1GHz. In this experiment, the PA is operated at 1 dB output compression point which yields 16 dBm output power. Thereafter, $v_{a,RF}(t)$ is attenuated and is fed to a vector analyser (FSG from Rohde & Schwartz), which is utilized as IQD. The output of the vector analyser, $v_{a,iq}(n)$, is imported to MATLAB as $\mathbf{v}_{a,iq}$. Finally, the matrices $\mathbf{V}_m$ and $\mathbf{V}_{a,iq}$ are constructed and the $\mathbf{A}_{LS,\gamma}$ is estimated using (7.14). To estimate EC circuit coefficients, the measurement setup is based on the structure explained in Fig.7.3. The vector $\mathbf{v}_{in}$ is generated in MATLAB from a 4.5 MHz LTE uplink signal sampled at 7.68 MHz. It is, then, loaded into a vector signal generator, which is utilized as IQM. The signal generator upconverts the signal to 1 GHz and delivers it to the error amplifier G_e. A highly linear amplifier (AH-103 from WJ) is used as G_e. The G_e output, then, is attenuated and loaded into the vector signal analyser, utilized as

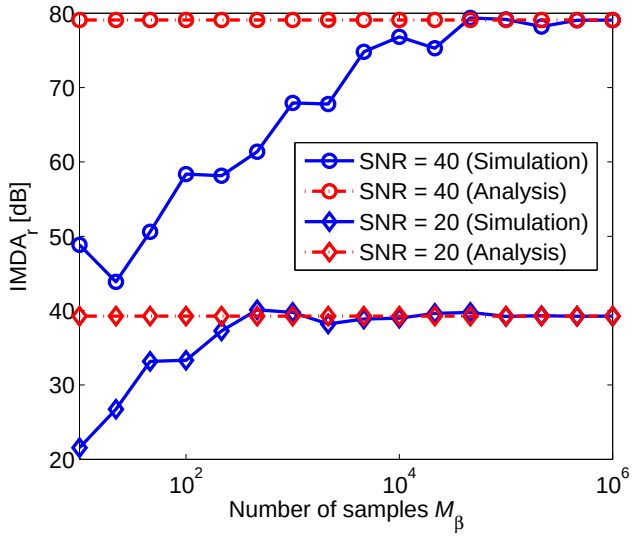

Figure 7.9: IMDA_r vs. number of samples M_β used in the LS estimator for β_1 and β_2 for WH core PA. The experiment is performed for 20dB and 40dB signal-to-measurement-noise ratios. The solid lines are the results of computer simulations and the dashed lines are analytical results obtained from (7.21).

IQD. The vector $\mathbf{v}_{out}$ is configured in MATLAB using the samples of $v_{out}(n)$, which is the vector analyser output. Next, the matrices $\mathbf{V}_{in}$ and $\mathbf{V}_{out}$ are constructed from the vectors $\mathbf{v}_{in}$ and $\mathbf{v}_{out}$, respectively. Finally, $\mathbf{B}_{LS,\gamma}$ is estimated using (7.18).

The final step of the experiment consists of two stages: first generating the baseband error signal and second subtracting the generated error signal from the core PA output.

For the first stage, another realization of the vector $\mathbf{v}_m$ is generated in MATLAB and loaded into the vector signal generator. The vector signal generator upconverts the signal to 1 GHz, then the upconverted signal is fed to the core PA. Thereafter the core PA output is attenuated, downconverted and loaded to MATLAB. Now, the baseband error vector, $\mathbf{v}_e$, is estimated from (7.4). The error vector is processed in Matlab by the estimated EC circuit coefficients and is then upconverted to 1 GHz using the vector signal generator. The upconverted error signal is amplified by G_e and finally subtracted from the core PA output. The resulting signal is DSP-FF output, $v_{o,RF}(t)$. A variable RF delay is utilized after the core PA to ensure that the subtraction at the core PA output is performed with acceptable delay match. The core PA input, the core PA output and the resulting DSP-FF output are presented in Fig. 7.13. In this case, the number of samples which is used for the estimation of SC and EC circuit coefficients is 10^4. The DSP-FF in

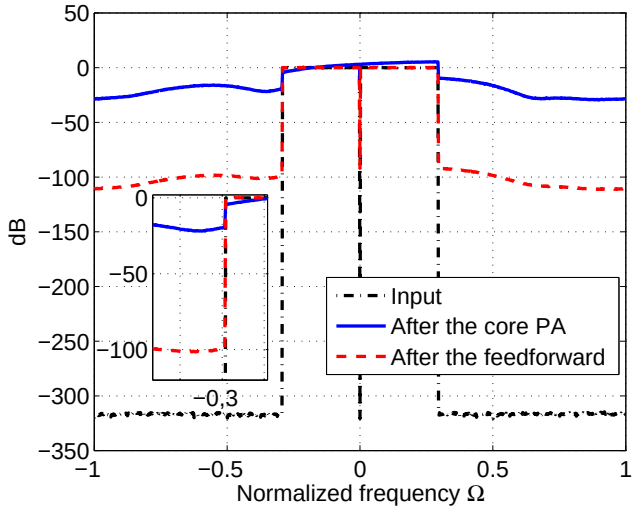

Figure 7.10: The spectrum of the input signal (dot-dashed line), core PA output (solid line) and DSP-FF output (dashed line) for the WH core PA. The operating point for the core PA is at 3 dB compression point. Signal-to-measurement noise ratio is 40 dB and $M_\alpha = 100$, $M_\beta = 10^5$. The input signal is OFDM with 1024 subcarriers of which 300 are active. The subcarriers around DC are inactive. The FFT has the same number of bins as the IFFT in the transmitter.

this case improves the ACLR by 9 dB and 10 dB for the lower and the upper adjacent channels, respectively. The ACLR is defined here as the power ratio of the transmitting and adjacent channels of 5 MHz.

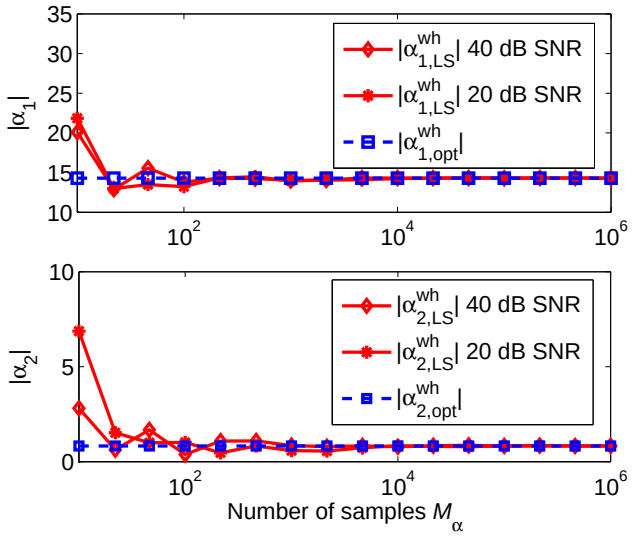

Figure 7.11: Computer simulated $|\alpha_{1,LS}^{wh}|$ and $|\alpha_{2,LS}^{wh}|$ against $|\alpha_{1,opt}^{wh}|$ and $|\alpha_{2,opt}^{wh}|$ for different number of samples M_α used in the SC circuit LS estimator for WH core PA. The signal-to-measurement-noise ratios are 20dB and 40dB and the operating point of the core PA is 0dB IBO from 3dB compression point.

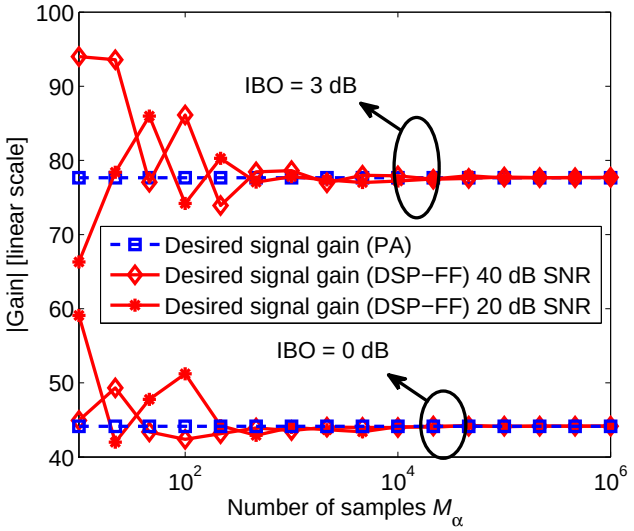

Figure 7.12: Desired signal gain of the core PA and the overall DSP-FF structure vs. number of samples M_α used in the SC circuit LS estimator and for WH core PA. The results are depicted for 0dB and 3 dB IBOs from 3dB compression points of the core PA. The signal-to-measurement-noise ratios in estimation of α_1 and α_2 are 20dB (star) and 40dB (diamond). The estimation of β_1 and β_2 is always performed under signal-to-noise ratio of 20dB with M_β = 100 samples.

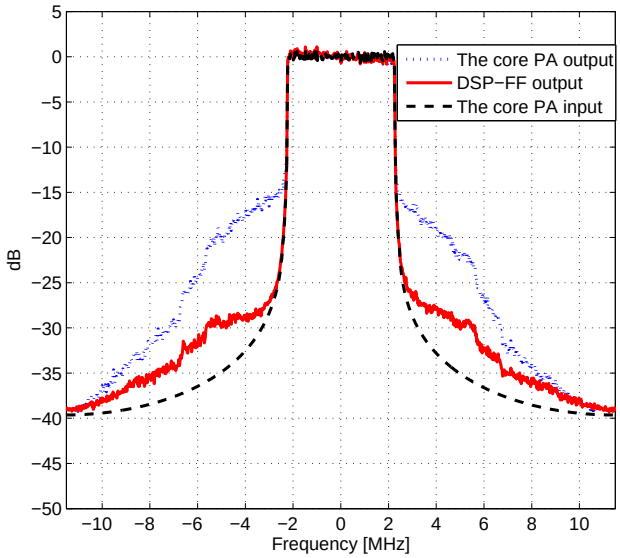

Figure 7.13: Measured normalized power spectrum of the core PA input, the core PA output and DSP-FF output. An LTE uplink signal with 4.5 MHz bandwidth is used in this laboratory measurement. The solid line represents the power spectrum of the linearized signal. The dotted line presents the core PA output and the dashed line is the core PA input. The number of samples which is used to estimate SC and EC circuit coefficients is 10^4. The x-axis represents the frequencies around 1 GHz center frequency.

CHAPTER 8

CONCLUSIONS

Dirty-RF concept, i.e., mixed signal processing/DSP algorithms to compensate for the front-end non-ideality effects, plays a crucial role in shaping the future of radio transceiver design. Deploying dirty-RF-based algorithms enables transceiver designers to design power efficient, wideband, portable and yet affordable radio devices through the use of less-than-perfect front-end components. Naturally, designing algorithms based on dirty-RF concept requires familiarity with the design strategies and algorithms which are generally used on either side of the ADC. In addition, proper understanding of certain non-ideality effects is an essential requirement for devising an effective strategy to mitigate those effects. That was the main ideology shaping up the structure of this manuscript, i.e. first to understand the effects of nonlinearity in radio transceivers, as the non-ideality which was the focus of this thesis, and then to propose proper dirty-RF-inspired DSP solutions to mitigate the nonlinearity effects in radio transceivers.

In the early parts of this manuscript the effects of nonlinearity in the context of DCR was studied. In particular the effects of nonlinear LNA and nonlinearity in I/Q path of the DCR was analyzed. As the result the profile of spurious frequency components for both types of nonlinearity was derived. As one of the contributions of this manuscript, it was shown that the nonlinearity in the I/Q branches of the DCR downconversion path generate rather different spurious frequency profile compared to LNA. This was presented in general through formal analysis of real passband nonlinearity (for LNA) and I/Q passband nonlinearity (for the I/Q paths of DCR). Based on the derived interference profile a DSP-based adaptive interference cancellation (IC) method was proposed to mitigate the interfering components stemming from the combined effects of nonlinear LNA and nonlinear elements in I/Q branches. Laboratory measurement experiments using real world telecommunications signals and actual receiver front-end showed that the proposed

IC method significantly mitigates these interfering terms.

The dynamic DC-offset problem in multiple-front-end DCR was treated next in this manuscript. The dynamic DC-offset components, resulting from RF signal self-mixing hit the desired signal band and are particularly damaging when they are created from self-mixing of strong blockers. Here, the signal model for the dynamic DC-offset for multiple-front-end receiver was derived. Furthermore, DSP algorithm based on ICA was proposed to mitigate the effects of dynamic DC-offset interference in the multiple front-end DCR. Deploying this DSP method relaxes the requirement on the isolation levels between the mixing core ports and therefore less expensive mixers can be deployed in DCR. Simulation results comparing the proposed algorithm against a number of bench mark diversity algorithms showed the superior interference mitigation of this method in a wide range of SNR.

The combined nonlinearity analysis of all the nonlinear elements in DCR and possible compensation method for transmitter nonlinearity implemented in the receiver side and detailed analysis of the proposed algorithm in combination to other non-idealities in the receiver are among future topics. Moreover, analysis of the effects of non-idealities in general and nonlinearity in particular on the sensing algorithms and actual CR receivers are among the promising and exciting topics.

On the transmitter side the nonlinearity study was focused mostly on the major source of nonlinearity in the radio transmitters, i.e., the RF power amplifier (PA). The system-level modeling of PA, i.e., behavioral modeling, was explained. Thereafter, the linearity vs. power efficiency dilemma in the PA design was presented to motivate the linearization topic, and in particular feedforward linearizer, as a solution which strikes a balance between linearity and power efficiency in PA. The effects of the errors in the adjustments of feedforward linearizer coefficients on the performance of this linearizer were analyzed. A closed-form expression relating these errors and linearization performance of feedforward linearizer with memoryless core PA in terms of r-SIR, i.e., the improvement in the signal-to-interference ratio as the result of deploying a feedforward linearizer, was derived.

To improve the flexibility of the feedforward linearizer, a DSP-oriented implementation of feedforward linearizer was proposed in this thesis. In this implementation of the feedforward linearizer major parts of its principal functionality, i.e., generation of the error signal, is transferred to the DSP regime. In addition, block-based algorithms to estimate the EC and SC coefficients were proposed. These algorithms have the benefits of estimating EC and SC coefficients independently, i.e., the error in the estimation of one of the coefficients doesn't propagate to the other coefficient. The large sample analysis of the EC circuit coefficients estimator revealed that the presence of measurement noise limits the accuracy of the EC circuit coefficient estimator. A closed-form expression predicting the large-sample EC coefficient

estimation error was derived analytically. The error in the estimation of EC coefficients in turn affects the linearization performance of DSP-FF in terms of the attenuation of intermodulation distortion. This performance measure was described as IMDA_r, or the ratio between the IMD term power at the PA output and DSP-FF output. In addition, a closed-form expression describing IMDA_r in terms of DSP-FF parameters was derived analytically. The above analyses were also extended for the DSP-FF with a core PA exhibiting memory. Extensive computer simulation results were reported to verify and demonstrate the analytical results for both cases where the core PA exhibits memory and the memoryless case. Finally, a proof-of-concept measurement setup demonstrated the achieved spectral regrowth suppression by this structure.

Among the future directions on the feedforward linearizer studies, are designing an adaptive algorithm to track the changes in the SC and EC circuit parameters and implementing more advanced algorithms at the baseband process of DSP-FF to improve its performance and power efficiency. Moreover, it is possible to show that in case IQM and IQD exhibit *frequency dependent* I/Q imbalances, those effects can be also compensated using similar approach as presented in this manuscript. The only required modification is to replace the coefficients in EC and SC circuits widely-linear filters with multitap filters. The in-depth analysis of such structure as well as introducing proper method to estimate these filters are considered in future studies. In the greater scheme of nonlinearity studies in transmitters, studies on improving the performance of digital predistorters, as a promising linearizer structure, as well as analyzing and compensating the combined effect of all the non-idealities in the transmitter chain will have great academic and social impact in future.

CHAPTER 9

SUMMARY OF PUBLICATIONS AND AUTHOR'S CONTRIBUTIONS

In this chapter we briefly describe the contents of the original publications [P1]-[P6]. The contributions of the thesis author to each individual publication contents are also discussed.

9.1 Summary of Publications

In [P1] and [P4], the contributions of nonlinear analog front-end in generating inter/cross-modulations interference on top of the desired signal in the presence of multiple strong signals are analyzed. In this analysis nonlinearities in LNA as well as nonlinear elements in the I/Q branches of a DCR receiver are considered, presenting the input/output relation of these elements using a basic polynomial model. The result of the derivations shows a distinct feature for the interference profile generated by nonlinear LNA and I/Q nonlinear elements. Based on the derived interference profile a DSP-based adaptive interference cancellation method is proposed to mitigate the interfering components stemming from the combined effect of nonlinear LNA and nonlinear elements in I/Q branches. Laboratory measurement experiments using real world telecommunications signals and actual receiver front-end show that the proposed IC method significantly mitigates these interfering terms.

The issue of DCR with dynamic DC-offset in multiple-front-end receivers context is studied in [P3]. Dynamic DC-offset components are generated as the result of RF signal self-mixing from insufficient isolation between the RF and LO port of the mixing core. Furthermore, DSP algorithm based on ICA is proposed in [P3] to mitigate the effects of dynamic DC-offset component interference in multiple front-end DCR. Simulation results comparing the

proposed algorithm against a number of bench mark diversity algorithms such as zero-forcing ZF and MRC shows the superior interference mitigation capability of this method in a wide range of SNR.

The effects of the errors in the adjustments of feedforward linearizer coefficients on the linearization performance are analyzed in [P5]. A closed-form expression relating these errors and linearization performance of feedforward linearizer with memoryless core PA in terms of r-SIR, i.e., the improvement in the signal-to-interference ratio as the result of deploying feedforward linearizer, is derived. It is shown analytically that the same expression for r-SIR can be equally used for the case where the core PA in feedforward linearizer exhibits memory effects.

One major drawback of the feedforward linearizer is that it is typically implemented entirely in the RF regime using bulky and rigid components. Therefore to improve upon this aspect of feedforward a DSP-oriented implementation of feedforward linearizer (DSP-FF) is initially proposed in [P6]. Least-square-based estimation algorithms for calibrating SC and EC circuits are also proposed in [P6]. These algorithms have the benefits of estimating EC and SC coefficients independently, i.e., the error in the estimation of one of the coefficients doesn't propagate to the other coefficient. Thorough performance analysis of DSP-FF as well as implementation aspects of DSP-FF are presented in [P2]. Modified and improved estimation methods for SC and EC circuits, in comparinson with [P6] are introduced in [P2]. The large sample performance of SC and EC coefficients estimators in the case of a memoryless core PA under and in the presence of measurement noise are analyzed. As a result a closed-form expression predicting the EC coefficient estimation floor performance is derived analytically. Moreover, a performance measure for DSP-FF, i.e., IMDA_r or the ratio between the IMD term power at the PA output and DSP-FF output is introduced in [P2]. A closed-form expression describing IMDA_r in terms of DSP-FF components parameters is presented in [P2]. The above analyses are also extended for the DSP-FF with a core PA with memory. Extensive computer simulation results are reported to verify the analytical results for both cases where the core PA exhibits memory and the memoryless case. Finally, a proof-of-concept measurement setup demonstrates the achieved interference mitigation by this structure.

9.2 Author's Contributions to the Publications

The entire research work reported in publications [P1]-[P6] was carried out in the Department of Communications Engineering (DCE), Tampere University of Technology (TUT), Finland, Tampere. The idea for the adaptive

interference cancellation method resulting in publications [P1] and [P4] was initially proposed by the supervisor, Prof. Mikko Valkama, and Prof. Markku Renfors. In [P4], the author performed the analysis leading to the new understanding of the interference profile of the I/Q bandpass nonlinearity. The simulation and measurement experiments as well as the preparation of the manuscript were performed by the author. The supervisor guided the author through all the mentioned tasks and also contributed significantly to the final appearance of the manuscript. In [P1], the author performed the bulk of the analytical derivations, simulation experiments and laboratory measurement. Incorporating memory effect in the interference cancellation structure was proposed and implemented by the author. The final manuscript was prepared in collaboration with the supervisor, the author of the thesis contributed in writing of analytical and results sections. The application of ICA in mitigating dynamic DC-offset reported in [P3], was proposed by the author. The signal modeling, design of the simulation experiments and writing the manuscript was solely performed by the author. The sensitivity analysis of feedforward linearizer leading to the publication [P5] was proposed by the author. The author was the main contributor to this publication. The DSP-oriented implementation of feedforward linearizer was the result of collaboration between DCE and Institute of Communications and Information Engineering, University of Linz, Austria and Danube Integrated Circuits Engineering (DICE). The final structure for DSP-FF was the result of close collaborations between the author of the thesis and M.Sc. Sascha Burglechner from University of Linz. In [P6] the signal modeling, estimation algorithm design and simulation experiments are designed by the author. The author also contributed to the writing of the final manuscript particularly bulk of the theoretical section. In publication [P2] the author was the main contributor. In all the analytical results, simulation experiments and in preparation of the manuscript the author of this thesis was the main contributor. However, the measurement experiment was performed in collaboration with the second author. All in all, prof. Mikko Valkama made essential contributions in all the publications through insightful comments and useful suggestions.

9.2.1 Other Publications by The Author

In addition to the publications which are included in this manuscript the author contributed to a number of other articles closely related to the topic of the thesis. These articles are not included in the manuscript, however they are cited in the reference section as [33, 34, 47, 97, 98].

APPENDIX

A.1 Real Bandpass Nonlinearity

These examples demonstrate the final IMD profile of bandpass nonlinear elements such as LNA exhibiting 2nd- and 3rd-order nonlinearity. Three bandpass signals at distinct frequencies ω_0, ω_1 and ω_2 are used as the nonlinear element input. The output spurious frequencies here are categorized to motivate the scenario in which a weak desired signal at ω_0 and two strong blockers at ω_1 and ω_2 are present at the nonlinearity input, i.e., $\mathbb{E}[|A_0(t)|^2] \ll \mathbb{E}[|A_1(t)|^2]$ and $\mathbb{E}[|A_0(t)|^2] \ll \mathbb{E}[|A_2(t)|^2]$. The signal $x_{RF}(t)$ containing three bandpass signals reads

$$\begin{aligned} x_{RF}(t) = {} & A_0(t)\cos(\omega_0 t + \phi_0(t)) + A_1(t)\cos(\omega_1 t + \phi_1(t)) \\ & + A_2(t)\cos(\omega_2 t + \phi_2(t)) \end{aligned} \tag{A.1}$$

Table A.1: IMD components for $a_1 x_{RF}(t) + a_2 x_{RF}^2(t)$

Original signal components
$+a_1 A_0(t)\cos\big(\omega_0 t + \phi_0(t)\big)$ $+a_1 A_1(t)\cos\big(\omega_1 t + \phi_1(t)\big)$ $+a_1 A_2(t)\cos\big(\omega_2 t + \phi_2(t)\big)$
Components around DC
$+\frac{a_2}{2}A_0^2(t) + \frac{a_2}{2}A_1^2(t) + \frac{a_2}{2}A_2^2(t)$

Components at 2-times original frequencies
$+a_2\frac{A_0^2(t)}{2}\cos(2\omega_0 t + 2\phi_0(t))$ $+a_2\frac{A_1^2(t)}{2}\cos(2\omega_1 t + 2\phi_1(t))$ $+a_2\frac{A_2^2(t)}{2}\cos(2\omega_2 t + 2\phi_2(t))$
Blocker's cross-modulations
$+a_2 A_1(t)A_2(t)\cos\big((\omega_1+\omega_2)t + \phi_1(t) + \phi_2(t)\big)$ $+a_2 A_1(t)A_2(t)\cos\big((\omega_1-\omega_2)t + \phi_1(t) - \phi_2(t)\big)$
Desired signal and one blocker cross-modulations
$+a_2 A_1(t)A_0(t)\cos\big((\omega_1+\omega_0)t + \phi_1(t) + \phi_0(t)\big)$ $+a_2 A_1(t)A_0(t)\cos\big((\omega_1-\omega_0)t + \phi_1(t) - \phi_0(t)\big)$ $+a_2 A_2(t)A_0(t)\cos\big((\omega_2+\omega_0)t + \phi_2(t) + \phi_0(t)\big)$ $+a_2 A_2(t)A_0(t)\cos\big((\omega_2-\omega_0)t + \phi_2(t) - \phi_0(t)\big)$

Table A.2: IMD components for $a_1 x_{RF}(t) + a_3 x_{RF}^3(t)$

Original signal components
$+a_1 A_0(t)\cos\big(\omega_0 t + \phi_0(t)\big)$ $+a_1 A_1(t)\cos\big(\omega_1 t + \phi_1(t)\big)$ $+a_1 A_2(t)\cos\big(\omega_2 t + \phi_2(t)\big)$
Self-distortion components
$+a_3\left(\frac{3A_0^3(t)}{4} + \frac{3A_1^2(t)A_0(t)}{2} + \frac{3A_2^2(t)A_0(t)}{2}\right)\cos(\omega_0 t + \phi_0(t))$ $+a_3\left(\frac{3A_1^3(t)}{4} + \frac{3A_2^2(t)A_1(t)}{2} + \frac{3A_0^2(t)A_1(t)}{2}\right)\cos(\omega_1 t + \phi_1(t))$ $+a_3\left(\frac{3A_2^3(t)}{4} + \frac{3A_1^2(t)A_2(t)}{2} + \frac{3A_0^2(t)A_2(t)}{2}\right)\cos(\omega_2 t + \phi_2(t))$
Components at 3-times original frequencies
$+a_3\frac{A_0^3(t)}{4}\cos(3\omega_0 t + 3\phi_0(t))$

$$+a_3\frac{A_1^3(t)}{4}\cos(3\omega_1 t+3\phi_1(t))$$
$$+a_3\frac{A_2^3(t)}{4}\cos(3\omega_2 t+3\phi_2(t))$$

Blocker's cross-modulations

$$+a_3\frac{3A_1^2(t)A_2(t)}{4}\cos((2\omega_1+\omega_2)t+2\phi_1(t)+\phi_2(t))$$
$$+a_3\frac{3A_1^2(t)A_2(t)}{4}\cos((2\omega_1-\omega_2)t+2\phi_1(t)-\phi_2(t))$$
$$+a_3\frac{3A_2^2(t)A_1(t)}{4}\cos((2\omega_2+\omega_1)t+2\phi_2(t)+\phi_1(t))$$
$$+a_3\frac{3A_2^2(t)A_1(t)}{4}\cos((2\omega_2-\omega_1)t+2\phi_2(t)-\phi_1(t))$$

Desired signal and one blocker cross-modulations

$$+a_3\frac{3A_1^2(t)A_0(t)}{4}\cos((2\omega_1+\omega_0)t+2\phi_1(t)+\phi_0(t))$$
$$+a_3\frac{3A_1^2(t)A_0(t)}{4}\cos((2\omega_1-\omega_0)t+2\phi_1(t)-\phi_0(t))$$
$$+a_3\frac{3A_0^2(t)A_1(t)}{4}\cos((2\omega_0+\omega_1)t+2\phi_0(t)+\phi_1(t))$$
$$+a_3\frac{3A_0^2(t)A_1(t)}{4}\cos((2\omega_0-\omega_1)t+2\phi_0(t)-\phi_1(t))$$
$$+a_3\frac{3A_2^2(t)A_0(t)}{4}\cos((2\omega_2+\omega_0)t+2\phi_2(t)+\phi_0(t))$$
$$+a_3\frac{3A_2^2(t)A_0(t)}{4}\cos((2\omega_2-\omega_0)t+2\phi_2(t)-\phi_0(t))$$
$$+a_3\frac{3A_0^2(t)A_2(t)}{4}\cos((2\omega_0+\omega_2)t+2\phi_0(t)+\phi_2(t))$$
$$+a_3\frac{3A_0^2(t)A_2(t)}{4}\cos((2\omega_0-\omega_2)t+2\phi_0(t)-\phi_2(t))$$

Desired signal and *both* blockers cross-modulations

$$+a_3\frac{6A_0(t)A_1(t)A_2(t)}{4}\cos((\omega_1-\omega_2-\omega_0)t+\phi_1(t)-\phi_2(t)-\phi_0(t))$$
$$+a_3\frac{6A_0(t)A_1^1(t)A_2(t)}{4}\cos((\omega_1-\omega_2+\omega_0)t+\phi_1(t)-\phi_2(t)+\phi_0(t))$$
$$+a_3\frac{6A_0(t)A_1^1(t)A_2(t)}{4}\cos((\omega_1+\omega_2-\omega_0)t+\phi_1(t)+\phi_2(t)-\phi_0(t))$$
$$+a_3\frac{6A_0(t)A_1^1(t)A_2(t)}{4}\cos((\omega_1+\omega_2+\omega_0)t+\phi_1(t)+\phi_2(t)+\phi_0(t))$$

A.2 I/Q Bandpass Nonlinearity

These examples demonstrate the final complex IMD profile of nonlinearities in I and Q branches of a radio receiver based on I/Q downconverion principle exhibiting 2nd- and 3rd-order nonlinearity. Three complex signals at distinct frequencies $\hat{\omega}_0$, $\hat{\omega}_1$ and $\hat{\omega}_2$ are used as the nonlinearity input. Moreover, to present a realistic and more general scenario the nonlinearities in I and Q branches exhibit different characteristics. The output spurious frequencies here are categorized to motivate the scenario in which a weak desired signal at

$\hat{\omega}_0$ and two strong blockers at $\hat{\omega}_1$ and $\hat{\omega}_2$ are present at the nonlinearity input i.e. $\mathbb{E}[|A_0(t)|^2] \ll \mathbb{E}[|A_1(t)|^2]$ and $\mathbb{E}[|A_0(t)|^2] \ll \mathbb{E}[|A_2(t)|^2]$. The signal model for I and Q elements of downconverted signal $x(t)$ which contain three signals with distinct frequencies passing through nonlinear elements are presented in the following tables.

$$x(t) = A_0(t)e^{j(\hat{\omega}_0 t+\phi_0(t))} + A_1(t)e^{j(\hat{\omega}_1 t+\phi_1(t))} + A_2(t)e^{j(\hat{\omega}_2 t+\phi_2(t))} \tag{A.2}$$

Table A.3: IMD components for $b_1 x_I(t) + b_2 x_I^2(t) + j[g_1 b_1 x_Q(t) + g_2 b_2 x_Q^2(t)]$

Original signal components
$+b_1\frac{1+g_1}{2}A_0(t)e^{j(\hat{\omega}_0 t+\phi_0(t))}$ $+b_1\frac{1-g_1}{2}A_0(t)e^{-j(\hat{\omega}_0 t+\phi_0(t))}$ $+b_1\frac{1+g_1}{2}A_1(t)e^{j(\hat{\omega}_1 t+\phi_1(t))}$ $+b_1\frac{1-g_1}{2}A_1(t)e^{-j(\hat{\omega}_1 t+\phi_1(t))}$ $+b_1\frac{1+g_1}{2}A_2(t)e^{j(\hat{\omega}_2 t+\phi_2(t))}$ $+b_1\frac{1-g_1}{2}A_2(t)e^{-j(\hat{\omega}_2 t+\phi_2(t))}$
Components around DC
$+b_2(1+jg_2)[\frac{A_0^2(t)}{2}+\frac{A_1^2(t)}{2}+\frac{A_2^2(t)}{2}]$
Components at ±2-times original frequencies
$+b_2\frac{1-jg_2}{4}\frac{A_0^2(t)}{2}e^{j(2\hat{\omega}_0 t+2\phi_0(t))}$ $+b_2\frac{1-jg_2}{4}\frac{A_0^2(t)}{2}e^{-j(2\hat{\omega}_0 t+2\phi_0(t))}$ $+b_2\frac{1-jg_2}{4}\frac{A_1^2(t)}{2}e^{j(2\hat{\omega}_1 t+2\phi_1(t))}$ $+b_2\frac{1-jg_2}{4}\frac{A_1^2(t)}{2}e^{-j(2\hat{\omega}_1 t+2\phi_1(t))}$ $+b_2\frac{1-jg_2}{4}\frac{A_2^2(t)}{2}e^{j(2\hat{\omega}_2 t+2\phi_2(t))}$ $+b_2\frac{1-jg_2}{4}\frac{A_2^2(t)}{2}e^{-j(2\hat{\omega}_2 t+2\phi_2(t))}$
Blocker's cross-modulations
$+b_2\frac{1-jg_2}{2}A_1(t)A_2(t)e^{j((\hat{\omega}_1+\hat{\omega}_2)t+\phi_1(t)+\phi_2(t))}$ $+b_2\frac{1-jg_2}{2}A_1(t)A_2(t)e^{-j((\hat{\omega}_1+\hat{\omega}_2)t+\phi_1(t)+\phi_2(t))}$ $+b_2\frac{1+jg_2}{2}A_1(t)A_2(t)e^{j((\hat{\omega}_1-\hat{\omega}_2)t+\phi_1(t)-\phi_2(t))}$ $+b_2\frac{1+jg_2}{2}A_1(t)A_2(t)e^{-j((\hat{\omega}_1-\hat{\omega}_2)t+\phi_1(t)-\phi_2(t))}$

Desired signal and one blocker cross-modulations
$+b_2\frac{1-jg_2}{2}A_1(t)A_0(t)e^{j((\hat{\omega}_1+\hat{\omega}_0)t+\phi_1(t)+\phi_0(t))}$ $+b_2\frac{1-jg_2}{2}A_1(t)A_0(t)e^{-j((\hat{\omega}_1+\hat{\omega}_0)t+\phi_1(t)+\phi_0(t))}$ $+b_2\frac{1+jg_2}{2}A_1(t)A_0(t)e^{j(\hat{\omega}_1-\hat{\omega}_0)t+\phi_1(t)-\phi_0(t)}$ $+b_2\frac{1+jg_2}{2}A_1(t)A_0(t)e^{-j(\hat{\omega}_1-\hat{\omega}_0)t+\phi_1(t)-\phi_0(t)}$ $+b_2\frac{1-jg_2}{2}A_2(t)A_0(t)e^{j(\hat{\omega}_2+\hat{\omega}_0)t+\phi_2(t)+\phi_0(t)}$ $+b_2\frac{1-jg_2}{2}A_2(t)A_0(t)e^{-j(\hat{\omega}_2+\hat{\omega}_0)t+\phi_2(t)+\phi_0(t)}$ $+b_2\frac{1+jg_2}{2}A_2(t)A_0(t)e^{j(\hat{\omega}_2-\hat{\omega}_0)t+\phi_2(t)-\phi_0(t)}$ $+b_2\frac{1+jg_2}{2}A_2(t)A_0(t)e^{-j(\hat{\omega}_2-\hat{\omega}_0)t+\phi_2(t)-\phi_0(t)}$

Table A.4: IMD components for $b_1x_I(t) + b_3x_I^3(t) + j\left[g_1b_1x_Q(t) + g_3b_3x_Q^3(t)\right]$

Original signal components
$+b_1\frac{1+g_1}{2}A_0(t)e^{j(\hat{\omega}_0t+\phi_0(t))}$ $+b_1\frac{1-g_1}{2}A_0(t)e^{-j(\hat{\omega}_0t+\phi_0(t))}$ $+b_1\frac{1+g_1}{2}A_1(t)e^{j(\hat{\omega}_1t+\phi_1(t))}$ $+b_1\frac{1-g_1}{2}A_1(t)e^{-j(\hat{\omega}_1t+\phi_1(t))}$ $+b_1\frac{1+g_1}{2}A_2(t)e^{j(\hat{\omega}_2t+\phi_2(t))}$ $+b_1\frac{1-g_1}{2}A_2(t)e^{-j(\hat{\omega}_2t+\phi_2(t))}$
Self-distortion components
$+\frac{b_3(1+g_3)}{2}\left(\frac{3A_0^3(t)}{4}+\frac{3A_1^2(t)A_0(t)}{2}+\frac{3A_2^2(t)A_0(t)}{2}\right)e^{j(\hat{\omega}_0t+\phi_0(t))}$ $+\frac{b_3(1+g_3)}{2}\left(\frac{3A_1^3(t)}{4}+\frac{3A_2^2(t)A_1(t)}{2}+\frac{3A_0^2(t)A_1(t)}{2}\right)e^{j(\hat{\omega}_1t+\phi_1(t))}$ $+\frac{b_3(1+g_3)}{2}\left(\frac{3A_2^3(t)}{4}+\frac{3A_1^2(t)A_2(t)}{2}+\frac{3A_0^2(t)A_2(t)}{2}\right)e^{j(\hat{\omega}_2t+\phi_2(t))}$
IMD Components at original signals mirror frequency
$+\frac{b_3(1-g_3)}{2}\left(\frac{3A_0^3(t)}{4}+\frac{3A_1^2(t)A_0(t)}{2}+\frac{3A_2^2(t)A_0(t)}{2}\right)e^{-j(\hat{\omega}_0t+\phi_0(t))}$ $+\frac{b_3(1-g_3)}{2}\left(\frac{3A_1^3(t)}{4}+\frac{3A_2^2(t)A_1(t)}{2}+\frac{3A_0^2(t)A_1(t)}{2}\right)e^{-j(\hat{\omega}_1t+\phi_1(t))}$

$$+\frac{b_3(1-g_3)}{2}\left(\frac{3A_2^3(t)}{4}+\frac{3A_1^2(t)A_2(t)}{2}+\frac{3A_0^2(t)A_2(t)}{2}\right)e^{-j(\hat{\omega}_2 t+\phi_2(t))}$$

Components at ±3-times original frequencies

$$+\frac{b_3(1-g_3)}{2}\frac{A_0^3(t)}{4}e^{j(3\hat{\omega}_0 t+3\phi_0(t))}$$
$$+\frac{b_3(1+g_3)}{2}\frac{A_0^3(t)}{4}e^{-j(3\hat{\omega}_0 t+3\phi_0(t))}$$
$$+\frac{b_3(1-g_3)}{2}\frac{A_1^3(t)}{4}e^{j(3\hat{\omega}_1 t+3\phi_1(t))}$$
$$+\frac{b_3(1+g_3)}{2}\frac{A_1^3(t)}{4}e^{-j(3\hat{\omega}_1 t+3\phi_1(t))}$$
$$+\frac{b_3(1-g_3)}{2}\frac{A_2^3(t)}{4}e^{j(3\hat{\omega}_2 t+3\phi_2(t))}$$
$$+\frac{b_3(1+g_3)}{2}\frac{A_2^3(t)}{4}e^{-j(3\hat{\omega}_2 t+3\phi_2(t))}$$

Blocker's cross-modulations

$$+\frac{b_3(1-g_3)}{2}\frac{3A_1^2(t)A_2(t)}{4}e^{j((2\hat{\omega}_1+\hat{\omega}_2)t+2\phi_1(t)+\phi_2(t))}$$
$$+\frac{b_3(1+g_3)}{2}\frac{3A_1^2(t)A_2(t)}{4}e^{-j((2\hat{\omega}_1+\hat{\omega}_2)t+2\phi_1(t)+\phi_2(t))}$$
$$+\frac{b_3(1+g_3)}{2}\frac{3A_1^2(t)A_2(t)}{4}e^{j((2\hat{\omega}_1-\hat{\omega}_2)t+2\phi_1(t)-\phi_2(t))}$$
$$+\frac{b_3(1-g_3)}{2}\frac{3A_1^2(t)A_2(t)}{4}e^{-j((2\hat{\omega}_1-\hat{\omega}_2)t+2\phi_1(t)-\phi_2(t))}$$
$$+\frac{b_3(1-g_3)}{2}\frac{3A_2^2(t)A_1(t)}{4}e^{j((2\hat{\omega}_2+\hat{\omega}_1)t+2\phi_2(t)+\phi_1(t))}$$
$$+\frac{b_3(1+g_3)}{2}\frac{3A_2^2(t)A_1(t)}{4}e^{-j((2\hat{\omega}_2+\hat{\omega}_1)t+2\phi_2(t)+\phi_1(t))}$$
$$+\frac{b_3(1+g_3)}{2}\frac{3A_2^2(t)A_1(t)}{4}e^{j((2\hat{\omega}_2-\hat{\omega}_1)t+2\phi_2(t)-\phi_1(t))}$$
$$+\frac{b_3(1-g_3)}{2}\frac{3A_2^2(t)A_1(t)}{4}e^{-j((2\hat{\omega}_2-\hat{\omega}_1)t+2\phi_2(t)+\phi_1(t))}$$

Desired signal and one blocker cross-modulations

$$+\frac{b_3(1-jg_3)}{2}\frac{3A_1^2(t)A_0(t)}{4}e^{j((2\hat{\omega}_1+\hat{\omega}_0)t+2\phi_1(t)+\phi_0(t))}$$
$$+\frac{b_3(1+jg_3)}{2}\frac{3A_2^2(t)A_1(t)}{4}e^{-j((2\hat{\omega}_1+\hat{\omega}_0)t+2\phi_2(t)+\phi_1(t))}$$
$$+\frac{b_3(1+jg_3)}{2}\frac{3A_1^2(t)A_0(t)}{4}e^{j((2\hat{\omega}_1-\hat{\omega}_0)t+2\phi_1(t)-\phi_0(t))}$$
$$+\frac{b_3(1-jg_3)}{2}\frac{3A_2^2(t)A_1(t)}{4}e^{-j((2\hat{\omega}_1-\hat{\omega}_0)t+2\phi_2(t)+\phi_1(t))}$$
$$+\frac{b_3(1-jg_3)}{2}\frac{3A_0^2(t)A_1(t)}{4}e^{j((2\hat{\omega}_0+\hat{\omega}_1)t+2\phi_0(t)+\phi_1(t))}$$
$$+\frac{b_3(1+jg_3)}{2}\frac{3A_2^2(t)A_1(t)}{4}e^{-j((2\hat{\omega}_0+\hat{\omega}_1)t+2\phi_2(t)+\phi_1(t))}$$
$$+\frac{b_3(1+jg_3)}{2}\frac{3A_0^2(t)A_1(t)}{4}e^{j((2\hat{\omega}_0-\hat{\omega}_1)t+2\phi_0(t)-\phi_1(t))}$$
$$+\frac{b_3(1-jg_3)}{2}\frac{3A_2^2(t)A_1(t)}{4}e^{-j((2\hat{\omega}_0-\hat{\omega}_1)t+2\phi_2(t)+\phi_1(t))}$$
$$+\frac{b_3(1-jg_3)}{2}\frac{3A_2^2(t)A_0(t)}{4}e^{j((2\hat{\omega}_2+\hat{\omega}_0)t+2\phi_2(t)+\phi_0(t))}$$
$$+\frac{b_3(1+jg_3)}{2}\frac{3A_2^2(t)A_1(t)}{4}e^{-j((2\hat{\omega}_2+\hat{\omega}_0)t+2\phi_2(t)+\phi_1(t))}$$
$$+\frac{b_3(1+jg_3)}{2}\frac{3A_2^2(t)A_0(t)}{4}e^{j((2\hat{\omega}_2-\hat{\omega}_0)t+2\phi_2(t)-\phi_0(t))}$$

$$+\frac{b_3(1-jg_3)}{2}\frac{3A_2^2(t)A_1(t)}{4}e^{-j((2\hat{\omega}_2-\hat{\omega}_0)t+2\phi_2(t)+\phi_1(t))}$$
$$+\frac{b_3(1-jg_3)}{2}\frac{3A_0^2(t)A_2(t)}{4}e^{j((2\hat{\omega}_0+\hat{\omega}_2)t+2\phi_0(t)+\phi_2(t))}$$
$$+\frac{b_3(1+jg_3)}{2}\frac{3A_2^2(t)A_1(t)}{4}e^{-j((2\hat{\omega}_0+\hat{\omega}_2)t+2\phi_2(t)+\phi_1(t))}$$
$$+\frac{b_3(1+jg_3)}{2}\frac{3A_0^2(t)A_2(t)}{4}e^{j((2\hat{\omega}_0-\hat{\omega}_2)t+2\phi_0(t)-\phi_2(t))}$$
$$+\frac{b_3(1-jg_3)}{2}\frac{3A_2^2(t)A_1(t)}{4}e^{-j((2\hat{\omega}_0-\hat{\omega}_2)t+2\phi_2(t)+\phi_1(t))}$$

Desired signal and *both* blockers cross-modulations

$$+\frac{b_3(1-jg_3)}{2}\frac{6A_0(t)A_1(t)A_2(t)}{4}e^{j((\hat{\omega}_1-\hat{\omega}_2-\hat{\omega}_0)t+\phi_1(t)-\phi_2(t)-\phi_0(t))}$$
$$+\frac{b_3(1+jg_3)}{2}\frac{6A_0(t)A_1(t)A_2(t)}{4}e^{-j((\hat{\omega}_1-\hat{\omega}_2-\hat{\omega}_0)t+\phi_1(t)-\phi_2(t)-\phi_0(t))}$$
$$+\frac{b_3(1+jg_3)}{2}\frac{6A_0(t)A_1(t)A_2(t)}{4}e^{j((\hat{\omega}_1-\hat{\omega}_2+\hat{\omega}_0)t+\phi_1(t)-\phi_2(t)+\phi_0(t))}$$
$$+\frac{b_3(1-jg_3)}{2}\frac{6A_0(t)A_1(t)A_2(t)}{4}e^{-j((\hat{\omega}_1-\hat{\omega}_2+\hat{\omega}_0)t+\phi_1(t)-\phi_2(t)+\phi_0(t))}$$
$$+\frac{b_3(1+jg_3)}{2}\frac{6A_0(t)A_1(t)A_2(t)}{4}e^{j((\hat{\omega}_1+\hat{\omega}_2-\hat{\omega}_0)t+\phi_1(t)+\phi_2(t)-\phi_0(t))}$$
$$+\frac{b_3(1-jg_3)}{2}\frac{6A_0(t)A_1(t)A_2(t)}{4}e^{-j((\hat{\omega}_1+\hat{\omega}_2-\hat{\omega}_0)t+\phi_1(t)+\phi_2(t)-\phi_0(t))}$$
$$+\frac{b_3(1-jg_3)}{2}\frac{6A_0(t)A_1(t)A_2(t)}{4}e^{j((\hat{\omega}_1+\hat{\omega}_2+\hat{\omega}_0)t+\phi_1(t)+\phi_2(t)+\phi_0(t))}$$
$$+\frac{b_3(1+jg_3)}{2}\frac{6A_0(t)A_1(t)A_2(t)}{4}e^{-j((\hat{\omega}_1+\hat{\omega}_2+\hat{\omega}_0)t+\phi_1(t)+\phi_2(t)+\phi_0(t))}$$

BIBLIOGRAPHY

[1] *Near Field Communication Interface and Protocol*, ECMA-340; second ed., 2004.

[2] *Evolved Universal Terrestrial Radio Access (E-UTRA) ; Physical Channels and Modulation*, 3GPP TS 36.211 V9.1.0, 2010.

[3] J. Mitola, "The software radio architecture," *IEEE Commun. Magazine*, vol. 33, no. 5, pp. 26–38, May 1995.

[4] S. Haykin, "Cognitive radio: brain-empowered wireless communications," *IEEE J. Selected Areas in Comm.*, vol. 23, no. 2, pp. 201 – 220, feb 2005.

[5] D. Cabric and R. W. Brodersen, "Physical layer design issues unique to cognitive radio systems," in *Proc. IEEE Int. Symp. on Personal, Indoor and Mob. Radio Comm. (PIMRC)*, vol. 2, 2005, pp. 759–763.

[6] B. Razavi, "Cognitive radio design challenges and techniques," *IEEE J. Solid-State Circuits*, vol. 45, no. 8, pp. 1542–1553, Aug. 2010.

[7] D. Cabric, "Addressing feasibility of cognitive radios," *IEEE Sign. Proc. Magazine*, vol. 25, no. 6, pp. 85–93, Nov. 2008.

[8] G. Fettweis, M. Lhning, D. Petrovic, M. Windisch, P. Zillmann, and W. Rave, "Dirty RF: A new paradigm," *Int. J. Wireless Inform. Networks*, vol. 14, pp. 133–148, 2007.

[9] S. Mirabbasi and K. Martin, "Classical and modern receiver architectures," *IEEE Commun. Magazine*, vol. 38, no. 11, pp. 132–139, Nov. 2000.

[10] J. Tsui, *Digital Techniques for Wideband Receivers.* Norwood, MA: Artech House Publishers, 1995.

[11] J. Crols and M. S. J. Steyaert, "Low-IF topologies for high-performance analog front ends of fully integrated receivers," *IEEE Trans. Circuits Syst. II*, vol. 45, pp. 269–282, Mar. 1998.

[12] ——, *CMOS Wireless Transceiver Design for digital Communications.* Dordrecht, The Netherlands: Kluwer Academic Publisher, 1997.

[13] A. A. Abidi, "Direct conversion radio tranceivers for digital communications," *IEEE J. Solid-State Circuits*, vol. 30, no. 12, pp. 1399–1410, Dec. 1995.

[14] B. Razavi, "Design consideration for direct conversion receivers," *IEEE Trans. Circuits Syst. II*, vol. 44, no. 6, pp. 428–435, 1997.

[15] M. Valkama, *Advanced I/Q Signal Processing in Wide-band Receivers: Models and Algorithms.* Ph.D. dissertation, Tampere University of Technology, Finland, 2001.

[16] L. Anttila, M. Valkama, and M. Renfors, "Frequency-selective I/Q mismatch calibration of wideband direct-conversion transmitters," *IEEE Trans. Circuits Syst. II*, vol. 55, no. 4, pp. 359–363, Apr. 2008.

[17] Y. Zou, *Analysis and Mitigation of I/Q Imbalances in Multi-antenna Transmission Systems.* Ph.D. dissertation, Tampere University of Technology, Finland, 2009.

[18] B. Razavi, RF *Microelectrinics.* Upper Saddle River, NJ: Prentice Hall, 1998.

[19] C. Chien, *Digital Radio Systems on a Chip.* Norwell, MA: Kluwer Academic Publisher, 2001.

[20] M. Faulkner, "Automatic adjustment of quadrature modulators," vol. 27, no. 3, pp. 214–215, Jan. 1991.

[21] ——, "DC offset and IM2 removal in direct conversion receivers," *IEE Proc. Commun.*, vol. 149, pp. 179–184, Jun. 2002.

[22] P. Alinikula, H. O. Scheck, and K. P. Estola, "Elimination of DC offset and spurious AM suppression in a direct conversion receiver," *U.S Patent*, no. 6115593, Sep. 2000.

[23] S. Laursen, *Second Order Ditortion in CMOS Integrated Mixers.* Aalborg, Denmark: Ph.D. dissertation, Aalborg University, 2004.

[24] L. D. Quach and S. P. Stapleton, "A postdistortion receiver for mobile communications," *IEEE Trans. Veh. Technol.*, vol. 42, pp. 604–616, Nov. 1993.

[25] K. Dufrene and R. Weigel, "Adaptive IP2 calibration scheme for direct conversion receivers," in *IEEE Radio and Wireless Symp.*, San Diego, CA, Oct. 2006, pp. 1755–1758.

[26] Q. Zou, M. Mikhemar, and A. H. Sayed, "Digital compensation of cross-modulation distortion in software-defined radios," *IEEE Journal of Selected Topics in Signal Processing*, vol. 3, no. 32, pp. 348–361, Jun. 2009.

[27] E. A. Keehr and A. Hajimiri, "Equalization of third-order intermodulation products in wideband direct conversion receivers," *IEEE J. Solid-State Circuits*, vol. 43, no. 12, pp. 2853 –2867, Dec. 2008.

[28] ——, "Digitally assisted equalization of third-order intermodulation products in wideband direct conversion receivers," *Int. Journal of Microw. and Wireless Tech.*, vol. 1, no. Special Issue 04, pp. 377–385, Jun. 2009.

[29] ——, "Successive regeneration and adaptive cancellation of higher order intermodulation products in RF receivers," *IEEE Trans. Microw. Theory Tech.*, vol. 59, pp. 1379 – 1396, May 2011.

[30] M. Allén, J. Marttila, and M. Valkama, "Digital post-processing for reducing A/D converter nonlinear distortion in wideband radio receivers," in *Proc. Asilomar Conf. Signals, Syst., Comput.*, Pacific Grove, CA, Nov. 2009, pp. 1111–1114.

[31] A. Bateman and D. M. Haines, "Direct conversion transceiver design for compact low-cost portable mobile radio terminals," in *Proc. IEEE Veh. Techn. Conf. (VTC)*, vol. 1, San Francisco, CA, May 1989, pp. 57–62.

[32] K. Kivekäs, A. Pärssinen, and K. A. I. Halonen, "Charactrization of IIP2 and DC-offset in transconductance mixers," *IEEE Trans. Circuits Syst. II*, vol. 48, no. 11, pp. 1028–1038, 2001.

[33] T. Huovinen, A. Shahed hagh ghdam, and M. Valkama, "Blind diversity reception and interference cancellation using ICA," in *Proc. IEEE Int. Conf. on Acoustics, Speech and Sig. Proc. (ICASSP)*, vol. 3, Honolulu, HI., 2007, pp. 685–688.

[34] ——, "Higher-order blind estimation of generalized eigenfilters using independent component analysis," in *Workshop on Cognitive Information Processing (CIP)*, Santorini, Greece, 2008, pp. 92–97.

[35] J. G. Proakis, *Digital Communications*. New York, NY: McGraw-Hill, 2001.

[36] J. R. Barry, E. A. Lee, and D. G. Messerschmitt, *Digital Communication*. 3rd ed. Norwell, MA: Kluwer Academic Publisher, 2004.

[37] D. Dardari, V. Tralli, and A. Vaccari, "A theoretical characterization of nonlinear distortion effects in OFDM systems," *IEEE Trans. Commun.*, vol. 48, no. 2, pp. 1755–1764, Oct. 2000.

[38] J. Heiskala and J. Terry, *OFDM Wireless LANs: A Theoretical and Practical Guide*. SAMS publishing, 2002.

[39] P. B. Kenington, *High Linearity RF Amplifier Design*. Norwood, MA: Artech House Publishers, 2000.

[40] S. C. Cripps, *RF Power Amplifiers for Wireless Communications*. 2nd ed. Norwood, MA: Artech House Publishers, 2006.

[41] J. K. Cavers, "Adaptation behavior of a feedforward amplifier linearizer," *IEEE Trans. Veh. Technol.*, pp. 31–40, Feb. 1995.

[42] N. Pothecary, *Feedforward Linear Power Amplifier*. Norwood, MA: Artech House Publishers, 1999.

[43] J. Legarda, *Feedforward Amplifier for Wideband Wireless Communication*. Dordrecht, The Netherlands: Springer, 2003.

[44] K. J. Parsons, P. B. Kenington, and J. P. McGeehan, "High efficiency power amplifier design for mobile satellite earth stations," *IEE Coll. on Evolving Technol. for Small Earth Station Hardware*, pp. 3/1–3/6, Feb. 1995.

[45] J. Legarda, J. Presa, E. Hernandez, H. Solar, J. Mendizabal, and J. A. Penaranda, "An adaptive feedforward amplifier under maximum output control method for UMTS downlink transmitters," *IEEE Trans. Microw. Theory Tech.*, vol. 53, pp. 2481–2486, Aug. 2005.

[46] J. K. Cavers, "A DSP controlled adaptive feedforward amplifier linearizer," in *Proc. Universal Personal Communications*, Cambridge, MA, USA, Sep. 1996, pp. 788–792.

[47] A. H. Gokceoglu, A. Shahed hagh ghdam, and M. Valkama, "Performance analysis of adaptive wideband feedforward linearizer," To appear in *IEEE Transactions on Signal Processing*.

[48] R. Chandrasekaran, "Model-based feedforward linearization of amplifiers," *U.S Patent*, no. 6765440, Jun. 2004.

[49] R. G. Randall, J. G. McRory, and R. H. Johnston, "Broadband DSP based feedforward amplifier lineariser," *IEE Electronics Letters*, vol. 38, pp. 1470–1471, Nov. 2002.

[50] E. G. Jeckeln, F. M. Ghannouchi, M. Sawan, and F. Beauregard, "Efficient baseband/RF feedforward linearizer through a mirror power amplifier using software-defined radio and quadrature digital up-conversion," in *IEEE MTT-S Int. Microw. Dig.*, vol. 2, Phoenix, AZ, May 2001, pp. 789–792.

[51] B. Aleiner, "Digital feed-forward linearization," *Microw. Journal*, vol. 52, no. 10, p. 110, Oct. 2009.

[52] M. K. Nezami, "Feedforward power amplifier linearization for 4G basestation," Kuala Lumpur, Malaysia, Dec. 2009, pp. 880–884.

[53] J. Kwon and C. Eun, "Digital feedforward compensation scheme for the nonlinear power amplifier with memory," *Int. J. Intell. Syst. Technol. Appl.*, vol. 9, pp. 326–334, November 2010.

[54] G. Strang, *Linear Algebra and Its applications*. Boston: Brooks/cole, 1998.

[55] Z. Koldovsky and P. Tichavsky, "Methods of fair comparison of performance of linear ICA techniques in presence of additive noise," in *Proc. IEEE Int. Conf. on Acoustics, Speech and Sig. Proc. (ICASSP)*, Toulouse, France, May 2006, pp. 873–876.

[56] R. G. Meyer and A. K. Wong, "Blocking and desensitization in RF amplifier," *IEEE Commun. Magazine*, vol. 30, pp. 944–946, Aug. 1995.

[57] X. Li and M. Ismail, *Multi-Standard CMOS Wireless Receivers*. Norwell, MA: Kluwer Academic Publisher, 2002.

[58] W. Tuttlebee, Ed., *Software Defined Radio: Enabling Technologies*. Chichester,U.K.: Wiley, 2002.

[59] P. B. Kenington, *RF and Baseband Techniques for Software Defined Radio*. Norwood, MA: Artech House Publishers, 2005.

[60] J. C. Pedro and N. B. Carvalho, *Intermodulation Distortion in Microwave and Wireless Circuits*. Norwood, MA: Artech House Publishers, 2003.

[61] M. E. Frerking, *Digital Signal Processing in Communication Systems*. New York,US: Chapman & Hall, 1994.

[62] T. S. Rappaport, *Wireless Communications: Principles and Practice*. 2nd ed. Upper Saddle River, NJ: Prentice Hall, 2002.

[63] J. Mitola, *Cognitive Radio*. Ph.D. dissertation, Royal Institute of Technology (KTH), Stockholm, Sweden, 2000.

[64] S. Haykin, *Adaptive Filter Theory*. 4th ed. Upper Saddle River, NJ: Prentice Hall, 2002.

[65] H. Meyr, M. Moeneclaey, and S. Fechtel, *Digital Communication Receivers*. New York,US: John Wiley & Sons, Ltd., 1998.

[66] D. Brennan, "Linear diversity combining techniques," in *Proc. of the IRE*, vol. 47, 1959, pp. 1075–11 102.

[67] A. Hyvärinen, J. Karhunen, and E. Oja, *Independent Component Analysis*. New York,US: John Wiley & Sons, Ltd., 2001.

[68] J. F. Cardoso and B. H. Laheld, "Equivariant adaptive source separation," *IEEE Trans. Sign. Proc.*, vol. 44, no. 12, pp. 3017–3010, Dec. 1996.

[69] A. Katz, "Linearization: reducing distortion in power amplifiers," *IEEE Microw. Magazine*, vol. 2, no. 4, pp. 37–49, Dec. 2001.

[70] F. M. Ghannouchi and O. Hammi, "Power amplifier and transmitter architectures for software defined radio systems," vol. 10, pp. 56–63, Fourth Quarter 2010.

[71] ——, "Behavioral modeling and predistortion," *IEEE Microw. Magazine*, vol. 10, pp. 52–64, Dec. 2009.

[72] P. M. Lavrador, T. R. Cunha, P. M. Cabral, and J. C. Pedro, "The linearity-efficiency compromise," *IEEE Microw. Magazine*, vol. 11, pp. 44–58, Aug. 2010.

[73] A. Papoulis, *Probability, Random Variables and Stochastic Process*. New York, NY: McGraw-Hill, 1991.

[74] T. Schenk, *RF Imperfections in High-rate Wireless Systems: Impact and Digital Compensation*. Dordrecht, The Netherlands: Springer, 2008.

[75] A. M. Smith and J. K. Cavers, "A wideband architecture for adaptive feedforward linearization," in *Proc. IEEE Veh. Techn. Conf. (VTC)*, vol. 3, Ottawa, Ont., May 1998, pp. 2488–2492.

[76] D. Schruers, M. O'Droma, A. A. Goacher, and M. Gadringer, *RF Power Amplifier Behavioral Modeling*. Cambridge, UK: Cambridge University Press, 2009.

[77] K. Rapp, "Effects of the hpa-nonlinearity on a 4-DQPSK/OFDM signal for a digital sound broadcasting system," in *Proc. 2nd European Conference on Satellite Communications*, vol. ESA-SP-332, October 1991, pp. 179–184.

[78] S. Benedetto and E. Biglieri, *Principles of Digital Transmission with Wireless applications*. Norwell, MA: Kluwer Academic Publisher, 1999.

[79] L. Ding, *Digital Predistortion of Power Amplifiers for Wireless Applications*. Ph.D. dissertation, School of Electrical and Computer Engineering, Georgia Institute of Technology, 2004.

[80] G. T. Zhou, H. Qian, L. Ding, and R. Raich, "On the baseband representation of a bandpass nonlinearity," *IEEE Trans. Sign. Proc.*, vol. 53, no. 8, pp. 2953 – 2957, Aug. 2005.

[81] A. Saleh, "Frequency-independent and frequency-dependent nonlinear models of TWT amplifiers," *IEEE Trans. Commun.*, vol. 29, pp. 1715–1720, Nov. 1981.

[82] S. C. Cripps, *Advanced Techniques in RF Power Amplifier design*. Norwood, MA: Artech House Publishers, 2002.

[83] H. H. Boo, W. C. Sung, and J. L. Dawson, "Adaptive predistortion using a $\Delta\Sigma$ modulator for automatic inversion of power amplifier nonlinearity," *IEEE Trans. Circuits Syst. II*, vol. 56, no. 12, pp. 901–905, Dec. 2009.

[84] J. Mehta, V. Zoicas, O. Eliezer, R. B. Staszewski, S. Rezeq, M. Entezari, and P. Balsara, "An efficient linearization scheme for a digital polar EDGE transmitter," *IEEE Trans. Circuits Syst. II*, vol. 57, pp. 193–197, 2010.

[85] J. Vuolevi and T. Rahkonen, *Distortion in RF Power Amplifiers*. Norwood, MA: Artech House Publishers, 2003.

[86] K.-H. Lim, G. Ahn, S. Jung, H.-C. Park, M.-S. Kim, J.-H. Van, H. Cho, J.-H. Jeong, C.-S. Park, and Y. Yang, "A 60-W multicarrier WCDMA power amplifier using an RF predistorter," *IEEE Trans. Circuits Syst. II*, vol. 56, pp. 265–269, Apr. 2009.

[87] W. J. Kim, K. J. Cho, S. P. Stapleton, and J. H. Kim, "Efficiency comparison of a digitally predistorted and a feed-forward linearized Doherty amplifier with crest factor reduction," *Microw. Journal*, vol. 50, no. 5, p. 228, May 2007.

[88] M. O'Droma, E. Bertran, J. Portilla, N. Mgebrishvili, S. D. Guerrieri, G. Montoro, T. J. Brazil, and G. Magerl, "On linearisation of microwave-transmitter solid-state power amplifiers," *Int. Journal of RF and Microwave Computer-Aided Engineering*, vol. 15, pp. 491–505, Sep. 2005.

[89] C. L. Larose and F. M. Ghannouchi, "Optimal adaptation methods and class of operation: keys to improving feedforward amplifier power efficiency," *IEEE Trans. Veh. Technol.*, vol. 54, no. 2, pp. 456–467, Mar. 2005.

[90] J. T. Chen, H. S. Tsai, and Y.-K. Chen, "The optimal RLS parameter tracking algorithm for a power amplifier feedforward linearizer," *IEEE Trans. Circuits Syst. II*, vol. 46, no. 4, pp. 464–468, Apr. 1999.

[91] S. Narahashi and T. Nojima, "Extremely low-distortion multicarrier amplifier self-adjusting feedforward (SAFF) amplifier," in *Proc. IEEE Int. Conf. on Comm. (ICC)*, vol. 3, Denver, CO, 1991, pp. 1485–1490.

[92] S. Kang, U. Park, K. Lee, and S. Hong, "Adaptive feedforward amplifier using pilot signals," *Proc. Int. Conf. on Telecomm. (ICT)*, vol. 1, pp. 677–680, 2003.

[93] R. N. Braithwaite, "Positive feedback pilot system for second loop control in a feedforward power amplifier," *IEEE Trans. Circuits Syst. I*, vol. 55, no. 10, pp. 3293–3305, Nov. 2008.

[94] B. Picinbono, "Widely linear estimation with complex data," *IEEE Trans. Sign. Proc.*, vol. 43, pp. 2030–2033, Aug. 1995.

[95] R. D. DeGroat and E. M. Dowling, "The data least squares problem and channel equalization," *IEEE Trans. Sign. Proc.*, vol. 41, no. 1, pp. 407–411, Jan. 1993.

[96] G. H. Golub and C. F. V. Loan, "An analysis of the total least squares problem," *SIAM*, vol. 17, no. 6, pp. 883–893, Jan. 1980.

[97] M. Bruno, J. Cousseau, A. Shahed hagh ghdam, and M. Valkama, "On high linearity - high efficiency RF amplifier design," in *Argentine School of Micro-Nanoelectronics, Technology and Applications (EAMTA)*, Montevideo, Uruguay, 2010, pp. 97–102.

[98] A. H. Gokceoglu, A. Shahed hagh ghdam, and M. Valkama, "Effects of power amplifier memory on adaptive feedforward linearize," in *IEEE International Symposium on Wireless Communication Systems (ISWCS)*, Reykjavik, Iceland, 2008, pp. 304–308.

Publications

Tampereen teknillinen yliopisto
PL 527
33101 Tampere

Tampere University of Technology
P.O.B. 527
FI-33101 Tampere, Finland

ISBN 978-952-15-2650-3
ISSN 1459-2045